

DISSERTATION

NOVEL LASER IGNITION TECHNIQUE  
USING DUAL-PULSE PRE-IONIZATION

Submitted by:

Ciprian Dumitrache

Department of Mechanical Engineering

In partial fulfilment of the requirements

For the Degree of Doctor of Philosophy

Colorado State University

Fort Collins, Colorado

Fall 2017

Doctoral Committee:

Advisor: Azer P. Yalin

Co-Advisor: Anthony J. Marchese

Xinfeng Gao

Alan Van Orden

Allan T. Kirkpatrick

Copyright by Ciprian Dumitrache 2017

All Rights Reserved

## ABSTRACT

### NOVEL LASER IGNITION TECHNIQUE USING DUAL-PULSE PRE-IONIZATION

Recent advances in the development of compact high-power laser sources and fiber optic delivery of giant pulses have generated a renewed interest in laser ignition. The non-intrusive nature of laser ignition gives it a set of unique characteristics over the well-established capacitive discharge devices (or spark plugs) that are currently used as ignition sources in engines. A judicious choice of the focusing optics allows one to generate a laser spark in a location where the mixture is homogeneously mixed thus eliminating any unwanted wall effects that can negatively impact the flame growth. In addition, laser ignition eliminates the electrode configuration of the current ignition devices. The cold surface of the electrodes tends to act as a heat sink impeding the development of the early flame kernel near the lean limit. Finally, the different physics governing the laser induced optical breakdown process makes operation at higher pressure easier than in the case of capacitive devices for which erosion at high pressures is a limiting factor in the plug lifetime. Overall, this can have a positive impact on engine operation leading to a reduction in NO<sub>x</sub> emission, fuel saving and an increased operational envelope of current engines.

Conventionally, laser ignition is achieved by tightly focusing a high-power q-switched laser pulse until the optical intensity at the focus is high enough to breakdown the gas molecules ( $I_{\text{threshold}} \sim 300 \text{ GW/cm}^2$ ). This leads to the formation of a spark that serves as the ignition source in engines. However, there are certain disadvantages associated with this ignition method. This ionization approach is energetically inefficient as the medium is transparent to the laser radiation until the laser intensity is high enough to cause gas breakdown. This results in very high energies

required for ignition (about an order of magnitude higher energy than capacitive plugs at stoichiometric conditions). Additionally, the fluid flow induced during the plasma recombination generates high vorticity leading to high rates of flame stretching.

In this work, we are addressing some of the aforementioned disadvantages of laser ignition by developing a novel approach based on a dual-pulse pre-ionization scheme. The new technique works by decoupling the effect of the two ionization mechanisms governing plasma formation: multiphoton ionization (MPI) and electron avalanche ionization (EAI). An UV nanosecond pulse ( $\lambda = 266 \text{ nm}$ ) is used to generate initial ionization through MPI. This is followed by an overlapped NIR nanosecond pulse ( $\lambda = 1064 \text{ nm}$ ) that adds energy into the pre-ionized gas into a controlled manner until the gas temperature is suitable for ignition ( $T=2000\text{-}3000 \text{ K}$ ). This technique is demonstrated by attempting ignition of various mixtures of propane-air and it is shown to have distinct advantages when compared to the classical approach: lower ignition energy for given stoichiometry than conventional laser ignition ( $\sim 20\%$  lower), extension of the lean limit ( $\sim 15\%$  leaner) and improvement in combustion efficiency. Moreover, it is demonstrated that the alignment of the two pulses influences the fluid dynamics of the early flame kernel. This finding has a number of implications for practical uses as it demonstrates that the flame kernel dynamics can be tailored using various combinations of laser pulses and opens the possibility for applications such as: flame holding and flame stabilization in high speed flow combustor (such as ramjet and scramjet engines), reducing flame stretching in highly turbulent combustion devices and increasing combustion efficiency for stationary natural gas engines. As such, the work presented in this dissertation should be of interest to a broad audience including those interested in combustion research, engine operation, chemically reacting flows, plasma dynamics and laser diagnostics.

## ACKNOWLEDGMENTS

I remember vividly the moment I decided to join Dr. Yalin's group at Colorado State University in order to pursue a PhD degree in the field of laser diagnostics and plasma assisted combustion. As I am writing this document that summarizes my entire doctoral work it is hard to realize how much I have grown as a researcher and as a person for the past 4.5 years. I started this adventure with great excitement and, to my own amazement, the enthusiasm has only grown as I progressed through my research. For this, I am extremely grateful to my advisor, Dr. Azer Yalin, for nurturing my curiosity and for giving me the intellectual freedom to discover my research passion. I will also like to thank him for taking a chance on me at a moment in time when I felt that my academic aspirations in the United States were coming to a close.

I would also like to thank Dr. Anthony Marchese, my co-advisor, for sharing his knowledge on combustion with me and for all his support over the years. Special thanks to my committee members as well - Dr. Xinfeng Gao, Dr. Alan Kirkpatrick, and Dr. Alan Van Orden - who have helped me throughout my doctoral program. I am very grateful for their time and valuable feedback.

I firmly believe that my research would not have been as successful without the continuous support and friendship of my colleagues at the Center for Laser Sensing and Diagnostics: Adam Friss, Soran Shadman, Laura McHale, Sean Walsh, Charles Rose, Betsy Farris, Jordan Rath, Isaiah Franka, and Brian Lee. I would also like to acknowledge Rachel VanOsdol who helped collecting the data presented in Chapter 4 of this dissertation during her summer internship in our lab. Thank you to the Powerhouse community for embracing me from the very beginning despite my idiosyncrasies. This place became my home away from home because of your friendships!

The doctoral degree is the culmination of 23 years of continuous education. Throughout the years I have encountered many teachers that mentored me and shaped the person I am today. I would like to take this opportunity to extend my gratitude to all the professors and teachers who taught me from first grade all the way to college. I can only hope that one day I will be able to match their level of dedication and passion. Two of those professors had a lasting impact on my academic trajectory and I would like to mention them here. First, I would like to thank my high school chemistry teacher, Carolita Cimpoca, for cultivating my passion for applied science through the many lab experiments we conducted together. More importantly, she was one of the very few that encouraged me to pursue my passion. Second, I would like to thank Dr. Radu Rugescu, my undergraduate advisor, for selflessly and patiently teaching me almost everything I know about rocket propulsion. I will never forget the countless evenings that Prof. Rugescu spent with me at the lab explaining in the greatest of detail the complexities of rocket engines, orbital mechanics, and rocket design. It is largely thanks to him that I felt inspired to pursue a graduate degree.

I came to the United State of America with the dream of becoming a world expert in my field of study and with the ambition that one day I can push the boundary of human knowledge a little bit further. I would like to thank the Romanian Fulbright Committee for believing in my dream and, more importantly, for funding my first 2 semesters of graduate education in the United States. Without their financial support, I would have never left my home country in the pursuit of my academic goals.

Above all, I am grateful to my wife, Adina Dumitrache, for her love and patience. The sacrifices she made to join me in the United States and her unwavering support every step of the way can never be repaid. I can only say that I love you and that I look forward to the many years to come together!

Last but not least, I need to thank to my superhero mother, Maria Birzache, without whom this incredible journey would not have been possible. I was born and raised by a single mother in a small city of a similarly small country. For me to be able to come to the United State of America and complete the highest degree in academia is nothing short of a miracle. This would not have happened without the confidence and the unconditional love of my mother who has never stopped believing even when everybody else doubted us.

Mama, nimic nu este imposibil!

## TABLE OF CONTENTS

ABSTRACT.....	ii
ACKNOWLEDGMENTS .....	iv
LIST OF FIGURES .....	xii
CHAPTER 1: Introduction .....	1
1.1 Motivation.....	1
1.2 Literature Review.....	4
1.2.1 Historical Perspective .....	4
1.2.2 Review of Laser Breakdown Literature.....	5
1.2.3 Pre-ionization Plasma Investigations.....	7
1.2.4 Laser Ignition Literature .....	7
1.3 Dissertation Outline .....	10
CHAPTER 2: Physics of Laser Plasma Formation.....	13
2.1 Introduction.....	13
2.2 Multiphoton Ionization .....	16
2.3 Electron Avalanche Ionization.....	20
2.4 Plasma Growth and Electron Losses.....	25
2.4.1 Master Equation.....	25
2.4.2 Primary Ionization Mechanisms (MPI & EAI).....	26

2.4.3 Secondary Ionization Pathways .....	26
2.4.4 Electron Diffusion.....	27
2.4.5 Recombination .....	29
2.4.6 Attachment.....	31
 CHAPTER 3: Threshold Characteristics of Ultraviolet and Near-Infrared Nanosecond Laser Induced Plasmas.....	
3.1 Description of Experimental Procedure.....	33
3.1.1 Optical Layout .....	33
3.1.2 Energy Absorption.....	35
3.1.3 Plasma Emission .....	35
3.1.4 Rayleigh Scattering.....	35
3.1.5 Schlieren Imaging .....	37
3.2 Results & Discussions.....	39
3.2.6 Energy Absorption Study.....	39
3.2.7 Plasma Luminosity & Emission Spectra.....	41
3.2.8 Rayleigh Scattering Thermometry.....	44
3.2.9 Plasma Density Measurements .....	46
3.2.10 Plasma Growth Model .....	48
3.2.11 Schlieren Imaging of Laser Plasma .....	50
3.2.12 Overlapped UV and NIR pulses .....	52

CHAPTER 4: Laser Ignition of Propane-Air Mixture Using Dual-Pulse Pre-Ionization .....	54
4.1 Description of Experimental Procedure.....	55
4.1.1 Optical Layout .....	55
4.1.2 Data Collection .....	56
4.1.3 Pressure Data Analysis .....	57
4.2 Lean Limit & Combustion Efficiency .....	62
4.3 Flame Visualization Using OH* Chemiluminescence .....	65
4.3.1 Single-Pulse Laser Ignition.....	65
4.3.2 Dual-Pulse Laser Ignition .....	67
4.3.3 Flame Speed Enhancement.....	68
4.4 Control of Flame Kernel Aerodynamics.....	69
CHAPTER 5: Numerical Modeling of Laser Ignition.....	72
5.1 Mathematical Model.....	73
5.1.1 Governing Equations .....	73
5.1.2 Thermodynamic Relations.....	74
5.1.3 Transport Properties.....	76
5.2 Numerical Methods.....	78
5.2.1 Physical Properties of the Advection Problem .....	78
5.2.2 General Approach .....	83
5.2.3 Roe-Pikes Method.....	85

5.2.4 Source Problem.....	88
5.2.5 Time Marching Technique.....	89
5.2.6 Algorithm Steps .....	91
5.3 Test Problems.....	91
5.3.1 Spherical Explosion .....	92
5.3.2 Unsteady Couette Flow.....	95
5.4 Study of Spark Induced Hydrodynamics .....	98
5.4.1 Problem Setup.....	98
5.4.2 Shock Wave Propagation.....	103
5.4.3 Kernel Dynamics .....	106
5.4.4 Comparison with experiments .....	113
5.4.5 Implications for Laser Ignition .....	115
CHAPTER 6: Conclusions .....	116
6.1 Summary.....	116
6.2 Future Work .....	119
6.2.1 Dual-Pulse Pre-ionization.....	119
6.2.2 Other Applications for Dual-Pulse Pre-ionization.....	122
6.3 Final Thoughts .....	123
BIBLIOGRAPHY.....	124
Appendix A: Solution Procedure for Thermally Perfect Gas .....	140

Appendix B: Roe-Pikes Algorithm for the Advection Problem .....	143
B.1 Euler Equations .....	143
B.2 Algorithm .....	146

## LIST OF FIGURES

2.1:	Schematic of the different stages for laser induced breakdown using nanosecond pulses. (a) Multiphoton ionization, (b) electron avalanche ionization, (c) plasma growth, (d) blast wave propagation <sup>74</sup> . .....	14
2.2:	Diagrams describing the various photoionization mechanisms: (a) MPI, (b) 2+1 REMPI and (c) electron tunneling ionization.....	18
2.3:	Breakdown intensity by MPI for the four harmonics of the Nd:YAG in a pure N <sub>2</sub> gas mixture. The calculation neglects electron loss mechanisms.....	20
2.4:	Schematic diagram showing the two competing quantum processes through which an electron interacts with a photon during EAI: inverse bremsstrahlung absorption and stimulated emission. ....	22
2.5:	Breakdown intensity due to EAI at the four harmonics of the Nd:YAG in a N <sub>2</sub> gas mixture. ....	25
3.1:	Optical layout for the laser plasma formation experiment using UV and NIR pulses. The Rayleigh scattering setup used for measuring gas temperature is also shown. ....	34
3.2:	Optical layout demonstrating the use of a Z-type laser illuminated Schlieren imaging system (beam is shown in green) for visualization of UV and NIR laser generated plasma. The UV beam is shown in blue and the NIR beam in red <sup>102</sup> .....	39
3.3:	Scatter plots of energy absorption for UV (left) and NIR (right) laser induced plasmas as a function of incident laser pulse energy. Data is for air at the indicated initial pressures...	41
3.4:	Luminosity of laser induced plasmas at various laser energies for UV (left) and NIR (right) beams.....	43

3.5:	Optical emission spectrum from a NIR laser-induced spark (blue) and a UV plasma (orange). .....	44
3.6:	Gas temperature measurement using Rayleigh scattering after the UV pulse (left) and the NIR pulse (right). Measurements were made in air at $p_0=1$ bar, $T_0=300$ K.....	45
3.7:	Normalized Rayleigh signal through the center of the beam for an UV (left) and a NIR induced plasma. Inserts are the raw ICCD plasma images at time delay $200 \mu\text{s}$ for UV and $500 \mu\text{s}$ for NIR. For both pulses, at early times, an increase in signal intensity is observed at the center of the plasma due to Thomson scattering. ....	47
3.8:	Evolution of the electron number density in a plasma generated using UV and NIR pulses. The simulation was conducted at $p_0 = 1$ bar assuming a Gaussian pulse with 10 ns full-width at half-maximum. ....	50
3.9:	Schlieren image sequence showing the evolution of the plasma kernel for NIR pulse (top) and UV pulse (bottom). The laser energies used for these experiments are: $E_{1064\text{nm}}=80$ mJ and $E_{266\text{nm}}=20$ mJ. ....	51
3.10:	Gas Temperature vs. laser energy for the 1064 nm beam and the dual pulse. Temperatures are reported at $50 \mu\text{s}$ after the end of the pulse. Initial conditions are $p_0=1$ bar and $T_0=300$ K.....	53
3.11:	Schlieren Images of Dual-Pulse plasma. The laser energies were set to $E_{266 \text{ nm}}=22$ mJ, $E_{1064 \text{ nm}}=53$ mJ.....	53
4.1:	Optical layout used for the laser ignition experiments. Single-pulse laser ignition method uses solely the 1064 nm Nd:YAG, while the dual-pulse method uses overlapped beams from both the 266 nm and 1064 nm Nd:YAG lasers. ....	56
4.2:	Gas manifold used for preparing the propane-air mixtures.....	57

4.3:	Schematic of a general piston-cylinder system used in the control volume analysis to determine the rate of heat release during combustion.....	58
4.4:	Analysis of the pressure data collected during combustion. By assuming the pressure decay is primarily due to heat transfer one can estimate the average heat transfer coefficient....	62
4.5:	Pressure curves showing the ignition of propane-air mixture at various equivalence ratios for NIR laser spark induced ignition (left) and dual-pulse pre-ionization (right). Each curve represents the average of three tests and the shaded area is +/- one standard deviation. The initial conditions were in both cases $p_0=1$ bar, $T_0=323$ K.....	64
4.6:	Combustion efficiency for NIR laser spark ignition (red) and Dual-Pulse (blue) at various propane-air equivalence ratios. Each point represents the average of three tests and the error bars are +/- one standard deviation.....	65
4.7:	Flame kernel development during single-pulse ignition of propane air mixtures at $\phi=1.0$ (top), $\phi=0.7$ (middle), and $\phi=0.6$ (bottom). The third lobe separates from the main kernel and is a precursor to flame quenching for the lean mixtures. Each image frame has field of view: 22 mm x 16 mm.....	67
4.8:	Early flame kernel development during dual-pulse ignition of propane-air mixtures at $\phi=1.0$ (top) and $\phi=0.6$ (bottom). Note that no third lobe is observed in this case. Each image frame has field of view: 22 mm x 16 mm.....	68
4.9:	Normalized flame speed for a $\phi=1.0$ propane-mixture for the laser breakdown ignited mixtures (left) and dual-pulse (right). Error bars represent +/- one standard deviation.....	69
4.10:	Dynamics of the flame kernel based on the spatial overlap between the two laser pulses. The images were all taken at delay of 1 ms with respect to the laser firing. Inserts at the top right	

corner shows the spatial overlap of the UV (blue) and NIR (red) beam waists. (The beams in the middle insert are laterally offset for visual clarity.) .....	70
4.11: IR laser energy absorbed as a function of spatial overlap between the two pulses. Show in red is the IR pulse on its own. ....	71
5.1: Schematic showing the domain of dependence and range of influence of a disturbance in the case of an elliptic (a), parabolic (b) and hyperbolic (c) PDE's. The color gradient in (b) is meant to show the decreasing effect of the disturbance as time progresses. ....	80
5.2: Characteristic lines for the 1-D linear advection equation .....	81
5.3: Diagram depicting a non-linear wave becoming distorted as time progresses (a) and the characteristic lines at several points on the wave (b). ....	82
5.4: One-dimensional domain discretized using finite volumes .....	85
5.5: Finite volumes used for spatial discretization of the source problem. ....	89
5.6: Initial conditions for a 2-D spherical explosion with axis-symmetric boundary conditions. ....	93
5.7: Density contours of a spherical explosion test problem. CFL=0.7, Grid resolution was set to $400 \times 400$ . ....	94
5.8: Density variation along the radius of a spherical explosion for various grid resolutions. .	95
5.9: Grid sensitivity expressed here in terms of the average relative error. ....	95
5.10: Schematic of a Couette Flow showing the Boundary Conditions used in the numerical code. ....	97
5.11: Unsteady Couette Solution at various time delays. The exact solution is shown with solid line and the numerical solution with discrete dots. ....	97

5.12: Schlieren image of a dual-pulse laser plasma in atmospheric air at 500 ns after the pulse. Image shows the channel generated by the UV plasma and the spherical plasma growth induced by the addition of the NIR. ....	99
5.13: Initial temperature (left) and pressure (right) profiles for the symmetric hot kernel generated by the dual-pulse. ....	101
5.14: Initial temperature (left) and pressure (right) profiles for the asymmetric hot kernel generated by the dual-pulse. ....	101
5.15: Initial mesh size for the symmetric (left) and asymmetric (right) kernels. Boundary A is the axis of symmetry for both kernels, B' is boundary of symmetry and C, D are prescribed the ambient condition. ....	103
5.16: Pressure contours shown the evolution of the shock wave for the symmetric (top) and asymmetric(bottom) kernel. Note that the r-axis is stretched compared to the z-axis in all the plots. ....	105
5.17: Schematic explaining the dynamics of shock wave development for non-spherical bodies .....	105
5.18: Time history of the pressure evolution at the center of the domain .....	106
5.19: Temperature contours showing the kernel evolution for the symmetric (top) and asymmetric (bottom) kernels .....	108
5.20: (Left) Velocity field overlaid on top of temperature contours for the symmetric kernel at a delay of 1.5 $\mu s$ after the two pulses. The figure shows the development of initial vorticity inside the kernel. (Right) Zoomed-in inserts showing the misalignment of the density and pressure gradients which leads to the formation of a barotropic instability.....	110

5.21: Velocity field overlaid on temperature contours for the symmetric kernel at 50  $\mu s$  delay.  
This shows the development of two counter-rotating vortices inside the toroid..... 111

5.22: Temperature contours of the symmetric kernel at 1 microsecond after the dual-pulse. Also  
shown in this figure is the position of the shock wave. Note that the trailing edge of the  
shock wave is much closer to the kernel than the leading edge. .... 112

5.23: (a) Velocity field of asymmetric dual-pulse kernel at 5  $\mu s$  and (b) at 300  $\mu s$ . .... 112

5.24: (a) Schlieren images depicting the evolution of a plasma kernel between two electrodes and  
(b) synthetic Schlieren images showing similar dynamics for the hot kernel generated by  
the dual-pulse symmetric case. Experimental Schlieren is from Kono et al.<sup>67</sup> ..... 114

5.25: (a) Experimentally obtained Schlieren images showing the collapse of the plasma kernel  
and the formation of the third lobe. (b) Synthetic Schlieren images showing very similar  
dynamics..... 115

# CHAPTER 1:

## Introduction

### 1.1 Motivation

Laser generated plasma has found a variety of applications in combustion devices. Recent advances in laser technology and fiber optic spark delivery systems are contributing to an increased interest in practical laser ignition systems for industrial ground based turbines<sup>1-5</sup>, aero-turbines<sup>6,7</sup>, rocket engines<sup>8-10</sup> or scramjet engines<sup>11-13</sup>. Several research groups have investigated the feasibility of replacing traditional electrical spark plug systems used in internal combustion engines with laser ignition systems<sup>14-18</sup>. Experimental results indicate many potential advantages over conventional ignition systems, including greater control over the location and timing of the ignition kernel inside the engine. Also, due to its electrodeless configuration, it eliminates problems such as spark plug erosion (present especially at high pressures) and reduces the possibility of flame quenching due to heat loss through the electrodes. Finally, because of the different mechanism of plasma formation, laser induced breakdown has been shown to lead to higher plasma temperatures than conventional sparks. All of the aforementioned advantages can potentially contribute to leaner engine operation with reduction in NO<sub>x</sub> formation<sup>19</sup>, higher pressure engine operation, and more reliable hardware systems.

In general, there are four types of laser ignition as described by Ronney<sup>20</sup>:

1. *Non-resonant breakdown*: in which laser plasma is formed by tightly focusing a high-power laser beam until the intensity (or the electric field strength) is high enough to cause breakdown of the gas molecules at the focus. Typical laser intensities values for gas breakdown

are on the order of  $\sim 300 \text{ GW/cm}^2$  at NIR wavelengths. The main mechanisms that govern the plasma formation using this technique are: multi photon ionization (MPI) that leads to the formation of the initial free electrons, and electron avalanche ionization (EAI) in which the free electrons are accelerated through the inverse bremsstrahlung process and generate further ionization through collision with gas molecules.

2. *Thermal ignition:* In general, this method involves heating the combustible mixture through laser excitation of a vibrational or rotational mode of the gas molecules. The subsequent quenching of the excited states leads to gas heating. This method does not require the generation of a plasma to serve as an ignition source.

3. *Resonant breakdown:* The laser wavelength is chosen such that ionization of a particular molecular species is achieved (usually through a resonant multi-photon ionization scheme). This leads to plasma formation, much like in case the case of non-resonant breakdown, but the energy is coupled more efficiently into the plasma (due to its resonant nature) and thus requires less energy overall.

4. *Photochemical ignition:* Gas dissociation is achieved through the absorption of photons by target molecules. This leads to the formation of important radicals that can initiate the combustion event.

It is important to note that the last three methods generally require wavelength-specific laser sources making their practical implementation more challenging. The most common laser ignition method involves the generation of laser sparks through non-resonant breakdown of the gas molecules. But while creating laser sparks for ignition presents several advantages over the classical capacitive spark plugs (i.e.: elevated flame speeds, freedom in positioning the plasma kernel inside the combustion chamber or elimination of spark plug erosion), this approach also has

several disadvantages. The un-tailored plasma generates temperatures in excess of 100,000 K, almost two orders of magnitude to what it is required for achieving ignition in practical devices. Several studies have also shown that a blast wave is likely to follow the optical breakdown<sup>21-24</sup> and a significant part of the energy is consumed by the propagating wave<sup>25</sup>. It was also demonstrated that ignition near the lean limit is more difficult due to the high rate flame stretch, a phenomenon that is aggravated at low pressures<sup>26</sup>. Finally, the energy requirements for achieving optical breakdown represents the biggest challenge for making possible the practical implementation in real world applications. For example, the development of a fiber spark delivery system for engines requires the use of specialized fibers that can transmit high power laser pulses with minimal losses due to bending and vibrations while also maintaining a good beam quality at the fiber output.

The scope of this dissertation is to address some of the aforementioned disadvantages by developing a novel laser ignition technique using a dual-pulse pre-ionization scheme. This approach uses an initial ultraviolet (UV) laser pulse at 266 nm to provide pre-ionization (but not full breakdown) along with an overlapped near-infrared (NIR) pulse at 1064 nm to add energy to the pre-ionized gas. In this respect, the dual-pulse laser ignition technique is a combination between the non-resonant breakdown and thermal ignition techniques described above. However, the dual-pulse approach presents certain advantages when compared with the two techniques. Since full breakdown is not achieved, the optical power required is considerably smaller than for the non-resonant breakdown technique. Moreover, gas heating is achieved without tailoring the laser wavelength to the gas mixture which represents a big advantage compared to the typical thermal ignition systems in which specialized lasers are required.

The dual-pulse method is demonstrated for laser ignition of various fuel-air mixtures with the aim of decreasing the lean flammability limit, increase combustion efficiency and reduce the energy required for ignition at a given equivalence ratio compared to non-resonant breakdown laser ignition. Also part of the motivation for this research is to develop a better understanding of the plasma physics phenomena involved in the generation of weakly ionized plasma. In particular, the focus is on demonstrating the ability to tailor the plasma parameters (temperature, electron number density, plasma size) as well as understanding how this influences the early flame kernel development.

## **1.2 Literature Review**

### **1.2.1 Historical Perspective**

The study of electrodeless gas discharges at optical frequencies is a relatively recent field coming into existence shortly after the construction of the first Q-switched high power laser capable of generating “giant” pulses. The first report on laser induced breakdown was made in February 1963, at the International Congress on Quantum Electronics in Paris by Maker, Terhune and Savage<sup>27</sup>. The authors report that, when the beam from a ruby laser emitting at 694 nm is focused using a converging lens, a spark is generated around beam waist similar to what is observed in the case of capacitive discharge devices. The discovery of laser “sparks” essentially lead shortly thereafter to the development of a new branch of quantum mechanics that deals with the theory of multiphoton processes. One of the first comprehensive descriptions of the phenomena is given by the soviet physicist Yuri Raizer who discusses in detail the theory responsible for laser-induced breakdown in his work published in 1965<sup>28</sup> later also translated in English in his book published in 1977<sup>29</sup>. Other early reports include DeMichelis who reviewed the topic in 1969<sup>30</sup> and Morgan who has investigated the role of de-ionization processes such as diffusion recombination

and radiative losses in laser plasmas and compiled a set of early breakdown experiments<sup>31</sup>. More recent reviews include Radziemski and Cremers's review book on the various modern applications of laser plasmas such as Laser Induced Breakdown Spectroscopy (LIBS) or laser vaporization of metals and ablation<sup>32</sup>.

When it comes to the use of laser plasma for combustion applications, the first successful demonstration of laser spark ignition in internal combustion engines is reported by Dale et al.<sup>33</sup> in 1977. The authors used a CO<sub>2</sub> laser operating at 10.6  $\mu\text{m}$  to generate a laser spark inside of the cylinder of an ASTM-CFR engine. Their investigation showed that laser ignition lead to less cycle-to-cycle variation (which lead to a decrease in CO and HC emissions) and an increase in flame speed when compared to capacitive ignition devices. More recent studies have expanded on these initial findings and focused on other aspects of laser ignition such as extension of flammability limit, minimum ignition energy or the stochastic nature of the minimum energy required to achieve gas breakdown.

### **1.2.2 Review of Laser Breakdown Literature**

Analyzing the threshold behavior of laser induced plasma represents one of the main topics discussed in this dissertation (see Chapter 3). The existence of a threshold laser intensity for plasma formation is widely observed for NIR and visible laser pulses, and is variously defined in literature by the naked eye observation of a visible plasma glow<sup>34</sup>, a threshold of total electron number (e.g.  $N_e \sim 10^{13}$ )<sup>29</sup> or a threshold ionization fraction (e.g.  $N_e/N \sim 10^{-3}$ )<sup>31,32</sup>. For widely used Q-switched pulses with typical duration of  $\sim 10$  ns, attainment of the breakdown threshold depends on both the plasma growth rate and pulse duration, provided initial seed electrons are present in the focal volume. The breakdown threshold has been measured by several authors<sup>35,36</sup> at NIR and visible wavelengths. For example, Phuoc et al. studied laser-induced breakdown thresholds and their

pressure dependence for combustion gases at  $\lambda=532$  nm and  $\lambda=1064$  nm and found a stronger pressure dependence for 532 nm pulse, suggesting the importance of diffusion losses<sup>35</sup>. A study by Buscher et al.<sup>36</sup> investigated the frequency dependence of the breakdown threshold of several inert gases at the first and second harmonics of the ruby and neodymium lasers and reported monotonically increasing breakdown intensity with laser optical frequency. Results at these frequencies (NIR and VIS) are explainable by avalanche cascade ionization theory. As shown by Raizer, for cascade ionization driven plasmas, one expects a frequency dependence of the threshold intensity of the type:  $I_{th} \sim \nu^2$ , where  $\nu$  is the laser frequency<sup>37</sup>. However, Buscher et al. observed a decline of the threshold intensity for  $\lambda=350$  nm (second harmonic of the ruby laser) which they attributed to the increased MPI contribution in the ionization process. Several investigations<sup>38-40</sup> have reported different breakdown trends for Nd:YAG harmonic wavelengths (i.e. 1064, 532, 355, 266 nm) which may be due to difficulties in determining laser spot sizes, different pressures and focusing configurations, and differing breakdown criteria, particularly for the UV, as it will be addressed in this dissertation. There have been several recent reports of nanosecond UV laser plasma formation with thresholds substantially lower than those in the VIS and NIR (lower than predicted by cascade theory). Zvorykin et al. employed a KrF laser operating at  $\lambda=248$  nm to form weakly ionized plasma channels for lightning control<sup>41</sup>. Measurements of electron number density showed a continuous increase with laser intensity from  $n_e \sim 10^8$  cm<sup>-3</sup> at  $I \sim 1$  MW/cm<sup>2</sup> to  $n_e \sim 10^{15}$  cm<sup>-3</sup> at  $I \sim 100$  GW/cm<sup>2</sup>. In another study, Way et al. used an ArF excimer laser at  $\lambda=193$  nm to generate low temperature ( $T \sim 1000$  K) atmospheric air plasmas at intensities of  $\sim 5.5$  GW/cm<sup>2</sup> ( $E = 280$  mJ)<sup>42</sup>. This dissertation work builds on past research by presenting an experimental comparison of the breakdown threshold characteristics for laser plasma formation in air using the

fourth harmonic (UV,  $\lambda=266$  nm) and fundamental output (NIR,  $\lambda=1064$  nm) of the Nd:YAG laser in Chapter 3.

### **1.2.3 Pre-ionization Plasma Investigations**

Gas pre-ionization techniques have been studied by other research groups in the past. Shneider et al. conducted a numerical study of laser induced plasma filaments using femtosecond laser pulses for microwave guiding<sup>43</sup>. Simulations show that if an overlapped NIR pulse follows the pre-ionization, the waveguide lifetime can be extended by suppressing electron attachment and dissociative recombination reactions in the plasma. Additionally, it was also shown that heating can occur in the channel due to inverse bremsstrahlung absorption. Zhou et al. have shown experimentally that a similarly pre-ionized plasma channel can be revived several milliseconds after its initial decay by overlapping a second NIR laser pulse<sup>44</sup>. In contrast, a study by Starikovskiy et al. demonstrated that laser breakdown can be suppressed at low pressures if the initial gas is pre-ionized<sup>45</sup>. The suppression is caused by the fast electron energy transfer away from the focal region (due to free electron diffusion at low pressures). The use of pre-ionization for laser ignition of methane-air mixtures was also demonstrated by Michael et al.<sup>46</sup>. In their work, seed electrons were generated by a femtosecond laser pulse with a subcritical microwave pulse providing energy addition. Dual-pulse approaches have also been examined in laser induced breakdown spectroscopy (LIBS), generally to enhance signal levels, but in configurations where the first pulse produces fully ionized plasma<sup>47</sup>.

### **1.2.4 Laser Ignition Literature**

From a practical point of view, commercial adoption has not yet occurred in part due to the need for fully reliable systems, potentially with fiber optic delivery<sup>48-52</sup>, which should be based on relatively inexpensive laser sources. There has been substantial recent progress towards

appropriate sources, for example VCSEL pumped Nd:YAG lasers<sup>53</sup> and ceramic microchip lasers<sup>54,55</sup>. Improvements in plasma energy coupling, as demonstrated in this work through the development of the dual-pulse approach, can benefit and expand the applicability of different laser sources to practical ignition systems. Past research on laser ignition has looked at the extension of the lean limit and minimum ignition energy. Weinrotter et al.<sup>56</sup> were able to ignite methane–air mixtures as lean as  $\phi = 0.52$ , while Gupta et al.<sup>14</sup> noted a lean limit of  $\phi = 0.5$  under laser ignition (compared to  $\phi = 0.6$  from a conventional capacitive discharge ignition system). One of the first laser-ignition studies on methane–air conducted by Phuoc and White<sup>15</sup> found a lean limit corresponding to an equivalence ratio of  $\phi = 0.66$ .

Several studies have also looked at the minimum ignition energy (MIE) for laser ignition. For example, Lee et al.<sup>57</sup> have looked at the MIE for several hydrocarbon mixtures: propane, dodecane and Jet-A fuel. They report a MIE for laser ignition on the order of ~2-3 mJ at 1 atm which is consistently higher than using electric spark plugs. Lewis and von Elbe report ignition energies for spark plugs an order of magnitude lower (~0.4 mJ)<sup>58</sup> under similar experimental conditions. Beduneau et al.<sup>59</sup> performed a parametrical study to characterize the effects of equivalence ratio, flow velocity and lens focal length on the laser ignition of methane/air mixture. The authors also found that laser ignition requires much higher energies than spark plugs. However, the energy requirements between the two ignition methods become negligible at the lean and rich limits. Flow instabilities and longer focal length can further increase the MIE. Other parameters that influence the MIE such as spark size and energy deposited inside the focal volume have also been investigated by Lim et al.<sup>60</sup> Normalizing the ignition energy based on these two parameters seems to bring the MIE values closer to those observed by Lewis and Von Elbe using spark plugs. Another important aspect for laser spark ignition is the stochasticity of the ignition

process. Dumitrache et al.<sup>61,62</sup> have demonstrated laser ignition of methane-air mixtures inside a rapid compression machine and found that the probability of ignition follows a logistic distribution with laser energy. It is posited that the stochasticity of the breakdown process which leads to a variation in energy absorbed into the spark plays an important role in determining the successful ignition of a combustible mixture. All of the findings presented above further motivate this dissertation work. To complement existing literature, the ability of the dual-pulse to ignite leaner fuel-air mixtures with lower MIE than laser spark ignition is investigated.

There have also been several studies focusing on the fluid mechanic aspects of flame kernel formation under laser breakdown ignition. Morsy et al.<sup>63</sup> showed numerically that a toroidal shaped flame kernel is formed in the wake of the shock wave prompted by the laser spark. Typically, the flame ignited using this method develops a front lobe that appears on the upstream (incident) laser side and propagates toward the laser source. The front lobe is often referred to as the third lobe, since the toroidal kernel resembles a two-lobe structure in two-dimensional cross-sectional images. The three lobe structure has been observed in air as well as both flammable and non-flammable mixtures<sup>23,26,64</sup>. Morsy et. al. noted that it is possible for the third lobe to separate from the main flame kernel but do not discuss this in connection with flame quenching as we investigate here. The formation mechanism of the third lobe is first discussed by Bradley et al.<sup>26</sup> who suggest that the third lobe forms due to an asymmetric inward flow induced by the passing rarefaction waves. The interaction between the rarefaction and the expanding hot gas behaves as a Taylor instability within the kernel, generating a pair of counter-rotating vortices – one at the upstream (laser incident) side and one at the downstream side of the kernel. Owing to the non-uniform energy addition around the beam waist (with more energy absorbed towards the laser<sup>29</sup>), the downstream vortex is stronger and forms the third lobe through the entrainment of the surrounding cold gas in

an axial jet which impinges upon and expels the hot gases in the plasma core. Ghosh and Mahesh also discuss the dynamics of vorticity in laser-induced sparks as observed in their numerical simulations<sup>65</sup>. They suggest that at short time scales (prior to plasma recombination) vorticity is generated through a baroclinic torque induced in the flow by misaligned pressure and density gradients, while at longer time scales additional vorticity is created by roll-up of the plasma core (similar to the model of Bradley et al.). Similar mechanisms to those discussed here (in the context of laser ignition) are also responsible for kernel dynamics induced by conventional spark plugs and in nanosecond discharges between electrode pairs. However, in these cases the energy deposition is more symmetric so that two matched vortex rings persist and no third lobe forms<sup>66-69</sup>. Finally, Endo et al. have reported a comparative study between laser breakdown ignition and discharge spark plugs indicating that the plasma-driven fluid dynamics play an important role in flame kernel augmentation<sup>64</sup>. They suggest that flame vorticity entrains the surrounding combustible mixture which leads to an increase of the effective kernel energy in the early stages of flame development. The fluid dynamics effects induced by the dual-pulse laser ignition technique are investigated here for the first time.

### **1.3 Dissertation Outline**

This dissertation develops a novel laser ignition technique based on a dual-pulse pre-ionization technique. There are three main directions that are pursued in order to form a unified understanding of how this new technique can improve on current laser ignition technology: 1) investigation of the plasma characteristics at various laser wavelengths, 2) demonstration of the new technique for ignition of fuel-air mixtures and comparison with the reference non-resonant laser breakdown ignition method, 3) understanding the impact of the thermal/fluid dynamic processes that accompany plasma recombination on the early flame kernel development. The

dissertation achieves these goals through a combination of experimental investigations and numerical modeling. As such, the dissertation is organized in six chapters. Chapter 1 gives a motivation for this work and covers the existing literature on the topics of laser breakdown and laser ignition. Chapter 2 is devoted to the physics of laser plasma formation. The main goal of this chapter is to understand what are the conditions under which successful breakdown can be achieved. The mechanisms of multiphoton ionization and electron avalanche ionization are treated theoretically and their role in electron generation and plasma growth at various laser wavelengths is explained. Additionally, the various kinetics pathways involved in the ionization process are presented and the main electron loss mechanisms are outlined. Chapter 3 presents an experimental investigation of the threshold characteristics of ultraviolet (UV)  $\lambda=266$  nm and near-infrared (NIR)  $\lambda=1064$  nm nanosecond laser generated plasma in ambient air. For UV pulses at the conditions studied, energy absorption by the plasmas increases gradually with laser pulse energy and the absorption of UV radiation does not necessarily result in visible plasma emission. For the NIR induced plasmas, the energy absorption profile is far more abrupt. In contrast with UV, the absorption of NIR radiation is always accompanied by intense optical emission. The contrast in the UV and NIR plasma threshold behavior are attributed to differing roles of avalanche ionization and multiphoton ionization. These experimental findings are further endorsed by a numerical simulation of the electron rate of growth under UV and NIR radiation. Finally, differences in the fluid dynamics for UV versus NIR pulses are shown with Schlieren imaging. Chapter 4 builds upon these findings and proposes a new laser ignition technique based on the overlap of the UV and NIR pulses. The new technique is successfully demonstrated for the ignition of propane-air mixtures at various equivalence ratios. A comparison with the classical laser spark ignition method shows that the dual-pulse technique is superior leading to a reduction in the minimum ignition

energy, lowering of the lean flammability limit and an increase in combustion efficiency. Another important experimental finding presented in this chapter is that the plasma induced flow can have a big impact on the flame kernel aerodynamics. The content of chapter 5 is motivated by this latter finding. A custom computational fluid dynamics (CFD) code is developed to study the flow field induced by the laser plasma. It is shown that the flow pattern is primarily dictated by how the laser energy is deposited along the optical axis. If the energy deposition is not homogenous (corresponding to a slight misalignment between the focal points of the two beams) then a third lobe is formed propagating towards the laser source. In contrast, if the energy is deposited homogeneously around the waist the flow develops into a symmetrical toroidal shape with no third lobe. Instead, a stagnation plane is observed to appear at the center of the kernel. This ensures that the temperature at the core stays higher for longer periods. The dissertation concludes with Chapter 6 in which the main findings are summarized in the form of conclusions. The main implications of the findings reported here are explored in this chapter as well. Finally, several recommendations and directions of future research are presented.

## **CHAPTER 2:**

### **Physics of Laser Plasma Formation**

#### **2.1 Introduction**

The main concern of this chapter relates to the physical and mathematical description of the optical breakdown phenomenon. The mechanisms of optical breakdown have been studied extensively and are discussed at length in the books of Raizer<sup>29,37</sup>, Bekefi<sup>70</sup> and Radziemski and Cremers<sup>32</sup> and reviews by Ostrovskaya and Zaidel<sup>71</sup> and Morgan<sup>31</sup>. Two principal ionization mechanisms lead to plasma formation and growth: multiphoton ionization (MPI) and electron avalanche ionization (EAI). The initial generation of free electrons is predominantly by MPI whereby a neutral gas molecule becomes ionized through absorption of a sufficient number of photons within the excitation lifetime (though some free electrons may also be present due to thermal ionization and cosmic ray excitation). The MPI process is shown schematically in Figure 2.1-a and it occurs with greater probability for at shorter wavelengths as fewer photons are required to overcome the ionization potential of the gas molecule. For nanosecond pulses, the initial seed electrons generated through MPI rapidly gain energy through inverse Bremsstrahlung absorption of laser radiation (see Figure 2.1-b) and, upon collision with surrounding molecules, induce further ionization into the gas. The rate of exponential plasma growth, characteristic to the formation of laser sparks, is dictated by the competition between EAI and various loss mechanisms, such as electron attachment, elastic and inelastic collisional losses, recombination, and diffusion. It is during this phase that most of plasma heating takes place. During the final part of energy deposition, the plasma is observed to propagate along the beam path growing towards the laser

source (Figure 2.1-c). It is important to note that once the plasma has formed the energy required to propagate the discharge is much smaller than what is required for breakdown. Even in very weak electric fields the ionization spreads through the adjacent layers being aided by processes such as pressure wave heating, heat conduction, thermal radiation and electron diffusion<sup>29,72,73</sup>. The final stage of laser plasma development involves the formation of a blast wave that propagates outward from the main plasma kernel (Figure 2.1-d). One of the main challenges in studying the laser induced plasmadynamics comes from the fact that each process described above takes place on vastly different time scales. MPI requires sub-nanosecond time scales because it involves the excitation of virtual energy levels with each photon absorption. EAI takes place over longer time scales (nanosecond or larger) because it is a collisional ionization process. Finally, the blast wave formation and the plasma induced fluid dynamics take place over microsecond timescale.

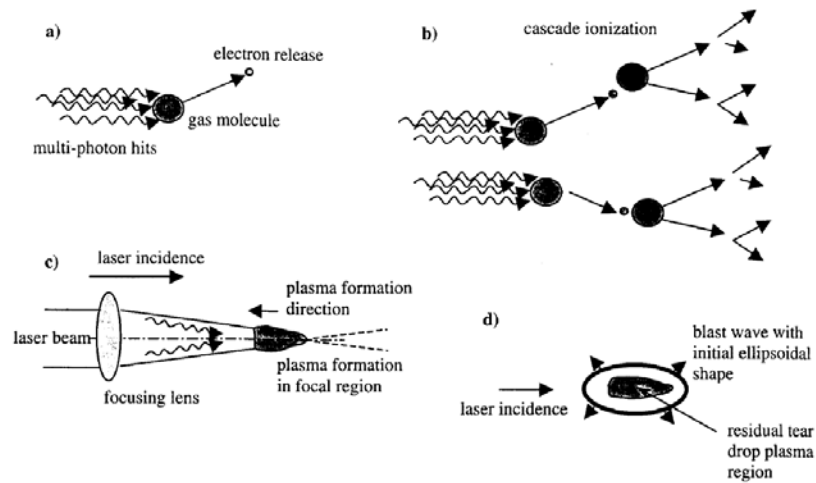


Figure 2.1: Schematic of the different stages for laser induced breakdown using nanosecond pulses. (a) Multiphoton ionization, (b) electron avalanche ionization, (c) plasma growth, (d) blast wave propagation<sup>74</sup>.

For sub-nanosecond pulses the mechanism governing plasma formation is somewhat different than the one described above. In the last few years, of particular interest was the study of plasma generated through the filamentation of femtosecond laser pulses. Owing to their short pulse

duration, no EAI is present and the gas ionization process is much more controllable being governed entirely by MPI. The femtosecond filament enables the propagation of a very narrow beam over great length without the support of a self-guiding mechanism. When the laser intensity is high enough ( $\sim 10^{13}$ - $10^{14}$  W/cm<sup>2</sup>), the phenomena leads to the formation of long weakly ionized plasma channels (also called filaments)<sup>75,76</sup>. This is due to the Kerr lensing effect that balances the MPI-induced defocusing tendency<sup>77</sup>. For this type of plasma, the acoustic wave that accompanies plasma cooling and recombination is observed to be much weaker than the typical blast wave associated with the nanosecond laser generated plasma<sup>78,79</sup>.

At the other end of the spectrum, if the pulse is very long (or even continuous) optical breakdown of gases cannot be achieved owing to the high peak intensity required for cascade ionization breakdown ( $I_{EAI\_breakdown} \sim 2 \times 10^{11}$  W/cm<sup>2</sup>)<sup>32</sup>. Thus, most common application of continuous wave (CW) lasers is on laser-sustained plasma whereby a plasma generated by other means (short pulses, capacitive discharges etc) is maintained at steady state by the use of a high-power CW laser. This type of plasma is also referred in literature as a continuous optical discharge and shares many characteristics with the other gas discharges mentioned above<sup>80</sup>. The mechanism involves the continuous replenishing of free electrons through inverse bremsstrahlung absorption to counteract various loss mechanisms (such as electron diffusion, recombination or attachment). Additionally, if the laser radiation frequency is greater than the plasma frequency the beam can propagate deep into the plasma kernel becoming absorbed at high intensities near the focus. This enables one to generate a steady state high density laser plasma.

In this dissertation, the main focus is on nanosecond pulses. However, the other types of laser plasma will be mentioned briefly for comparison purpose where appropriate.

## 2.2 Multiphoton Ionization

The creation of initial electrons by laser radiation is most commonly achieved through multiphoton ionization of atoms or molecules. In this section, the theory of MPI is first developed intuitively using statistical mechanics arguments. Later, the result of this analysis is compared to more complex models that are found in literature.

Multiphoton ionization involves the quasi-simultaneous absorption of several photons by a gas molecule or atom. The main requirement for ionization to occur is that the total energy of the absorbed photons needs to be larger than the ionization potential of the particle. The MPI reaction can be described as follows:



Where  $n$  represents the number of photon required to photoionize the molecule and  $h\nu$  is the energy of one photon. The ionization mechanism, shown schematically in Figure 2.2-a, can be explained as follows: a high-power laser pulse is focused using a lens to achieved high irradiance at the beam focal spot. Provided that the flux density is high enough, multiple photons can interact with the gas molecule that is initially in its ground state. If the photon energy does not match any of the molecule's allowed quantum transition (energy levels) then absorption of the photon energy can only take place to a virtual state. However, the electron cannot remain in that state. In fact, the electron residence time in a virtual state is governed by Heisenberg's uncertainty principle and it is related to the photon energy:  $\Delta t = h/h\nu$ <sup>81</sup>. If a second electron is absorbed during this time, then the electron will be excited to a higher virtual energy state corresponding to:  $2h\nu$ . Depending on the molecular structure of the gas to be ionized and the laser frequency used, multiple photons are needed to overcome the ionization potential, with each subsequent photon absorption requiring a decreasing residence time in a virtual state (for the  $n^{\text{th}}$  photon in an MPI scheme the residence

time becomes  $\sim 1/n\nu$ ). As a consequence, the MPI process takes place over very short time scales (sub-nanoseconds) and it is a strong function of the gas mixture and laser wavelength. A shorter laser wavelength (more energetic photons) yields a shorter residence lifetime to a given virtual state but will require fewer photons overall to overcome the molecule's ionization potential.

Another related ionization mechanism could take place if the photon energy matches one of the quantum energy levels of the gas molecule. In this case fewer photons are required for achieving ionization and the residence time increases (since the transition is allowed). Such mechanism is called resonant-enhanced multi-photon ionization (or REMPI) and, if the conditions are met for it to take place, its probability is higher than MPI<sup>29,82</sup>. However, REMPI is a much more challenging process to achieve because it requires tailoring the laser wavelength to the gas mixture. An example of a 2+1 REMPI ionization scheme is shown in Figure 2.2-b. Here, two photons are required to reach an intermediate excited state ( $M + 2h\nu \rightarrow M^*$ ) and a third one takes the electron above the ionization threshold ( $M^* + h\nu \rightarrow M^+$ ). Usually high power tunable lasers are required for achieving gas ionization through REMPI.

At longer wavelengths in the IR ( $\lambda > 1 \mu m$ ) photoionization is enabled by yet another mechanism. If the laser irradiance is very high ( $\sim 10^{15} W/cm^2$  for  $\lambda = 1 \mu m$ ) ionization can be induced by electron quantum tunneling. If the electron in an atom or molecule absorbs sufficient energy it can pass through the quantum potential well and the particle becomes ionized<sup>83</sup>. It is largely agreed that for very long radiation wavelength (especially in microwaves) photoionization can only take place through electron tunneling<sup>84,85</sup>. A schematic of the tunneling photoionization is shown in Figure 2.2-c.

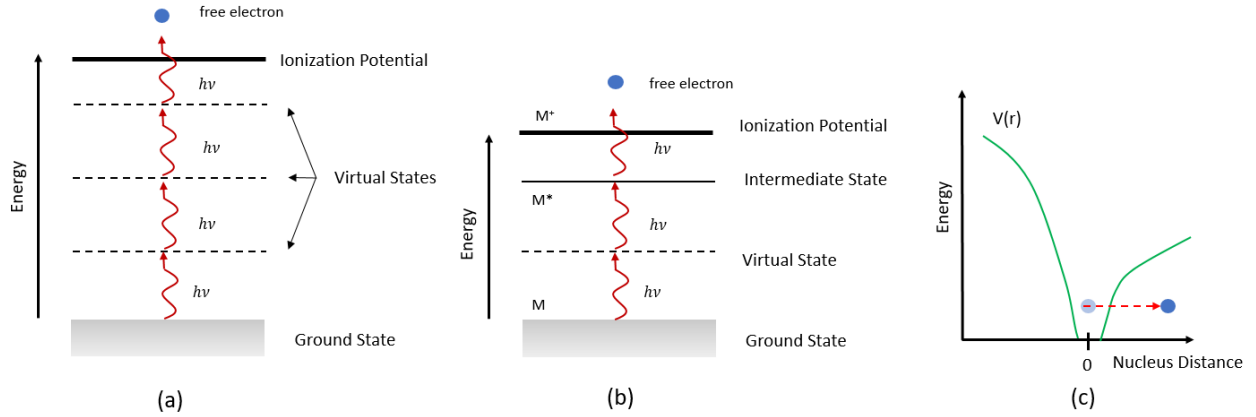


Figure 2.2: Diagrams describing the various photoionization mechanisms: (a) MPI, (b) 2+1 REMPI and (c) electron tunneling ionization

In the experimental work presented in this dissertation, it is believed that MPI is the main pre-ionization mechanism present<sup>86</sup>. A mathematical expression for the probability of MPI can be derived based on statistical mechanics arguments that follow naturally from the discussion presented in the previous paragraph. Let us consider the interaction between the laser beam and a molecule or atom. The photon flux at the location of the beam waist is given by:  $\phi_\nu$  and the photon energy is:  $h\nu$ . The number of photon required to ionize a molecule through MPI is therefore:

$$n = \frac{E_p}{h\nu} \quad (2.2)$$

where,  $E_p$ , represents the energy required to pass the ionization potential of the particle. If we assume that the excitation is purely a collisional process then we can define a sectional area in the close vicinity of the particle that has to be crossed by the photons in order to excite that particle.

If this area is defined as  $\sigma$  then we know that, in general, the average number of photons crossing this area over a time interval,  $\Delta t$ , is given by:

$$n_{ph\_avg} = \phi_\nu \sigma \Delta t \quad (2.3)$$

According to Tozer<sup>87</sup> it is reasonable to assume that the probability of  $n$  photons crossing  $\sigma$  in time  $\Delta t \sim 1/\nu$  obeys a Poisson distribution (which implies that the photon distribution is random over

molecular/atomic distances). Using this argument, the probability for ionization of a single particle can be defined as:

$$p = \exp(-\phi_v \sigma / \nu) [(\phi_v \sigma / \nu)^n / n!] \quad (2.4)$$

If one is interested in determining the number of free electrons generated in a gas of density,  $N$ , over a laser pulse length,  $\tau$  then this can be obtained from Eq. (2.4):

$$n_e = (N \tau \nu) \times \exp(-\phi_v \sigma / \nu) [(\phi_v \sigma / \nu)^n / n!] \quad (2.5)$$

The reaction rate for MPI can also be obtained by dividing the probability by the time interval allowed for the excitation into the virtual state to take place:

$$W = \nu \times \exp(-\phi_v \sigma / \nu) [(\phi_v \sigma / \nu)^n / n!] \quad (2.6)$$

A similar expression for multiphoton ionization rate was obtained by Grey Morgan<sup>81</sup> who solved a system of rate equation for the upward and downward transitions from various virtual states. His derivation assumes that the cross-section for the photon excitation is the same for each virtual state and that the decay from each of these state is spontaneous within a lifetime governed by the uncertainty principle. The equation obtained is very similar to Eq. (2.6):

$$W = \left( \frac{\sigma}{h\omega^2} \right)^n \frac{2\pi\omega}{(n-1)!} \quad (2.7)$$

For practical applications, another important relation is the photon flux required to achieve optical breakdown (formation of laser spark) by MPI. This can be obtained from Eq. (2.5) by setting gas ionization fraction  $\delta = n_e / N = 0.001$  and solving for the flux  $\phi_v$ :

$$\phi_v |_{threshold} = \frac{\nu}{\sigma} \left[ \frac{\delta n!}{\tau \nu} \exp(\phi_v \sigma / \nu) \right]^{1/n} \quad (2.8)$$

The solution of the implicit equation (2.8) for the four harmonics of the Nd:YAG are plotted in Figure 2.1 below. Results indicate that the intensity required to achieve breakdown by MPI alone increases with the laser wavelength. Note that at the fundamental wavelength of the Nd:YAG ( $\lambda =$

1064 nm) the breakdown intensity is about an order of magnitude higher than at 266 nm. As it will be demonstrated in the next section, MPI is not the dominant mechanism for achieving optical breakdown at NIR laser frequencies.

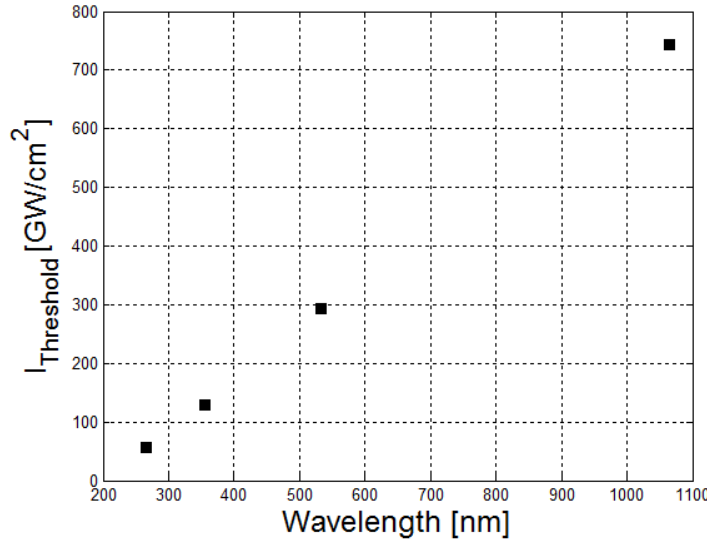


Figure 2.3: Breakdown intensity by MPI for the four harmonics of the Nd:YAG in a pure N<sub>2</sub> gas mixture. The calculation neglects electron loss mechanisms.

### 2.3 Electron Avalanche Ionization

It was noted in the previous sections that MPI is essential for the initial formation of seed electrons in a gas mixture (also referred as gas pre-ionization). However, for the successful formation of a laser spark (gas breakdown) MPI is not a sufficient condition in most cases. The main requirement for gas breakdown under intense laser radiation is the rapid multiplication of free electrons in order to counteract the various loss mechanisms such as electron diffusion, attachment or recombination. At optical frequencies, this is achieved through the process of electron avalanche ionization (EAI). This section is concerned with the development of a mathematical model describing the probability of EAI.

The electron avalanche (sometimes also referred in literature as the cascade growth) can be described by the following reaction:



Reaction (2.9) describes an avalanche because it leads to a net gain of electrons in the plasma. The probability of electron multiplication is governed by the rate at which the electrons gain energy in the electromagnetic field generated by the laser beam at the location of optical breakdown. In quantum mechanics, this process is called inverse bremsstrahlung (IB) absorption of radiation (from the German words bremsen = to slow down and strahlung = radiation). However, IB is not the only possible interaction between free electrons and laser radiation. A competing mechanism is present in the form of stimulated emission which acts like a quenching mechanism for EAI. This quantum mechanical description of avalanche ionization was treated in detail for the first time by Zel'dovich and Raizer<sup>28</sup> in their seminal work on cascade ionization of a gas by a light pulse published in 1965. Here only the main result will be presented. The rate of electron density growth can be described by solving the Boltzmann's kinetic equation for the electron distribution function in velocity space<sup>32</sup>:

$$\frac{\partial f(\varepsilon)}{\partial t} = n R(\varepsilon) + n \sum_j \int G_j(\varepsilon, \varepsilon') f(\varepsilon') d\varepsilon' \quad (2.10)$$

The first term in Eq. (2.10) represents the rate at which an electron gain energy in the EM field generated by the laser pulse. According to Zel'dovich and Raizer<sup>28,32</sup> this corresponds to:

$$R(\varepsilon) = K_{IB}(\varepsilon - h\nu) f(\varepsilon - h\nu) - K_{IB}(\varepsilon) f(\varepsilon) + K_{SE}(\varepsilon + h\nu) f(\varepsilon + h\nu) - K_{SE}(\varepsilon) f(\varepsilon) \quad (2.11)$$

Where  $K_{IB}$  and  $K_{SE}$  represent the inverse bremsstrahlung and stimulated emission rate coefficients.

A diagram of all four processes is shown in Figure 2.4 below.

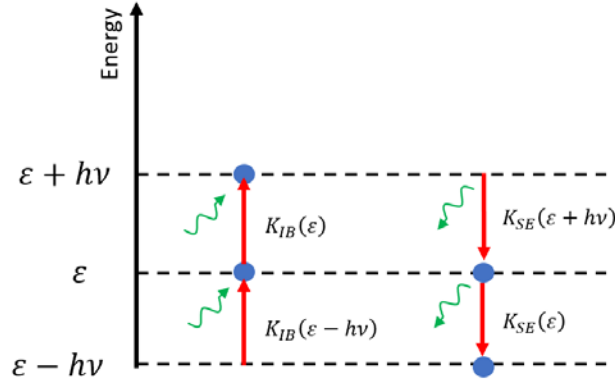


Figure 2.4: Schematic diagram showing the two competing quantum processes through which an electron interacts with a photon during EAI: inverse bremsstrahlung absorption and stimulated emission.

Various relations for the IB rate coefficient can be found in literature<sup>88,89</sup>. It is important to note that, depending on the plasma parameters, the dominant IB mechanism can change from electron-neutral IB (at  $T < 10,000$  K) to electron-ion IB ( $T > 10,000$  K)<sup>90,91</sup>. On the other hand, stimulated emission coefficient can be implied through detailed balance once the IB coefficients are known.

The second term in Eq. (2.10) represents the gain/loss of electrons upon collisions with molecules<sup>32</sup>:

$$G_j(\varepsilon, \varepsilon') = \left(\frac{2}{m_e}\right)^{0.5} [\varepsilon'^{0.5} \sigma_j(\varepsilon') \delta(\varepsilon - \varepsilon' + \varepsilon_j) - \varepsilon^{0.5} \sigma_j(\varepsilon) \delta(\varepsilon - \varepsilon')] \quad (2.12)$$

Electrons at energy,  $\varepsilon$ , can be generated from a collision between a molecule and an electron at energy  $\varepsilon' > \varepsilon$  (first term in Eq. (2.12)) or an electron at energy  $\varepsilon$  can be lost when the excited state  $\varepsilon'$  is formed (second term in Eq. (2.12)). The cross-section for impact ionization of molecules,  $\sigma_j$ , is obtained from experiments.

According to Raizer<sup>29</sup>, a simpler analysis for the rate of EAI can be conducted if the average electron energy is higher than the photon energy. This is valid in the microwave region but it can also be used for qualitative results at optical wavelengths. In this scenario, the motion of the

electron inside of an EM field induced by a laser beam can be described using classical mechanics.

From Newton's second law:

$$m_e \frac{d^2 \vec{x}}{dt^2} = -e\vec{E} - m_e \nu_m \vec{V} \quad (2.13)$$

Where the first term describes the oscillatory motion of the electron inside the electric field:  $\vec{E} = E_0 \exp(-i\omega t)$ . This is in fact the Lorentz force where we have neglected the contribution of the magnetic component (which is minimal in a laser field). The second term deals with the translational motion of the electron as a consequence of collisions with surrounding particles ( $\nu_m$  is the collision frequency). This term can be thought as acting like a "drag" because the electron is forced to slow down due to collisions with other particles in the field. By integrating Eq. (2.13) one obtains the velocity of the electron in the E-field:

$$\vec{V} = \frac{-ie\vec{E}}{m_e} [\omega + i\nu_m] \quad (2.14)$$

The rate of electron energy increase inside the field (i.e. the power gained by the electron) can be computed by taking the time average product between the E-field and the velocity vector:  $-e\langle \vec{E}\vec{V} \rangle$ .

Note that for complex numbers this is equivalent to:  $\langle \vec{E}\vec{V} \rangle = \frac{1}{2} \text{Re}\{E V^*\}$ , where  $V^*$  is the complex conjugate of the electron velocity. Substituting expression (2.14) into this gives the rate of electron energy increase in the laser field:

$$\frac{d\varepsilon}{dt} = \frac{e^2}{2m_e[\omega^2 + \nu_m^2]} \quad (2.15)$$

In the simplest scenario when all the electron loss mechanisms are ignored, the plasma growth rate due to EAI can be computed as follows:

$$\frac{dn_e}{dt} = \nu_i n_e \quad (2.16)$$

The ionization frequency,  $\nu_i$ , is governed by the time it takes for an electron to increase its energy from the ground state to the ionization potential,  $I_p$ :

$$\nu_i = \frac{1}{I_p} \frac{d\varepsilon}{dt} = \frac{1}{I_p} \frac{e^2}{2m_e[\omega^2 + \nu_m^2]} \quad (2.17)$$

An important quantity for practical applications is the E-field required to achieve gas breakdown through EAI. This can be obtained by integrating Eq. (2.16) over the laser pulse duration:

$$\ln\left(\frac{n_{e\_final}}{n_{e\_initial}}\right) = \int_0^{\tau_p} \nu_i dt \quad (2.18)$$

By considering a square pulse the integration can be done analytically very easily and a relationship for the root-mean-squared E-field required for breakdown becomes apparent:

$$E_{RMS}^2 = \frac{I_p}{e^2 \tau_p \nu_m} \ln\left(\frac{n_{e\_final}}{n_{e\_initial}}\right) m_e [\omega^2 + \nu_m^2] \quad (2.19)$$

Here the breakdown requirement is defined as:  $\frac{n_{e\_final}}{n_{e\_initial}} = 10^{13}$  the same as in the previous section when we looked at MPI. The breakdown intensity is plotted in Figure 2.5 as a function of laser wavelength. It is worth noting that for EAI, the breakdown intensity increases with photon energy. This is in contrast with the results obtained for MPI where higher energy photons increase the probability of ionization. Moreover, in the NIR range, the breakdown intensity for MPI is higher than it is for EAI. This suggests that in NIR most of the electrons generated in a laser spark come from avalanche ionization. Also important to note that, since:  $\nu_m \sim p$ , breakdown threshold decreases with increasing pressure:  $E_{RMS} \sim \frac{1}{\sqrt{p}}$ . This is an important result for the laser ignition applications because it shows that it is easier to generate laser sparks when engines are operated at higher pressure.

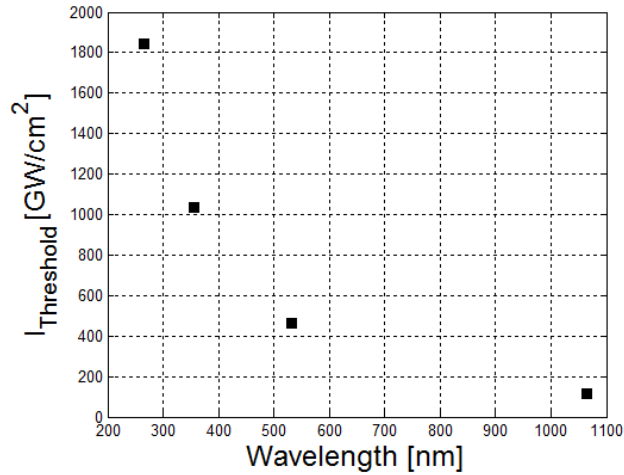


Figure 2.5: Breakdown intensity due to EAI at the four harmonics of the Nd:YAG in a N<sub>2</sub> gas mixture.

## 2.4 Plasma Growth and Electron Losses

### 2.4.1 Master Equation

The previous two sections of this chapter presented the mechanisms of electron generation in a gaseous mixture under laser illumination with complete disregard to any losses that might occur during the plasma formation period. However, optical breakdown is achieved when the electrons generated through a combination of MPI and EAI is higher than the various electron loss mechanisms that are present in the plasma. There are various definitions for the breakdown threshold as described in the literature survey section of this dissertation. In this work, the breakdown threshold is associated with the generation of a critical ionization fraction:  $n_e/n \sim 0.001$ .

The focus here is on evaluating the kinetics pathways involved in the ionization process and try to understand the conditions under which successful breakdown can be achieved. The rate of growth of electrons in a plasma is governed by the following master equation:

$$\frac{dn_e}{dt} = \nu_{EAI}n_e + \nu_{MPI}nI^m - \nu_Dn_e - \nu_{rec}n_e - \nu_{att}n_e \quad (2.20)$$

The subsection that follow describe each term in detail. An example calculation using Eq. (2.20) is given in CHAPTER 3: when discussing the threshold characteristics of UV and NIR laser plasma.

### 2.4.2 Primary Ionization Mechanisms (MPI & EAI)

The first term represents the rate of generation of electrons through electron avalanche ionization. Note that EAI cannot take place in the absence of free electrons already present in gas that were either generated through a photoionization mechanism or background ionization. This is illustrated in Eq. (2.20) by the dependence on electron number density,  $n_e$ . The EAI rate,  $\nu_{EAI}$ , can be computed using the models presented in the previous section (see Eq. (2.17), for example) but other models have been proposed in literature by Shneider<sup>92</sup> or Bekefi<sup>70</sup> which have also shown agreement with experiments. The second term describes the rate of ionization through multiphoton ionization. The MPI process dependence on laser intensity is given by a power law:  $I^m$ , where “m” is the number of photons that need to be absorbed “simultaneously” to achieve ionization.

### 2.4.3 Secondary Ionization Pathways

The first two terms represent the primary paths through which electrons can be generated in a gas. In reality, there are a series of secondary processes that can lead to ionization that are not accounted for in Eq. (2.20) because their probability is very low in laser induced breakdown. One such mechanism is the ionization by excited atoms in the gas and can be described by the following reaction:



Under this reaction an excited atom,  $M^*$ , with sufficient kinetic energy could, in principle, ionize another particle through collisions. The main issue with this process is that the kinetic energy required by the excited atom to induce ionization needs to be extremely large ( $\sim 10\text{-}100\text{ keV}$ ) according to Raizer<sup>37</sup>. This is equivalent with the atom moving at close to relativistic speeds  $\sim 10^8\text{ cm/s}$ . An improvement is obtained if the excitation energy of one atom is greater than the ionization potential of other atoms present in the gas mixture. This process is also referred in literature as the Penning effect<sup>93</sup> and it can be promoted in practical applications through resonance excitation of an atom followed by collisions with neutrals. An example is the resonance excitation of He ( $2^1\text{ P}$ ) atoms followed by impact with Ar, Xe or N<sub>2</sub>. Still, unless the laser wavelength is tailored to promote resonance-excitation, the ionization through collisions with excited atoms is not very common in laser generated plasma.

Free electrons can also be formed through associative ionization when two atoms (in which one or both can be in an excited state) collide to form a single positive ion. The process is described by the reaction:



This process happens when the atomic binding energy is higher than what is required for ionization of a single atom. The excess energy resulted from the binding reaction can promote ionization of the newly formed molecule. This process can be important in inert gases such as He or Hg but it is very unlikely in most gaseous plasma of interest for laser ignition applications<sup>37</sup>.

#### **2.4.4 Electron Diffusion**

One of the main loss mechanism in laser plasma is electron diffusion from the focal volume where plasma initiation takes place. In contrast with neutral gas mixtures, in a plasma there are

two types of diffusion: free diffusion and ambipolar diffusion and their respective role depend on the plasma density and temperature. The rate of diffusion is given by:

$$v_D = \frac{D}{\Lambda^2} \quad (2.23)$$

Where  $D$  is the diffusion coefficient and  $\Lambda$  represents the characteristic diffusion length. At low electron densities, the dominant diffusion process is free diffusion. From the kinetic theory of gases, the diffusion coefficient in this case is given by:

$$D = \left\langle \frac{v^2}{3\nu_m} \right\rangle \quad (2.24)$$

Note that free diffusion is dependent on the gas pressure through the collision frequency  $\nu_m \sim p$  being much more important for laser breakdown at low pressures. The electron velocity can be estimated as:  $v^2 = 2\bar{\epsilon}/m_e$  where the average electron energy,  $\bar{\epsilon}$ , is usually taken as one third of the ionization potential ( $\bar{\epsilon} = \bar{\epsilon}_I/3$ ). If the plasma density is high, electron diffusion becomes affected by the other charged particles present in the gas. This reduces diffusion because the electrons cannot leave the focal volume without “dragging” the heavier ions after them. This type of diffusion is called ambipolar and leads to a reduction of the diffusion coefficient by the square root of the ratio between the mass of the electron to that of the ion ( $\sqrt{m_e/m_{ion}} \sim 10^{-2}$ )<sup>32</sup>. Ambipolar diffusion becomes the dominant mechanism when the Debye length is smaller than the beam waist:

$$\lambda_D = \left[ \frac{k_b T_e}{4\pi n_e e^2} \right]^{1/2} < w_0 \quad (2.25)$$

One can use Eq. (2.25) to determine the critical plasma density for which ambipolar diffusion is dominant:

$$n_{e\_critical} > k_b T_e \left[ \frac{1}{4\pi w_0^2 e^2} \right]^{1/2} \quad (2.26)$$

The characteristic diffusion length in Eq. (2.23) is dependent on the geometry of the ionization volume<sup>29</sup>:

$$\begin{aligned} (\text{cylinder}): \quad & (1/\Lambda)^2 = (2.4/R)^2 + (\pi/L)^2 \\ (\text{sphere}): \quad & (1/\Lambda)^2 = (\pi/R)^2 \end{aligned} \quad (2.27)$$

Overall, diffusion can be significant when optical breakdown is attempted in low pressure mixtures and beam waist is small (see dependence on beam radius in Eq. (2.27)).

### 2.4.5 Recombination

In the absence of an electric field, electron-ion reactions also play a significant role in plasma decay. For example, dissociative recombination is one of the main electron loss mechanism at low temperatures (such as pre-ionization plasmas) due to the presence of molecular ions. The reaction describing dissociative recombination can be written as follows:



Typically, the collision of an electron with a molecular ion leads to atomic dissociation and subsequent excitation. In air plasma some of the most important reactions involve the dissociation  $N_2^+$ ,  $O_2^+$  and  $NO^+$  ions<sup>94</sup>:

$$\left\{ \begin{array}{ll} N_2^+ + e^- \rightarrow N + N(^2D), & k = 2 \times 10^{-7} \times \left(\frac{300}{T_e}\right)^{0.5} [cm^3/s] \\ O_2^+ + e^- \rightarrow O + O, & k = 2 \times 10^{-7} \times \left(\frac{300}{T_e}\right)^{0.5} [cm^3/s] \\ NO^+ + e^- \rightarrow N + O, & k = 4 \times 10^{-7} \times \left(\frac{300}{T_e}\right)^{1.5} [cm^3/s] \end{array} \right. \quad (2.29)$$

As suggested by Eq.(2.29), the likelihood of dissociative recombination decreases with increasing plasma temperature (note the inverse dependence on  $T_e$ ). Moreover, in high density plasma molecular ions are replenished almost instantaneously through conversion reactions of the type:

$M^+ + M + M \rightarrow M_2^+ + M$ . The rate of conversion can be significantly faster than that of dissociative recombination due to the high abundance of atoms in the early stages of the discharge. Accordingly, conversion reactions can produce larger ion complexes such as  $N_4^+$  and  $O_4^+$  that have even larger rate coefficients than those presented in (2.29)<sup>94</sup>:

$$\begin{cases} N_4^+ + e^- \rightarrow N_2 + N_2, & k = 2 \times 10^{-6} \times \left(\frac{300}{T_e}\right)^{0.5} [cm^3/s] \\ O_4^+ + e^- \rightarrow O_2 + O_2, & k = 1.4 \times 10^{-6} \times \left(\frac{300}{T_e}\right)^{0.5} [cm^3/s] \end{cases} \quad (2.30)$$

Plasma decay, accompanied by light emission, is also possible through the process of radiative recombination. This mechanism of electron loss can be described by the following reaction:



As noted by Raizer<sup>37</sup> this mechanism is not as important as dissociative recombination in accounting for the loss of electrons in a plasma. However, it is of importance in the field of spectroscopy because the light emitted through reactions of the type (2.31) allows for species detection. Typical rate constants for this process are on the order of:  $\nu_{rr} \sim 10^{-12} cm^3/s$ .

In high pressure gas discharges, recombination can also take place through 3-body electron-ion reactions:



Where  $A^+ = N_2^+, O_2^+, NO^+, N^+, O^+$  and  $M = N_2, O_2$ . The presence of the third body in this type of reaction is almost mandatory in order to absorb the excess energy resulted from the collision of highly energetic electrons with ions. Nonetheless, reactions of the type (2.32) have a very low probability<sup>94</sup> (typically:  $\nu_{e-ion} \sim 10^{-19} - 10^{-25} cm^6/s$ ).

## 2.4.6 Attachment

Electron attachment can be the dominant mechanism for electron loss in mixtures containing gases with high electronegativity. Typical example of atoms and molecules with high electron affinity (0.5-3 eV<sup>37</sup>) includes:  $O$ ,  $H$ ,  $O_2$ ,  $H_2O$  and halogen gases (not considered in this work). In air breakdown, the process is characterized mainly by reactions of the type:



with:  $M = O_2, N_2, H_2O$ . When the electron collides with molecular oxygen, the binding energy is distributed over the vibrational modes of the molecule resulting in the formation of a stable negative ion. A typical attachment frequency of electrons in an air mixture at  $p=1$  atm is given by Raizer<sup>37</sup>:  $\nu_a \sim 10^8 \text{ s}^{-1}$ . Electron attachment has been shown to play a significant role in allowing plasma revival at very long delays after the decay of electron densities. For example, if a secondary pulse is added to the previously ionized gas, the weakly bonded electrons can be detached from the negative ions and multiplied through a cascade process leading to the revival of a plasma kernel at hundreds of microseconds after its initial decay with only moderate laser irradiance required (below that required to achieve breakdown in the first place)<sup>44</sup>.

Ion-ion recombination (or charge transfer) reactions can play an important role in plasmas in which attachment is significant due to the high concentration of negative ions:



The binary reaction described in (2.34) is only reasonable at low pressures. At high pressures ( $p > 1$  bar) the ions lose energy through frequent collisions with molecules and cannot undergo neutralization anymore with opposite charge ions<sup>37</sup>.

## CHAPTER 3:

### Threshold Characteristics of Ultraviolet and Near-Infrared

### Nanosecond Laser Induced Plasmas<sup>1</sup>

This chapter is concerned with the energy absorption, optical emission, temperature and fluid dynamics of ultraviolet (UV)  $\lambda=266$  nm and near infrared (NIR)  $\lambda=1064$  nm nanosecond laser induced plasmas in ambient air. For UV pulses at the conditions studied, energy absorption by the plasmas increases relatively gradually with laser pulse energy. Additionally, measurements of plasma luminosity show that the absorption of UV radiation does not necessarily result in visible plasma emission. For the NIR induced plasmas, the energy absorption profile is far more abrupt and begins at much higher laser energies. In contrast with UV, the absorption of NIR radiation is always accompanied by intense optical emission. This indicates that the mechanism governing the plasma formation at UV and NIR wavelengths is different. The temperatures of both types of plasma have been measured with Rayleigh scattering thermometry (at times after the Thomson signal sufficiently diminishes). The UV plasmas can attain a wider range of temperatures, including lower temperature compared to the NIR plasma. The temperature of NIR plasma is found to be consistent with what was previously reported in literature and. The high temperature of the NIR plasma correlates well with those of gas optical breakdown. Differences in the fluid dynamics

---

<sup>1</sup> This chapter is based primarily on material published as a journal article: Dumitrache, C., Limbach, C. M., Yalin, A. P., “Threshold Characteristics of Ultraviolet and Near Infrared Nanosecond Induced Plasmas”, *Physics of Plasma* 23, 093515(2016). My contribution to this was to perform the experiments and write the manuscript. Section 3.2.12 is based on two AIAA conference proceedings papers: (1) Dumitrache, C., Wilvert, N, Yalin, A.,P. “Laser Plasma Formation Using Dual Pulse Pre-Ionization”, AIAA2013-2632. (2) Dumitrache, C., Limbach, C. M., Yalin, A. P., “Laser Thermal Ignition Using a Dual-Pulse Approach”. I collected all data presented here from the two AIAA papers and I wrote both manuscripts.

for UV versus NIR pulses are also investigated in this chapter using Schlieren imaging. The contrast in the UV and NIR plasma threshold behavior are attributed to differing roles of avalanche ionization and multiphoton ionization as is also illustrated by a simple numerical model. Finally, the two pulses are overlapped in an attempt to quantify the ability of the dual-pulse to tailor the plasma parameters. It is demonstrated that temperatures relevant for ignition applications can be obtained using the combination of the UV and NIR pulses.

### **3.1 Description of Experimental Procedure**

#### **3.1.1 Optical Layout**

The optical layout used for the laser plasma generation and measurements of energy absorption, optical emission, and Rayleigh thermometry is presented in Figure 3.1. The UV laser plasma is generated by the fourth harmonic of an unseeded Nd:YAG laser (Continuum Powerlite 8010) at 266 nm. The delivered laser energy is adjusted with a variable attenuator comprised of a half waveplate and polarizer. Shot-to-shot variations in delivered energy are monitored by collecting a small fraction (~3%) of the laser light (picked off by a beam splitter) with an energy meter (Ophir PE-10). Optical breakdown is produced by focusing the beam with a single plano-convex lens of focal length 300 mm. NIR pulses are produced from the unseeded fundamental output (1064 nm) of a second Nd:YAG laser (New Wave Gemini PIV). Again, a variable attenuator (half-waveplate and polarizer) and energy meter are used to vary and monitor the output pulse energy before it reaches the plasma formation area. The NIR beam is also focused with a plano-convex lens of focal length 300 mm. Laser plasma formation occurs inside an aluminium chamber (with a volume of 195 cm<sup>2</sup>) that can be filled with different gases and to different pressures (measured with pressure gauge Omega DGP 409-500A). The two beams are combined with a beam splitter such that they share a common optical axis through the chamber (though the

current experiments only use one beam at a time). The waist sizes are made consistent (within  $\sim 10 \mu\text{m}$ ) by appropriately setting the focusing lenses. Sizes and durations of the beams have been characterized and are also given in Table 3.1.

Transmitted beam energies after the laser plasma formation and chamber are measured with a photodiode (MODEL Thorlabs DET 10A). The photodiode signals (whose temporally integrated areas are used) have been calibrated to energy measurements with an energy meter. As discussed below, the combination of the delivered energy measurement and the post-plasma measurement allow determination of energy absorbed by the plasma.

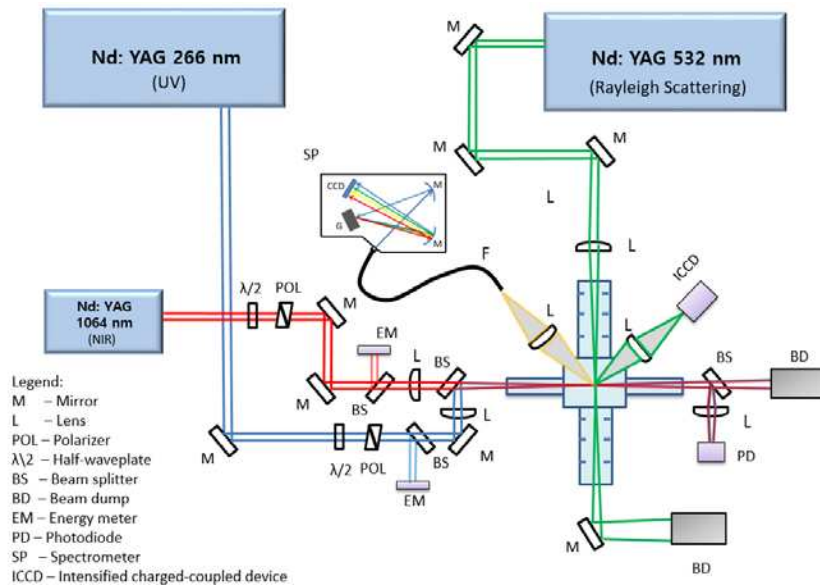


Figure 3.1: Optical layout for the laser plasma formation experiment using UV and NIR pulses. The Rayleigh scattering setup used for measuring gas temperature is also shown.

Table 3.1: Parameters for the three Nd: YAG lasers used in the Rayleigh scattering experiment

Laser	Wavelength (nm)	Pulse Duration (ns)	Waist Diameter ( $\mu\text{m}$ )	Energy (mJ)
UV	266	7	150	0 – 60
NIR	1064	10	150	0 – 75
Rayleigh Scattering	532	10	170	10
Schlieren	1064	15	N/A	< 1

### 3.1.2 Energy Absorption

Single-shot measurements of the energy absorption by the plasma are obtained from the energy meter and calibrated photodiode at the chamber output. The fraction of absorbed energy  $F$  is calculated as:

$$F = C \frac{E_i - E_t}{E_i} \quad (3.1)$$

where  $E_i$  and  $E_t$  are the incident and transmitted pulse energies. A correction factor  $C$  that accounts for optical losses through the chamber and a calibration factor between the two instruments was obtained by evacuating the chamber ( $p < 10$  mbar) and measuring the input and output laser energy. The energy absorption measurement approach requires that any scattering of incident laser light by the plasma itself be negligible, as is also widely assumed by other researchers<sup>22,26,59</sup>.

### 3.1.3 Plasma Emission

Spatially resolved optical emission from the laser induced plasmas is collected using an ICCD camera (pco DICAM pro) with pixels binned 2 x 2. The gating and exposure is set such that each image shows the plasma luminosity during the first 100 ns immediately after the laser pulse. The photons were collected perpendicular to the plasma and imaged onto the detector array using an  $f/3.0$  plano-convex lens. Prior to reaching the ICCD the light is passed through a 532 nm bandpass filter (full-width at half-maximum of 10 nm) placed in front of the ICCD camera. The peak plasma luminosity, i.e. the signal from the most luminous part of the plasma, was determined by querying the images for the location with the maximum binned pixel intensity.

### 3.1.4 Rayleigh Scattering

The Rayleigh scattering probe beam is the second harmonic (532 nm) of an additional Nd:YAG laser (Spectra Physics PR-II) with pulse duration 10 ns. In order to obtain maximum

scattering intensity, the polarization of the 532 nm beam was set orthogonal to the viewing direction (S-polarization). The Rayleigh beam is focused using a  $f=250$  mm plano-convex lens to a waist diameter of  $\sim 170$   $\mu\text{m}$  and directed into the chamber such that it passes through the center of the plasma kernel and is orthogonal to the plasma formation beams. Since the core region of the plasma kernel moves slightly with changes in chamber pressure, the Rayleigh beam is re-aligned for each test to ensure overlap in each case. Scattered photons are collected using an  $f/3.0$  lens and imaged on an ICCD camera (pco DICAM pro) with an array size of  $1280 \times 1024$  pixels ( $6.7$   $\mu\text{m}$  per pixel). The camera exposure is set to  $50$  ns and the gain is held constant for all the measurements. Due to potential interference to Rayleigh signals from stray light, several baffles are installed across the length of the chamber. In order to increase signal-to-noise, the scattering signals are averaged over a set of  $300$  images and pixels are binned  $2 \times 2$ . Uncertainties in Rayleigh signal and resulting temperature measurements are discussed below.

Rayleigh scattering is a linear, elastic process that produces a signal proportional to gas density<sup>95,96</sup>. The spatially resolved thermometry approach is based on inferring temperature from density (through the ideal gas law); essentially, an image of the unknown temperature field from the laser plasma is divided by a known reference image. Temporally resolved measurements are obtained by changing the image delay relative to the laser pulse. The approach requires background subtraction, uniform pressure and composition, and negligible Thomson scattering, as will be discussed. The following procedure is used: First, an image of the background stray light (a result of the Rayleigh beam passing through the cell) is acquired with the chamber evacuated ( $p < 10$  mbar). Next, a reference Rayleigh image is obtained at known scattering conditions (ambient air at  $p_0 = 1$  bar and  $T_0 = 300$  K). An image of the plasma optical emission (also a form of background) is also obtained without the Rayleigh beam present. Camera dark counts (with no plasma or

Rayleigh beam) are separately determined. Finally, the following relation is used to obtain the plasma temperature at each pixel in the images:

$$T = T_0 \frac{I_0 - I_B - I_p + I_D}{I - I_B} \quad (3.2)$$

where  $T$  represents the plasma temperature,  $I$  is the Rayleigh signal with plasma,  $I_0$  is the intensity at reference conditions (no plasma), and  $I_B$ ,  $I_p$  and  $I_D$  correspond to background counts, plasma luminosity counts, and dark counts respectively. The terms  $-I_p + I_D$  in the numerator of Eq. (3.2) were only used when plasma emission was present. Note that the approach also automatically normalizes for variations in laser spatial intensity along the beam.

The applicability of Rayleigh thermometry is fundamentally limited by molecular dissociation and ionization in the plasma which alters the mean scattering cross-section of the mixture<sup>97</sup>. Of particular importance is Thomson scattering, or scattering by free electrons, which possesses a differential scattering cross-section 130 times greater than the (effective) Rayleigh cross-section of air at 532 nm<sup>98</sup>, i.e.  $\sigma_T/\sigma_R = 130$ . Because it is also elastic, i.e. centered at the Rayleigh laser wavelength, it is also collected with the Rayleigh signal. Data from two-wavelength interferometry<sup>99</sup> and two-color laser scattering<sup>100</sup> have shown that the light scattering at the center of 1064 nm laser plasmas is dominated by Thomson scattering until 5-10  $\mu$ s after the pulse, prohibiting an accurate Rayleigh temperature measurement. Therefore, Eq. (3.2) given above can only be used to determine temperature after a certain experimentally determined time delay which depends on plasma density and plasma recombination rates.

### 3.1.5 Schlieren Imaging

The basic operation principles of a Schlieren photography system have been described in detail in the section 3.1 and here only the optical layout used for the plasma visualization

experiments is discussed. As shown in Figure 3.2, Schlieren illumination is provided by a Nd:YAG laser (New Wave Gemini PIV) operating at 1064 nm with a pulse duration of 15 ns. The Schlieren system is of the z-type and uses two dielectric mirrors (diameter 2.54 cm) to steer the Schlieren beam perpendicular to the plasma kernel. At the cutoff plane, a partially transmitting neutral density knife edge is used to mitigate some of the issues inherent to laser illuminated Schlieren<sup>101</sup>. Images are captured with a triggered CCD camera (Spiricon SP503) with an array size of 640×480 pixels (10 μm pixel size). The camera is gated with respect to the Schlieren laser using a pulse delay generator (BNC 555) and the image exposure time is dictated by the laser pulse length (15 ns). This technique enables one to generate short exposure images using relatively inexpensive imaging camera. The image collection speed of the camera is also limited to 10 fps which is unacceptable for the time scales involved in the formation of laser plasma (~ 1 μs). Nonetheless, the shot-to-shot reproducibility of the optical breakdown process, allows one to phase-lock the Schlieren laser to the UV and NIR lasers respectively using the pulse delay generator. This means that a single Schlieren image was collected for each plasma formation event with the Schlieren laser being successively delayed with respect to the UV and NIR lasers to collect the remainder of the sequence images. Finally, the frames from different events were “stitched” together to generate the sequence shown in Figure 3.9. To confirm the shot-to-shot reproducibility of the plasma formation event, at each time delay a series of 100 Schlieren images were collected.

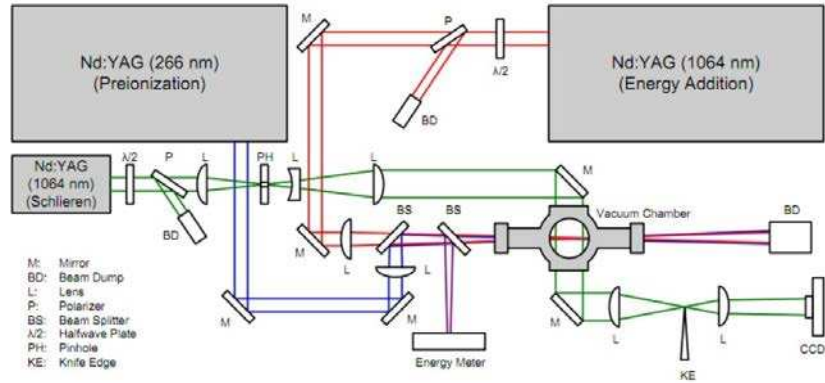


Figure 3.2: Optical layout demonstrating the use of a Z-type laser illuminated Schlieren imaging system (beam is shown in green) for visualization of UV and NIR laser generated plasma. The UV beam is shown in blue and the NIR beam in red<sup>102</sup>.

## 3.2 Results & Discussions

### 3.2.6 Energy Absorption Study

Measurements of laser energy absorption were obtained for both UV and NIR pulses in air at initial temperature of  $T_0 = 295$  K using the setup presented in section 4.1.1. The results of the energy absorption study are presented in the scatter plots of Figure 3.3 for various pressures and laser input energies. Each plotted point corresponds to an individual laser shot. Two observations are immediately apparent: 1) at a given pressure, energy absorption for the UV begins at lower pulse energy than for IR, i.e. at  $\sim 12$  mJ for UV at 1 bar versus at  $>55$  mJ for NIR at the same pressure. Although the pulse intensity of the NIR pulse is slightly lower than that of the UV pulse due to the slightly longer pulse (see Table 3.1) this difference is not sufficient to explain the large energy difference observed in Figure 3.3. 2) for a given pressure and pulse energy the UV absorption can vary fairly continuously in a unimodal distribution (e.g. between  $\sim 0$ -10% at 1 bar and  $\sim 15$  mJ, and between  $\sim 8$ -25% at 1 bar and  $\sim 25$  mJ), while the NIR absorption “jumps” between zero and an elevated range (e.g. between 0% and a range from  $\sim 5$ -30% at 1 bar and 65 mJ), i.e. the NIR shows a bimodal distribution with one group of points at zero and a second group in a range

at elevated absorptions. The final observation of the NIR jumping between zero and then elevated values (with absence of points in between) corresponds to the “threshold” behavior (plasma on or off) widely reported – the lack of such behavior for UV casts immediate doubt on the suitability of characterizing UV plasma formation with threshold breakdown intensities and is indicative of different physics. (Note that for the NIR data of Figure 3.3, all measurements for the pressures above 1 atm are above the breakdown threshold, and all measurements at 0.5 bar are below, i.e., measuring the lower pressures at higher energy would eventually lead to a jump to increased absorption, and measuring the higher pressures at lower energy would eventually lead to a bimodal grouping zero absorption).

The observed decrease in laser energy requirement for achieving absorption (through optical breakdown) in the UV versus NIR, is consistent with MPI playing a larger role at higher optical frequencies<sup>29,35,36,103</sup>. The pressure dependence shown in Figure 3.3 provides further support for the increased role of MPI versus EAI for the UV case. For EAI at sufficiently elevated pressures, Chylek et al.<sup>104</sup> suggest a threshold intensity scaling of  $I_{th} \sim 1/p^k$ , where  $k \approx 1$ , while for MPI the pressure scaling is much weaker with  $k \approx 1/\alpha$ , where  $\alpha$  is the number of photons needed for photoionization. In air, the MPI process involves the absorption of 3 and 11 photons for O<sub>2</sub> ( $I_{p,O_2} = 12.07$  eV) for our UV and NIR wavelengths respectively, and similarly 4 and 14 photons for N<sub>2</sub> ( $I_{p,N_2} = 15.58$  eV). The observation of weaker pressure dependence for UV versus NIR, for example looking at UV energy of  $E = 20$  mJ versus NIR laser energy of  $E = 70$  mJ, is thus indicative of increased role of MPI in the former case.

Contributions from resonant enhanced multiphoton ionization (REMPI) may also influence the lower absorption energies observed at 266 nm versus 1064 nm. Lewis and Wadt<sup>105</sup> have found resonances that facilitate the multiphoton process at 266 nm by measuring the fluorescence signal

produced by transitions corresponding to the second positive system of  $N_2$  ( $C^3\Pi_u \rightarrow B^3\Pi_g$ ) and the first negative system of  $N_2^+$  ( $B^2\Sigma_u^+ \rightarrow X^2\Sigma_g^+$ ). The 2+1+1  $N_2$  REMPI process proposed in their study involves a two-photon resonance involving the transition  $a^1\Pi_g \leftarrow X^1\Sigma_g^+$ . Ionization then occurs by absorption of the third photon corresponding to a vibrational transition from  $a^1\Pi_g (v''=4)$  to  $b^1\Sigma_u^+ (v'=13)$  followed by a fourth photon to the ionization continuum. The authors acknowledge that the total energy of the four photons ( $150,348 \text{ cm}^{-1}$ ) is slightly less than that required to excite the  $B^2\Sigma_u^+$  state of  $N_2^+$  ( $151,234 \text{ cm}^{-1}$ )<sup>105</sup>. However, the energy difference ( $886 \text{ cm}^{-1}$ ) can be accounted for when gas heating due to quenching of intermediate states is considered.

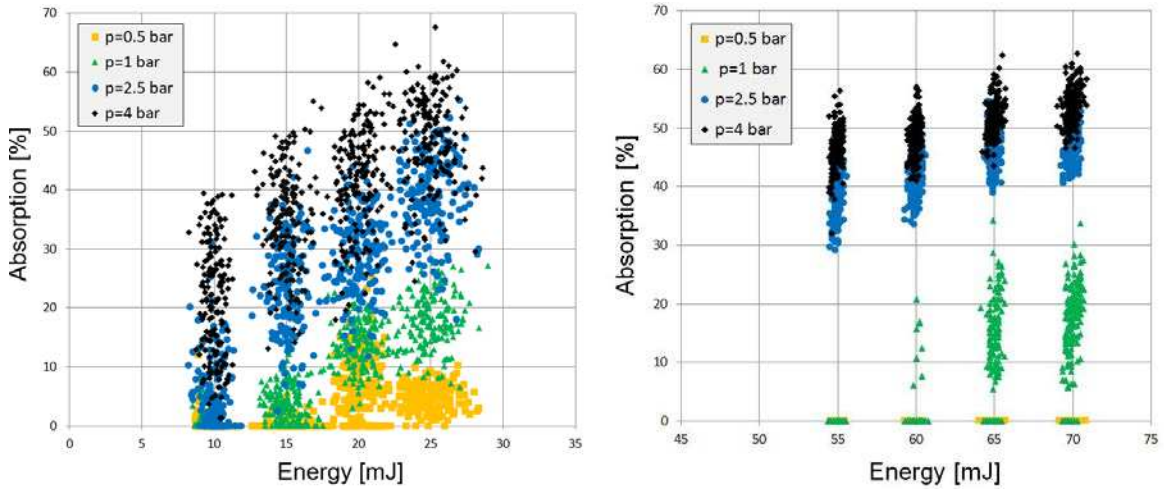


Figure 3.3: Scatter plots of energy absorption for UV (left) and NIR (right) laser induced plasmas as a function of incident laser pulse energy. Data is for air at the indicated initial pressures.

### 3.2.7 Plasma Luminosity & Emission Spectra

The contrasting threshold behavior of the UV and NIR pulses is also manifested in measurements of plasma luminosity, shown in Figure 3.4, for air at starting conditions of 300 K and 1 bar. The left and right panels show the ICCD optical emission signal counts for the UV and NIR pulses, respectively, and each point represents a single laser shot. In each case, the plotted point represents a  $40.2 \times 40.2 \mu\text{m}$  average intensity region around the maximum pixel intensity in

the 2-D image. The inserts in Figure 3.4 show such images. As with the energy absorption data, the UV pulse shows no apparent threshold with plasma luminosity spanning a range of values at a given laser energy, and counts tending to increase with energy. For laser energies, less than ~15mJ, the plasma luminosity is very weak and is only captured by the ICCD (it is not visible by eye). It is important to note that the apparent threshold at 10 mJ in the UV luminosity data is due to detection limit and it does not necessarily imply zero plasma emission for lower energies. In the case of the NIR pulse, the emission intensity again follows a threshold type behavior with no emission observed for less than ~55 mJ, then a range where one “jumps” between either zero or high count levels for individual laser shots (discontinuous bi-modal distribution), followed by a higher energy region at above ~65 mJ where essentially all laser shots have high luminosity. These observations are very consistent with the energy absorption data and again relate to the increased role of MPI (and possibly REMPI) for the UV case and more prominent EAI for the NIR case.

An important aspect of the data presented in Figure 3.3 and Figure 3.4 is the large scatter, i.e. stochastic nature, of the breakdown process. This is most evident for the UV cases but also occurs for the NIR (both between breakdown and non-breakdown, and within the breakdown case). The stochastic nature of optical breakdown has been reported in the past<sup>25,59,106</sup> and while measures can be undertaken to limit this behavior, it cannot be completely eliminated<sup>31</sup>. Several factors may contribute to this behavior such as spherical aberrations<sup>107</sup> and changes in spatial and temporal structure of the beam<sup>108,109</sup>. Each factor directly affects the photon flux inside the focal region, thereby exerting a strong influence on the rates of MPI and EAI. The AC Stark effect may broaden and shift virtual electronic states bringing them into resonance and produce variations in the MPI rate. Therefore, shot-to-shot variations of the photon flux can lead to intermittent overlap with atomic resonant states which could randomly increase the ionization rates (through REMPI) and

significantly change the amount of energy absorption inside the plasma<sup>31</sup>. Since the selection rules depend on the magnetic quantum number, changes in light polarization from shot-to-shot may also lead to plasma variability<sup>110</sup>. Our laser system operates polarized unseeded and the beam presents multiple spatial and temporal modes. The randomness of these modes do not dictate the main features of the data though, since, for example, regardless of the modes, the differing UV and NIR threshold characteristics are present in Figure 3.3 and Figure 3.4.

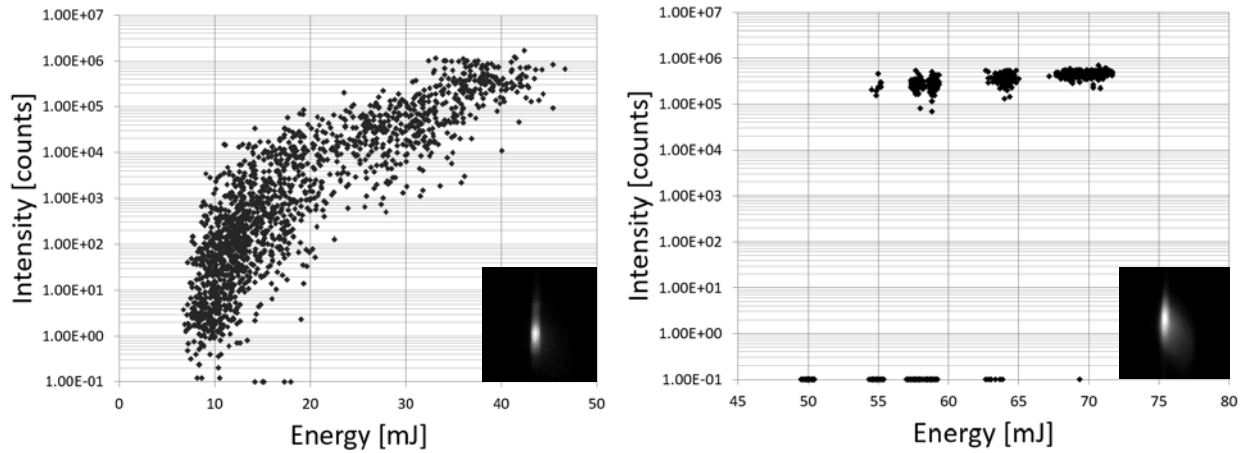


Figure 3.4: Luminosity of laser induced plasmas at various laser energies for UV (left) and NIR (right) beams.

To complement the plasma luminosity study, times integrated optical emission spectra, presented in Figure 3.5 below, were collected for both UV and NIR plasmas. For the UV case, the spectrum was captured at low energy ( $E_{266\text{nm}}=15$  mJ), when the plasma luminosity is somewhat visible by naked eye whereas for the NIR pulse the spectra was collected for an intense spark condition. No attempt was made to correct for the spectral sensitivity of the spectrometer, detector, or the focusing lens and fiber in the optical path. Strong emission lines were identified using the National Institute of Standards and Technology (NIST) database<sup>111</sup> and predominantly correspond to atomic species and ions. For both pulses, the major lines were  $\text{N II}$  (463.054 nm),  $\text{N II}$  (500.11 nm) and  $\text{N II}$  (518.04 nm). Other lines that have been observed are emission from atomic nitrogen

and oxygen:  $N_I$  (746.83 nm) and  $O_I$  (777.42 nm). Several previous studies<sup>112</sup> have also identified some faint molecular lines such as:  $N_2$  ( $B^3\Pi_g \rightarrow A^3\Sigma_u^+$  or  $C^3\Pi_u \rightarrow B^3\Pi_g$ ),  $O_2$  ( $B^3\Sigma_u^- \rightarrow X^3\Sigma_g^-$ ) or electronically excited molecular ions like  $N_2^+$  ( $B^2\Sigma_u^+ \rightarrow X^2\Sigma_g^+$ ). However, in the current study these lines were not observed.

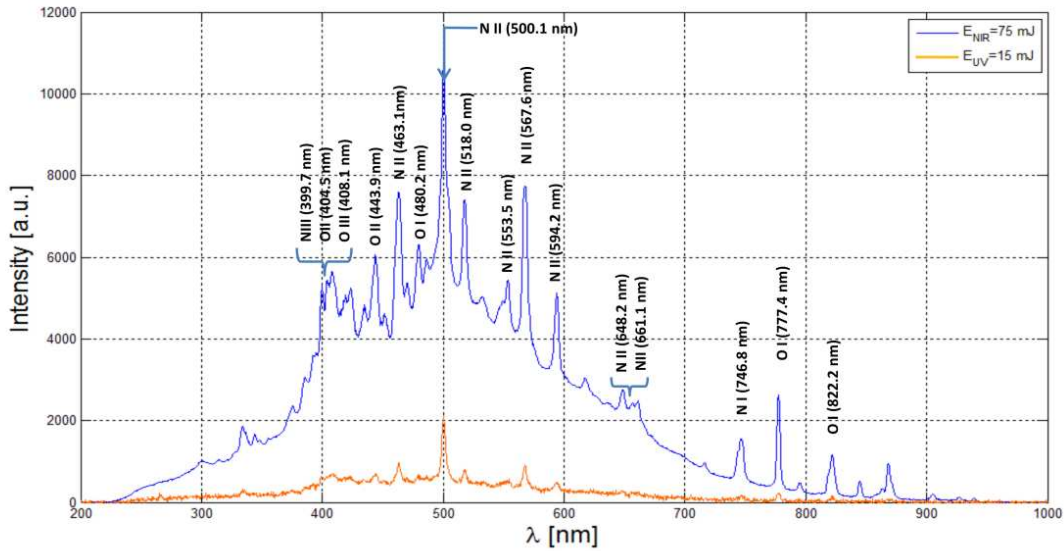


Figure 3.5: Optical emission spectrum from a NIR laser-induced spark (blue) and a UV plasma (orange).

### 3.2.8 Rayleigh Scattering Thermometry

The temperature of the decaying plasma kernels was measured using Rayleigh scattering in order to determine the gas heating associated with the breakdown event. The study was conducted at a pressure  $p_0=1$  bar and an initial temperature of  $T_0=300$  K. The gas temperature was measured for laser energies from 7-35 mJ at 266 nm, and at 75 mJ for 1064 nm, with time delays ranging from 1-150  $\mu$ s after the laser pulse. The results shown in Figure 3.6 report the maximum gas temperature along the Rayleigh probe beam. (The location of the maximum temperature is identified at the onset of the laser plasma, and the same location is used to report temperature at later time.). For the UV plasma, we again observe a continuous change in plasma properties as the

laser energy varies, though it should be noted that each temperature point is based on the average of 300 shots so that the stochastic variation for a given energy is not captured here. The measurements span a wide range of input energies from  $E=7$  mJ ( $T\sim 500\pm 5$  K at  $1\ \mu\text{s}$  delay) to  $E = 35$  mJ ( $T\sim 3500\pm 140$  K at  $1\ \mu\text{s}$  delay) and one sees that the temperature increases continuously throughout. In the case of the NIR pulses, the optical breakdown results in either a high density and high temperature plasma or no plasma at all. Temperatures in excess of 10,000 K were measured starting at  $10\ \mu\text{s}$  after the end of the pulse. Several other researchers have performed similar measurements for laser induced sparks at 1064 nm and report maximum temperature histories consistent with our findings<sup>113,114</sup>. For example, Glumac and Elliot<sup>113</sup>, have reported the temperature for 1064 nm sparks using filtered Rayleigh scattering, finding temperatures of  $\sim 2000$  K at delays of  $50\ \mu\text{s}$ . The profiles of Figure 3.6 show that the NIR laser plasma cools more quickly in an absolute sense, though the time constants (or fractional rates) are relatively comparable. It should also be noted that, particularly for the NIR case, the location of maximum temperature may in fact not remain fixed in the measurement region due to advective effects of the plasma toroid as can also be seen from the Schlieren study.

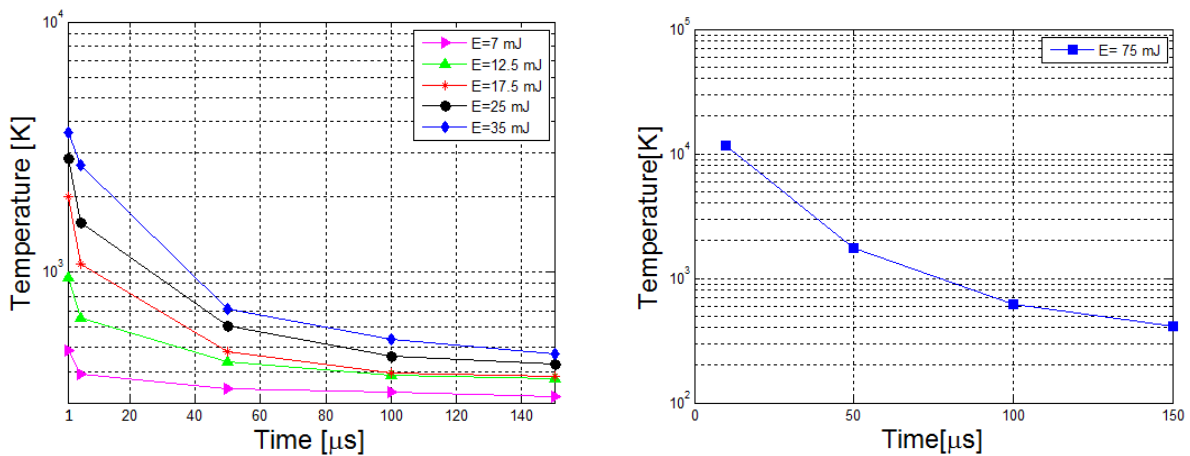


Figure 3.6: Gas temperature measurement using Rayleigh scattering after the UV pulse (left) and the NIR pulse (right). Measurements were made in air at  $p_0=1$  bar,  $T_0=300$  K.

### 3.2.9 Plasma Density Measurements

For the UV plasmas, the earliest time at which the temperature could be measured was 1  $\mu\text{s}$  after the end of the pulse while for the NIR plasmas the earliest time was 10  $\mu\text{s}$ . Prior to these time delays, the plasmas are dense enough that Thomson scattering is significant and interferes with the Rayleigh scattering signal. (The competing Thomson signal would cause artificial lowering of the measured peak temperature if the regular method were applied.) The longer wait period for NIR relative to UV is due to higher electron density in the former case; therefore, it is important to understand the time applicability of the assumption that all scattered light is due to Rayleigh scattering. Figure 3.7 shows normalized Rayleigh signal intensities through the center of the plasma forming laser beam for the UV plasma for  $E = 25$  mJ (left) and NIR plasma for  $E = 20$  mJ (right) with curves for different time delays (1064 nm data used a 100 mm focal length lens). By normalized intensity we mean the ratio of the plasma scatter signal to that from the reference image, after background subtraction, so that, for example, a ratio of 1 would indicate that plasma temperature equals reference temperature in the absence of complicating effects. For both UV and IR, one can notice that at early times the signal increases towards to center of the kernel which is attributed to Thomson scattering from high electron number density present immediately after the end of the pulse. The apparent Thomson signal diminishes and disappears over a time scale consistent with plasma recombination times. Also apparent in Figure 3.7 is the characteristic blast wave that accompanies the laser plasma formation<sup>25</sup> which leads to a signal increase at the plasma edges due to density rise across the shock wave. The shock wave travels outward and dissipated energy as time progresses. A closer inspection of the results shows that for the UV pulse the plasma kernel is smaller than that generated by the NIR pulse, and that its Thomson signal decays much

faster. These findings are consistent with the plasma generated by the UV pulse being less dense compared to that from the NIR pulse (at the conditions studied).

Assuming that Thomson scattering is responsible for the signal increase at the center of the plasma kernel allows estimation of the plasma electron number density. As shown in Figure 3.7 one can bound the electron density by assuming that the entire signal at this pixel location is due to Thomson scattering (upper bound) or by assuming that the Thomson scattering contribution is the difference between the minimum signal and the central peak (lower bound). Using such an approach yields an electron number density for the UV case (25 mJ) at 200 ns after the pulse in the range of  $n_e = 2.5\text{--}6.1 \times 10^{16} \text{ cm}^{-3}$  which is several orders of magnitude smaller than the electron number density for a nanosecond NIR plasma of  $n_e = 1.2\text{--}1.7 \times 10^{18} \text{ cm}^{-3}$  measured at 500 ns after the pulse. The density range obtained for the NIR pulse (Figure 3.7-right) is in good agreement with reports from several other studies<sup>113,114</sup>.

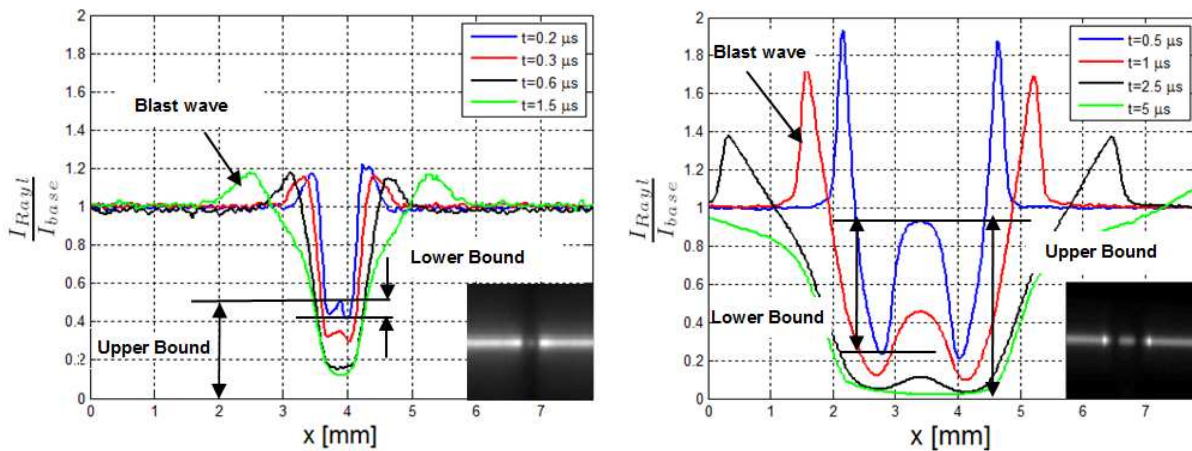


Figure 3.7: Normalized Rayleigh signal through the center of the beam for an UV (left) and a NIR induced plasma. Inserts are the raw ICCD plasma images at time delay 200  $\mu s$  for UV and 500  $\mu s$  for NIR. For both pulses, at early times, an increase in signal intensity is observed at the center of the plasma due to Thomson scattering.

### 3.2.10 Plasma Growth Model

In support of the ideas presented in the experimental study above, a relatively simple zero-dimensional plasma model has been developed. The rate of electron density growth is governed by the continuity equation:

$$\frac{dn_e}{dt} = \nu_{MPI}n + \nu_{EAI}n_e - \nu_D n_e - \nu_{rec}n_e - \nu_{att}n_e \quad (3.3)$$

where  $\nu_{MPI}$  is the multiphoton ionization rate,  $\nu_{EAI}$  is the electron avalanche ionization rate,  $\nu_D$  is the diffusion rate,  $\nu_{rec}$  is the dissociative recombination rate, and  $\nu_{att}$  represents the electron attachment rate. The first two terms on the right side of Eq. (3.3) are responsible for the electron generation by MPI and electron multiplication by EAI while the last three terms provide electron loss mechanisms. The multi-photon ionization rate expression from Morgan<sup>31</sup> is used :

$$\nu_{MPI} = \left( \frac{\sigma}{\hbar\omega^2} \right)^\alpha \frac{2\pi\omega}{(m-1)!} I^\alpha \quad (3.4)$$

where,  $\alpha$  is the number of photons required to overcome the ionization potential of the gas molecules,  $\hbar\omega$  is the photon energy, and  $I$  represents the laser intensity. The photon absorption cross section,  $\sigma$ , is taken to be the same for all the virtual states ( $\sigma = 10^{-16} \text{ cm}^2$ )<sup>32</sup>. Given the expected role of 2+1+1 REMPI in  $N_2$  for UV excitation, the exponent  $m$  has been reduced from 4 to 2 in accordance with the two-photon process limiting the overall REMPI ionization rate. An equation for the cascade ionization rate is given by assuming that the rate of ionization is determined by the ratio of the Joule power to the gas ionization potential<sup>115</sup>

$$\nu_{EAI} = \xi \frac{e^2 \nu_m I}{\epsilon_0 m c [\omega^2 + \nu_m^2]} \left( \frac{0.2}{I_{O_2}} + \frac{0.8}{I_{N_2}} \right) \quad (3.5)$$

where  $\xi$  is a proportionality factor depending on the assumed energy absorbed into the gas (generally taken as  $\xi=0.75$ ),  $m$  is the mass of the electron,  $c$  is the speed of light and  $I_{O_2}$  and  $I_{N_2}$

respectively represent the ionization energy for the oxygen and the nitrogen molecules ( $I_{O_2}=12.2$  eV,  $I_{N_2}=15.6$  eV). The momentum transfer collision frequency of electron with neutral,  $\nu_m$ , is estimated according to Radzimeski and Cremers<sup>32</sup> as  $\nu_m = 2 \times 10^{12}$  p[atm]. The diffusion rate is defined as:

$$\nu_D = \frac{D}{\Lambda^2} \quad (3.6)$$

where  $D$  is the diffusion coefficient accounting for both free electron and ambipolar diffusion and taken as  $D=1200$  cm<sup>2</sup>/sec from Radzimeski and Cremers and  $\Lambda$  is the diffusion length found from Raizer<sup>37</sup> by assuming a cylindrical volume around the focus with a height equal to twice the Rayleigh range. When it comes to dissociative recombination and electron attachment it is important to acknowledge that there are many reactions that contribute to the loss of electrons. However, for simplicity, the dissociative recombination was reduced to the two major reactions involving the losses of electrons with  $N_2^+$  ( $N_2^+ + e \rightarrow N + N$ ) and  $O_2^+$  ( $O_2^+ + e \rightarrow O + O$ ). The rates, taken from Kossyi et al.<sup>94</sup>, depend on electron temperature and for this simulation an average  $T_e=2$  eV was considered. The attachment process can be estimated by assuming that electron attachment only takes place with oxygen (due to its higher electron affinity compared to nitrogen). Raizer<sup>37</sup> gives an estimated attachment rate for the reactions:  $e + O_2 + M \rightarrow O_2^- + M$  (where  $M = O_2, N_2, H_2O$ ) of  $\nu_{att} = 0.9 \times 10^8$  sec<sup>-1</sup>.

Integrating Eq. (3.3) allows one to compute temporal profiles of electron density and plasma growth for UV and NIR pulses and to provide comparison with our experimental studies. The peak electron number density for both UV (266 nm) and NIR (1064 nm) pulses are plotted in Figure 3.8 as a function of the laser energy normalized by the breakdown threshold energy (defined here in terms of the degree of gas ionization:  $\delta = \frac{n_e}{n} = 0.001$ ). The calculations assume laser

pulses with Gaussian temporal profiles of full-width-at-half-maximum of 10 ns and initial pressure of  $p_0=1$  bar. The results support the experimental findings presented above, in particular the NIR pulse clearly shows a threshold behavior versus energy, i.e. a near step-function change from non-breakdown to breakdown, while the UV pulse shows a more continuous increase of electron density with energy. This is consistent with the energy absorption and plasma luminosity findings presented in this work. Given the simplicity of the model, the numeric agreement between the laser energies causing plasma formation is reasonable, i.e. the model predicts NIR threshold of  $\sim 157$  mJ while experiment yielded  $\sim 60$  mJ and the model predicts UV threshold (for  $n_e/n=0.001$ ) of 29 mJ compared to 20 mJ in experiments. Equation (3.3) can also be used to determine the fractional contribution of MPI to the overall number of electrons. Such an analysis indicates that for the UV pulse, most of the electrons ( $\sim 90\%$ ) have been generated through MPI while in NIR, EAI (based on seed MPI electrons) is responsible for  $> 99\%$  of the total electrons.

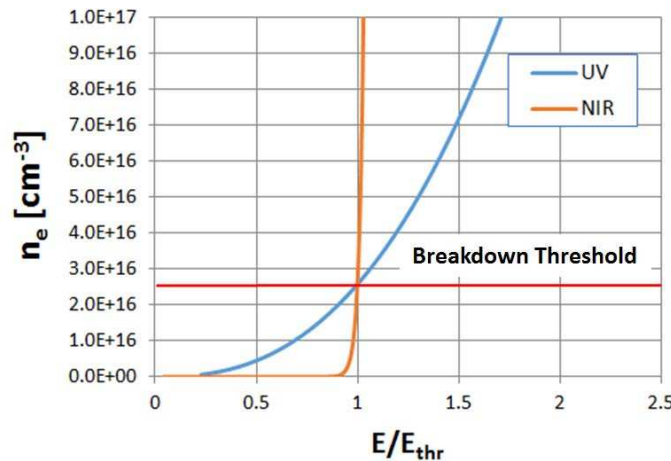


Figure 3.8: Evolution of the electron number density in a plasma generated using UV and NIR pulses. The simulation was conducted at  $p_0 = 1$  bar assuming a Gaussian pulse with 10 ns full-width at half-maximum.

### 3.2.11 Schlieren Imaging of Laser Plasma

Schlieren photography enables the visualization of the temporal and spatial evolution of the plasma kernel for both UV and NIR pulses. Comparison of a NIR pulse ( $E=80$  mJ) and UV

pulse ( $E=20$  mJ) is shown in Figure 3.9. The NIR plasma (top) develops as a localized elliptical kernel and a blast wave is seen propagating away from the kernel after  $\sim 1 \mu\text{s}$ . After the plasma recombines and the gas cools, the typical three lobe structure is formed<sup>26</sup>. The generated toroidal vortex sheds the cold surrounding air and the temperature recovers to ambient conditions within  $\sim 1$  ms. In contrast, the UV induced plasma (bottom) shows a markedly different behavior. The laser pulse generates a relatively long ( $\sim 1$  cm) plasma channel inside the focal region which cools down in  $\sim 300 \mu\text{s}$ . A weak acoustic wave propagates outward from the channel in the first  $3 \mu\text{s}$  after the end of the pulse. The image sequence shown in Figure 3.9 outlines the differences between the plasma dynamics involved in the plasma generation by the two beams. For the NIR pulse, the MPI process (which varies as  $\sim I^{14}$  for NIR as opposed to  $\sim I^3$  or  $I^4$  for UV) that generates the initial free electrons is only effective over a small region around the focus where the photon flux is high enough to allow ionization. Therefore, the cascade ionization process can only act localized around the focal point giving rise to the elliptical shape. In contrast, the higher energy photons of the UV pulse allow the MPI to develop along a larger distance over the beam path so that the plasma is less localized around the focal point leading to a cylindrical plasma channel.

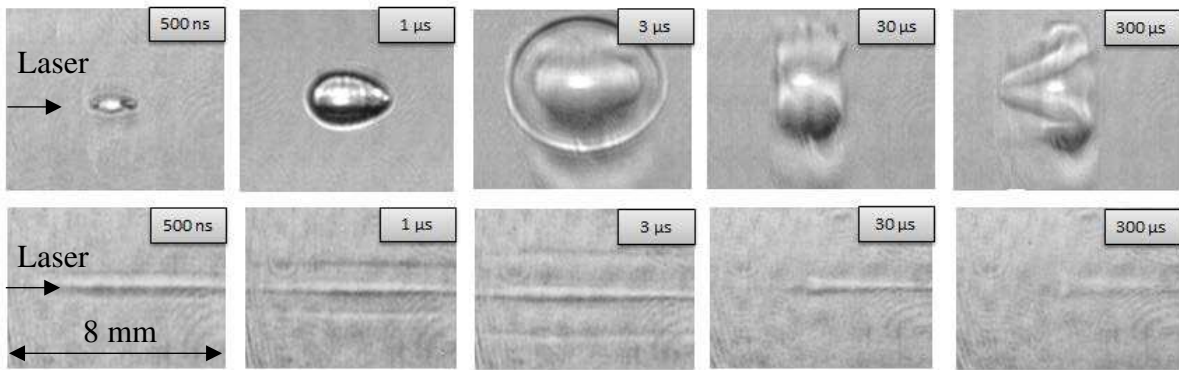


Figure 3.9: Schlieren image sequence showing the evolution of the plasma kernel for NIR pulse (top) and UV pulse (bottom). The laser energies used for these experiments are:  $E_{1064nm}=80$  mJ and  $E_{266nm}=20$  mJ.

### 3.2.12 Overlapped UV and NIR pulses

Gas temperature for the overlapped pulses is measured 50  $\mu$ s after the two pulses. The result is shown on the same plot with the temperature generated by NIR laser sparks. Figure 3.10 shows that combining a 10 mJ UV pulse with a 20 mJ IR pulse yields temperatures as high as  $T=1268$  K. This is equivalent to the temperature obtained by a 65 mJ pulse NIR laser spark. Therefore, a reduction of required energy by more than 3 times is observed. Similar to the temperature analysis for the UV and NIR pulses on their own, data presented in Figure 3.10 was filtered in order to ensure that the temperature results are not biased by events that did not lead to any energy absorption. The UV pulse alone at 10 mJ generates a gas temperature of  $T=430$  K at 50  $\mu$ s after the laser was fired (see Figure 3.6). By adding the 20 mJ NIR pulse the temperature was raised by another  $\sim 800$  K (up to  $T=1268$  K). This result indicates that the overlapping of the two pulses makes it possible to heat the gas to temperatures relevant to ignition using lower energies than NIR sparks. Given the pre-ionization available from the initial UV pulse, the main mechanism through which heat is being added to the mixture is the inverse bremsstrahlung absorption where the free electrons are accelerated by the NIR pulse and transfer energy to the gas through direct e-T and e-V (followed by V-T) transfer<sup>116</sup>. In order to achieve optimum absorption, a good temporal synchronization is required. Based on the pulse lengths shown in Table 3.1 it was experimentally determined that the ideal time delay between the two pulses is around  $\sim 15$  ns (peak to peak). At later times electron re-attachment reactions reduce the availability of free electrons making the inverse bremsstrahlung absorption process less effective. Alternatively, earlier during the pulse, there is not enough buildup of free electrons to generate significant gas heating.

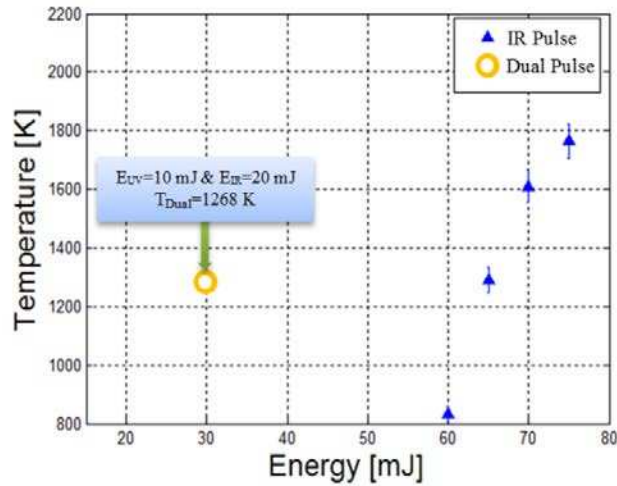


Figure 3.10: Gas Temperature vs. laser energy for the 1064 nm beam and the dual pulse. Temperatures are reported at 50  $\mu$ s after the end of the pulse. Initial conditions are  $p_0=1$  bar and  $T_0=300$  K

Schlieren images of the dual-pulse laser plasma are presented in . The images show that overlapping the two pulses results in a superposition of the effects observed Figure 3.9. More precisely, a plasma channel characteristic of the UV pulse is observed at the early times with a spherical front (coming from the NIR pulse) seen to grow inside the pre-ionized gas. After plasma recombination and at later times ( $t < 30 \mu$ s) the fluid dynamics of the remaining hot gas kernel are similar to those induced by the NIR plasma on its own (see Figure 3.9-top for comparison).

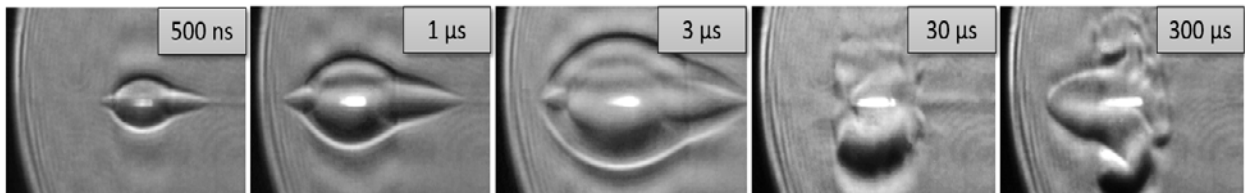


Figure 3.11: Schlieren Images of Dual-Pulse plasma. The laser energies were set to  $E_{266 \text{ nm}}=22$  mJ,  $E_{1064 \text{ nm}}=53$  mJ.

## CHAPTER 4:

### Laser Ignition of Propane-Air Mixture Using Dual-Pulse Pre-Ionization<sup>2</sup>

This chapter presents a comparative study between (conventional) single-pulse laser ignition ( $\lambda=1064$  nm) and a novel dual-pulse method based on combining an ultraviolet (UV) pre-ionization pulse ( $\lambda=266$  nm) with an overlapped near-infrared (NIR) energy addition pulse ( $\lambda=1064$  nm). The early flame kernel development is visualized inside the pressure cell for both ignition techniques using OH\* chemiluminescence. For single-pulse laser ignition at lean conditions, the flame kernel separates through third lobe detachment, corresponding to high strain rates that extinguish the flame. In contrast, the dual-pulse technique is shown to allow control over the plasma-driven fluid dynamics by adjusting the axial offset of the two focal points. In particular, it is demonstrated that there exists a beam waist offset whereby the resulting vorticity suppresses formation of the third lobe, consequently reducing flame stretch. The new technique is shown to be superior to the well-established laser spark ignition method leading to an extension of the lean limit and a decreased ignition energy requirement.

---

<sup>2</sup> This chapter is largely based on the following manuscript: Dumitrache, C., Limbach, C. M., Yalin, A. P., “Control of Early Flame Kernel Growth by Multi-Wavelength Laser Pulses for Enhanced Ignition”. The manuscript was accepted for publication in Nature Scientific Report on August 10<sup>th</sup>. However, at the date of writing this dissertation the manuscript has not yet been published. My contribution to this work was to develop the experimental setup, post-process the results, and write the first draft of the manuscript.

## 4.1 Description of Experimental Procedure

### 4.1.1 Optical Layout

The experiments were conducted using the setup shown in Figure 4.1 For dual-pulse experiments, the UV pre-ionization pulse was the fourth harmonic ( $\lambda=266$  nm) of an Nd:YAG (Continuum Powerlite 8010), while the energy addition pulse was the fundamental output ( $\lambda=1064$  nm) from a second Nd:YAG (New Wave Gemini PIV). Each beam has a variable attenuator, comprised of a half-wave plate and polarizer pair, to control laser energy. The 266 nm beam has 7 ns pulse duration and typical delivered energy of 20 mJ, while the 1064 nm beam has 10 ns pulse duration and typical delivered energy of 40 mJ (exact numbers are given with the experimental results). The two beams are spatially overlapped (with precision  $\sim 10$   $\mu\text{m}$ ) using a beam splitter and focused inside the combustion chamber using two  $f=300$  mm plano-convex lenses (one in each beam path). The focusing configuration yields beam diameters of 170  $\mu\text{m}$  for both beams as measured using the 4- $\sigma$  method<sup>117</sup>. To vary the offset between the two beams in the axial direction (i.e. along the beam propagation direction), a translation stage was used to move the focusing lens of the 1064 nm beam. Both the beam waist axial overlap and waist diameters were determined experimentally using a beam profiler (Spiricon SP503). The combustion chamber has a central volume of  $\sim 0.195$  liters and two side arms of length  $\sim 20$  cm with 2.54 cm diameter circular windows for optical access. A series of photodiodes and energy meters are used to monitor laser pulse durations and pulse energies of each beam leg (i.e. UV and NIR) both before and after passage through the focal region and combustion chamber. For comparative experiment with conventional single-pulse laser ignition, the same 1064 nm laser is used without the accompanying 266 nm beam.

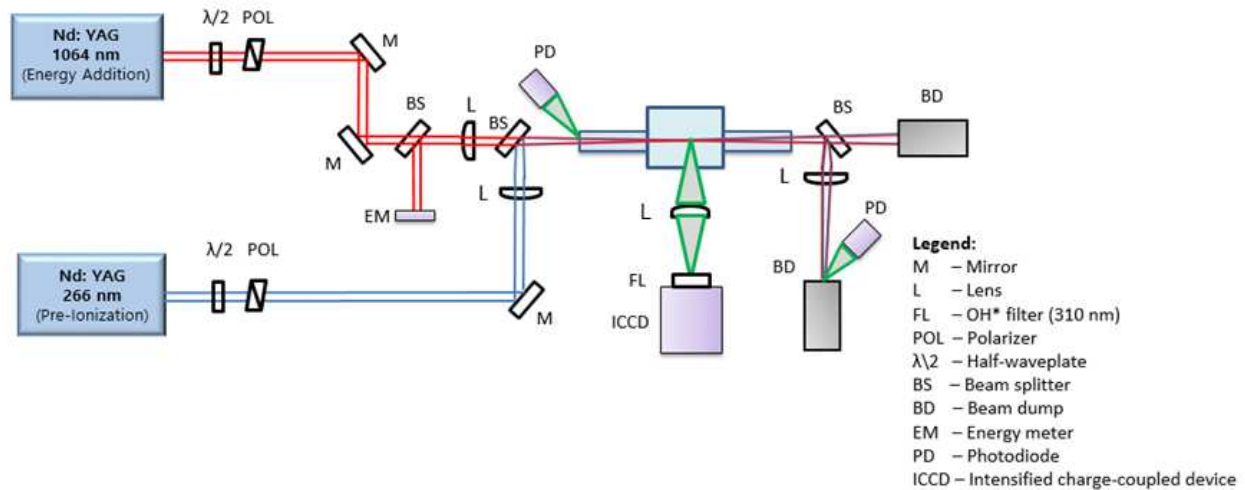


Figure 4.1: Optical layout used for the laser ignition experiments. Single-pulse laser ignition method uses solely the 1064 nm Nd:YAG, while the dual-pulse method uses overlapped beams from both the 266 nm and 1064 nm Nd:YAG lasers.

#### 4.1.2 Data Collection

Pressure data of combustion events was recorded using a pressure transducer (PCB: 113B24) mounted on the inner wall of the chamber. This information is used to determine the lean limit and the combustion efficiency in each test case using the method described in section 4.1.3. Additionally, chemiluminescence images of the OH\* radical were acquired using an intensified charged coupled device (ICCD) camera (PCO dicam pro). The electronically excited hydroxyl radical is generated during the combustion of hydrocarbon fuels through the chain branching reaction:  $\text{CH} + \text{O}_2 = \text{OH}^* + \text{CO}$ . The excited OH\* emits light at  $\sim 310$  nm as it relaxes to the ground state<sup>118</sup>. For CL imaging of this transition a 310 nm bandpass filter (Andover: 310FS10-50, FWHM: 10 nm) was placed in front of the ICCD.

For the combustion experiments presented in this study, the combustible mixture consisted exclusively of propane-air at an initial pressure of 1 bar. Various equivalence ratios ranging from  $\phi=0.6-1.0$  were tested with mixtures prepared inside the chamber based on partial pressures recorded from a gage (Omega DGP409) mounted downstream of the chamber valve. Once the

chamber was filled, there was a 10 minute wait period to allow the fuel and air species to fully mix prior to ignition. Finally, after each experiment, the chamber was flushed with zero air and emptied to a pressure of  $<1$  mbar (by connecting to a vacuum pump) to ensure any effects of residual combustion gases were eliminated. A sketch of the gas mixing manifold is presented below in Figure 4.2.

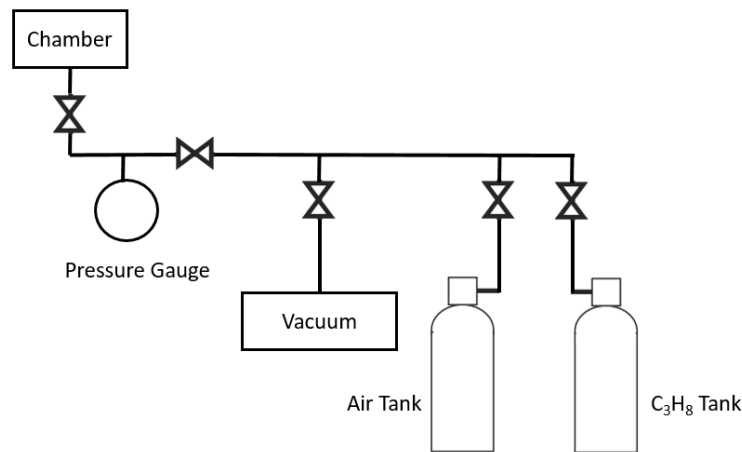


Figure 4.2: Gas manifold used for preparing the propane-air mixtures.

### 4.1.3 Pressure Data Analysis

The pressure inside of the combustion cell changes as a function of time due to chemical reaction heat release, heat transfer to the walls and leakage. This subsection presents a thermodynamic analysis that relates the chamber time history to the combustion efficiency.

In the most general case, let us consider the combustion chamber of an internal combustion engine and write an equation that gives the time rate of change of in-cylinder pressure as measured by a pressure transducer mounted on the cylinder wall (see Figure 4.3). Later, this relation will be simplified for the particular combustion cell used for the dual-pulse laser ignition experiments.

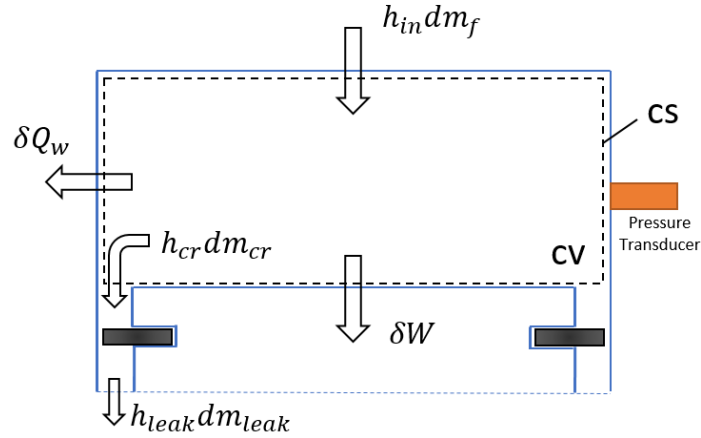


Figure 4.3: Schematic of a general piston-cylinder system used in the control volume analysis to determine the rate of heat release during combustion.

Writing the 1<sup>st</sup> law of thermodynamics for the system showed in Figure 4.3 above, one has:

$$\delta\dot{Q} - \delta\dot{W} = \frac{dE_{sys}}{dt} \quad (4.1)$$

Applying Reynold's transport theorem on the RHS of Eq. (4.1) gives the following expression:

$$\frac{dE_{sys}}{dt} = \iiint_{CV} \frac{\partial \rho e}{\partial t} dV + \oint_{CS} \rho e \vec{V} \cdot d\vec{S} \quad (4.2)$$

Which means that the time rate of change of the energy in a system can be caused by an unsteady change of energy inside the control volume (such as energy released during a chemical reaction) or energy can cross the control surface of the system flowing in or out of the system.

Combining Eq. (4.1) and Eq. (4.2) allows for a more general expression for the 1<sup>st</sup> law of thermodynamics that is valid for any open system:

$$\delta\dot{Q} - \delta\dot{W} = \iiint_{CV} \frac{\partial \rho e}{\partial t} dV + \oint_{CS} \rho e \vec{V} \cdot d\vec{S} \quad (4.3)$$

The integration of the first term in the RHS is straightforward since it simply represents the time rate of change of the system inside the control volume. For the second integral it is important to

note that  $\rho \vec{V} \cdot d\vec{S} = dm$  which is an infinitesimal mass flux. Therefore, taking the integral over the entire control surface bounding the control volume is equivalent to summing up all the fluxes coming in and out of the system.

Based on these arguments, Eq. (4.3) becomes:

$$\delta\dot{Q} - \delta\dot{W} = \frac{dE_{CV}}{dt} + \left\{ \sum_{out} \dot{m}e - \sum_{in} \dot{m}e \right\} \quad (4.4)$$

The first term on the LHS is nothing else than the heat loss to the wall  $\delta\dot{Q} = -\delta\dot{Q}_w$  (where the minus sign indicates that heat is leaving the system). The second term on the LHS represents the summation of two types of work: work done inside of the control volume (CV) and the so-called flow work (which, in this case, leads to an increase in the volume of the CV due to gas expansion):  $\delta W = \delta W_{CV} + pdV$ . Here we neglect the work done inside the CV (there is nothing inside to generate work) such that  $\delta W_{CV} = 0$ . Note that piston is not allowed to cross the domain boundary. Therefore, piston work appears as  $pdV$  (leading to expansion/contraction of the CV) not as  $\delta W_{CV}$ . Including these observations, Eq. (4.3) becomes:

$$-\dot{Q}_w - \frac{d}{dt}(pdV) = \frac{dE_{CV}}{dt} + \left\{ \sum_{out} \dot{m}e - \sum_{in} \dot{m}e \right\} \quad (4.5)$$

The RHS of Eq. (4.5) can be expanded further as well. First, it is important to recognize that there are two contributions to the internal energy of the control volume:  $d\dot{E}_{CV} = -d\dot{Q}_{ch} + d\dot{E}_s$ . The first term represents the heat of formation. In this particular case, since we are primarily looking at combustion, this is given by the internal energy stored in the chemical bonds of the fuel molecule. It is this term that we care about in our derivation because we are trying to find an expression that relates the rate at which the heat released during the combustion event influences the pressure measured by the transducer. The second term represents the sensible energy:

$$dE_s = mc_v dT + e(T)dm \quad (4.6)$$

Note that mass losses to the piston crevices and chamber leaks are accounted for in the second term since:  $dm = dm_{crevice} + dm_{leak}$ . This expression can be developed further with the aid of the equation of state:  $dT = 1/(R_g m)d(p\mathcal{V})$  to obtain:

$$dE_s = \frac{c_v}{R_g}(\mathcal{V}dp + pd\mathcal{V}) + e(T)\{dm_{crevice} + dm_{leak}\} \quad (4.7)$$

Inserting this relation back into the 1<sup>st</sup> law of thermodynamics, Eq. (4.5), we have:

$$\begin{aligned} \dot{Q}_{ch} = \dot{Q}_w + \frac{d}{dt} \left[ \frac{c_v}{R_g} (\mathcal{V}dp + pd\mathcal{V}) + e(T)\{dm_{crevice} + dm_{leak}\} \right] + \\ + \left( \sum_{out} \dot{m}h - \sum_{in} \dot{m}h \right) \end{aligned} \quad (4.8)$$

Where we coupled the  $pd\mathcal{V}$  work with internal energy to express the flux term in terms of enthalpy (since:  $dh = de + d(p\mathcal{V})$ ).

Equation (4.8) is the most general relation that shows how the chemical energy inside of the combustion chamber of an internal combustion chamber can change. For the experiments conducted in this chapter, this relation can be simplified extensively by observing the following:

- 1) The volume of the combustion cell used in our experiments is fixed:  $d\mathcal{V} = 0$
- 2) No significant leaks out of the chamber have been observed and there are no pistons or crevices:  $dm_{crevice} = 0, dm_{leak} = 0$ ; The chamber leaks have been monitored by checking the pressure a minute after the combustion event has ended. Since most of the heat is lost to the wall by that point, the pressure should return to the initial chamber pressure. The chamber leak can then be determined by taking the difference:  $dp_{leak} = dp_f - dp_0$ . In our experiments  $dp_{leak} < 1$  mbar. Therefore, we concluded that chamber leaks are negligible.

3) Since there are no leaks and no crevices, this means that there is not flux in/out of the chamber:  $\{\sum_{out} \dot{m}h - \sum_{in} \dot{m}h\} = 0$ . For internal combustion piston engines, this term has to be evaluated, however, as it can play a significant role in cylinder energy balance depending on the crevice volume. An analysis that takes into account the flux in/out of the crevices is presented in Heywood<sup>119</sup>.

Under these assumptions, the rate of heat release inside for the experiments conducted inside the pressure cell becomes:

$$\dot{Q}_{ch} = \frac{1}{k_{mix} - 1} V \frac{dp}{dt} + \dot{Q}_w \quad (4.9)$$

Equation (4.9) can be used to determine the heat released during the combustion event based on the measured pressure vs. time curve (generated by the transducer). Nonetheless, the equation above poses some difficulties still because it assumes that the mixture composition and temperature are known such that the specific heat ratio,  $k_{mix}$ , can be evaluated. In addition, the heat lost to the wall also needs to be somehow estimated. In this work the ratio of specific heats is computed at the average between the initial temperature and adiabatic flame temperature (where the adiabatic flame temperature and chemical composition are determined using a chemical equilibrium solver developed in-house). The convective rate of heat loss to the wall is calculated using Newton's law of cooling:

$$\dot{Q}_w = Ah(T - T_w) \quad (4.10)$$

Where A is the surface area of the chamber, h is the heat transfer coefficient, T is the average temperature of the gas and  $T_w$  represents the wall temperature. The heat transfer coefficient is estimated by analyzing the rate of pressure decay after the combustion event as shown in Figure 4.4. The main argument made here is that, after the combustion event is completed, the chamber

pressure should remain unchanged if the process is adiabatic (since the volume is constant). Therefore, the only reason why the pressure drops is that heat is transferred to the walls. Finally, an average heat transfer coefficient is obtained by computing the slope of pressure decay over a few tens of milliseconds:

$$h = \frac{1}{A(T(t) - T_w)(k_{mix} - 1)} V \frac{dp}{dt} \quad (4.11)$$

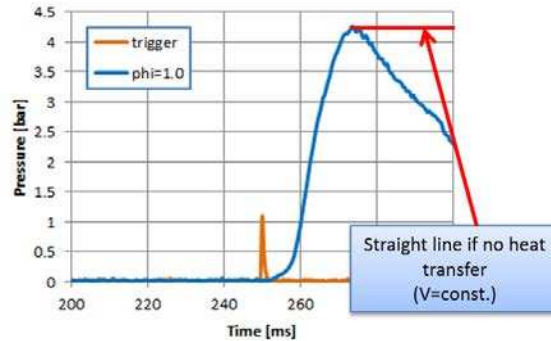


Figure 4.4: Analysis of the pressure data collected during combustion. By assuming the pressure decay is primarily due to heat transfer one can estimate the average heat transfer coefficient.

It is important to note at this stage that this analysis is only possible if the pressure transducer is compensated for high temperature. Otherwise, the pressure decay rate cannot be trusted for making estimates of the heat transfer to the wall. For the experiments reported here the heat lost to the wall is generally less than 20% of the total heat release (depending on the equivalence ratio).

## 4.2 Lean Limit & Combustion Efficiency

The capabilities of the dual-pulse pre-ionization technique are presented here in contrast with classical laser induced spark ignition of propane-air mixtures. Figure 4.5 shows the pressure data collected during the combustion events for both ignition methods. For all test condition the initial pressure inside of the chamber was set to 1 bar and the combustion chamber was heated to 323 K (50°C). This elevated initial temperature was chosen to enhance the molecular mixing of the reactants thus reducing the wait time between tests. In addition, it was also observed upon

preliminary testing that during the combustion events initiated at room temperature the flame sometimes transitions from an initially steady propagating flame to a homogenous ignition of the entire mixture. This behavior has been observed by others for large hydrocarbon fuels and it is associated with low-temperature chemical kinetics<sup>120,121</sup>. Increasing the initial chamber temperature eliminated this issue. For both laser ignition methods, the equivalence ratio of the mixture was varied such that the lean limit (defined here as the leanest mixture which resulted in a pressure rise) can be determined. In the case of laser spark ignition, the energy of the NIR pulse was set to 75 mJ. This was sufficient to consistently generate sparks (100% of the time) in all the mixture that were tested. Figure 4.5-left shows that the leanest mixture that was successfully ignited using this method was  $\phi=0.7$ . An investigation of the pressure curves also show that the ignition delay increases as leaner mixtures are attempted. Additionally, the pressure rise rate is lower towards the lean limit which indicates a decrease in flame speed for the leaner mixtures. For the dual-pulse method the laser energies were set to 20 mJ for the UV pulse and 30 mJ for the NIR. To relate this back to the analysis performed in Chapter 3, this dual-pulse energy levels lead to the generation of a visible plasma. However, the plasma density and temperatures are lower than a typical laser spark<sup>86,122</sup>. Pressure data presented in Figure 4.5-right shows that the dual-pulse technique lead to the extension of the lean limit to  $\phi=0.6$  for propane-air mixtures. Moreover, it is important to note that the lowering of the lean limit was also achieved with a combined lower pulse energy (50 mJ were required for the dual-pulse as opposed to 75 mJ for the NIR laser induced spark ignition).

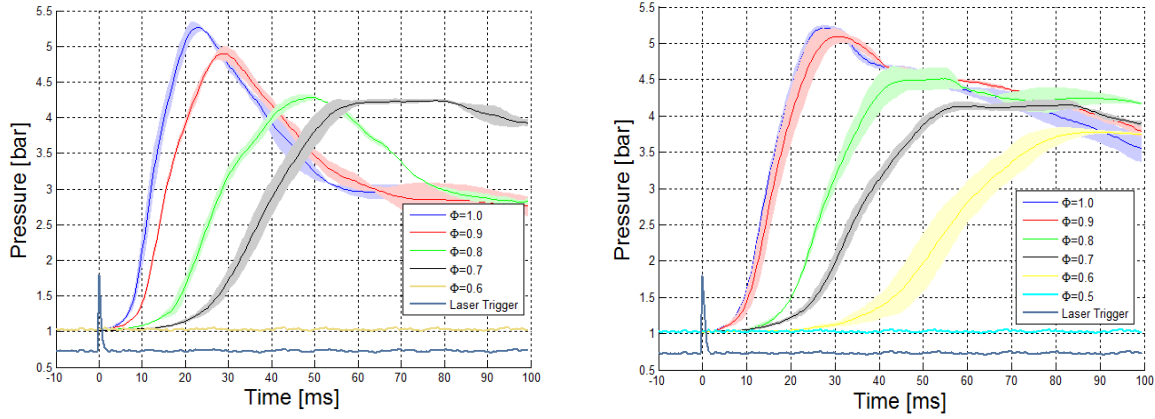


Figure 4.5: Pressure curves showing the ignition of propane-air mixture at various equivalence ratios for NIR laser spark induced ignition (left) and dual-pulse pre-ionization (right). Each curve represents the average of three tests and the shaded area is +/- one standard deviation. The initial conditions were in both cases  $p_0=1$  bar,  $T_0=323$ K.

An investigation of the lean limit for propane-air mixtures ignited with both single- and dual-pulse techniques was performed by examining the efficiency of converting the fuel chemical energy into heat. The total available chemical energy of the fuel is computed in terms of the lower heating value (LHV) as:

$$E_{fuel} = m_{fuel} \times LHV \quad (4.12)$$

where  $m_{fuel}$  represents the mass of propane added into the chamber. The apparent heat release,  $Q$ , can be directly determined from the pressure time history using Eq. (4.9) derived previously.

Finally, the combustion efficiency,  $\eta$ , is estimated as the ratio between the apparent heat release and the fuel energy content:

$$\eta = Q/E_{fuel} \quad (4.13)$$

Figure 4.6 shows the combustion efficiency for both methods as a function of equivalence ratio. Each data point represents the average of  $\eta$  from three repeated tests. For both methods, the

efficiency drops at sufficiently lean conditions allowing identification of the lean limit. For increasingly lean conditions, the combustion efficiency of the single-pulse method is lower than for the dual-pulse case. These results demonstrate the ability of the dual-pulse method to extend the lean limit relative to conventional laser ignition.

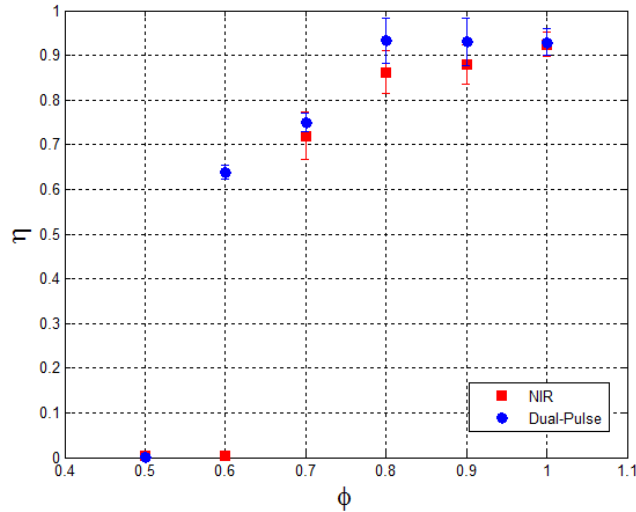


Figure 4.6: Combustion efficiency for NIR laser spark ignition (red) and Dual-Pulse (blue) at various propane-air equivalence ratios. Each point represents the average of three tests and the error bars are +/- one standard deviation.

### 4.3 Flame Visualization Using OH\* Chemiluminescence

#### 4.3.1 Single-Pulse Laser Ignition

The first set of experiments investigated ignition of propane-air mixture using single NIR laser pulses, i.e. conventional laser ignition approach. The NIR laser energy was set to  $E=75$  mJ to ensure reliable laser plasma formation, i.e. “sparking” with 100% probability. In this way, any non-combusting cases are due to problems with flame kernel growth, not simply lack of an initiation spark. OH\* chemiluminescence images collected at various equivalence ratios are presented in Figure 4.7. The top row of images show flame kernel development and propagation

at  $\phi=1.0$ . Under these conditions, one can clearly observe the toroidal flame structure that was previously reported by other researchers as well as the presence of the front (third) lobe on the upstream side<sup>26</sup>. The flame dynamics in this case are largely dictated by the flow vorticity induced during plasma recombination and cooling<sup>26,63</sup>. At leaner conditions, for example in the middle row of images for which  $\phi=0.7$ , the front lobe detaches causing the flame kernel to break into two separate flamelets. The splitting of the kernel at lean conditions is attributed to flame stretching induced by the vorticity effects of the laser plasma. At even leaner conditions, i.e. the bottom row of images for which  $\phi=0.6$ , the flame kernel never develops into a self-propagating flame.

The image sequences suggest a relationship between the moment of lobe separation and ensuing flame quenching. In the lean mixtures cases, one can observe that the separation of the third lobe negatively impacts the rate of growth of the remaining flame kernel. For example, for  $\phi =0.7$ , the kernel at 5 ms is observed to be similar in size with that at  $\sim 1$  ms (or earlier) for  $\phi =1.0$ . The third lobe likely plays an important role in flame propagation by transporting radical species along the longitudinal (laser propagation) axis of the flame, such that its separation can have a dramatic impact on subsequent flame propagation. This idea is also supported by Bradley et al.<sup>26</sup> where, by comparing the propagation distances of the third lobe in combustible and pure air mixtures, it was concluded that the propagation of the third lobe is chemically enhanced. For the non-propagating case at  $\phi=0.6$ , one observes that once the third lobe becomes separated, the chemiluminescence signal decreases significantly even in the main kernel. This is likely indicative of the termination of chain branching chemical reactions and leads to complete extinction a few hundred microseconds later. The behaviors of third lobe separation and flame quenching are more readily apparent in the present chemiluminescence imaging (of OH\*), since it provides direct

chemical information, as compared to past work that has predominantly used shadowgraph or Schlieren, which probes variations in index-of-refraction (mainly due to gas heating)<sup>24,59,64,123</sup>.

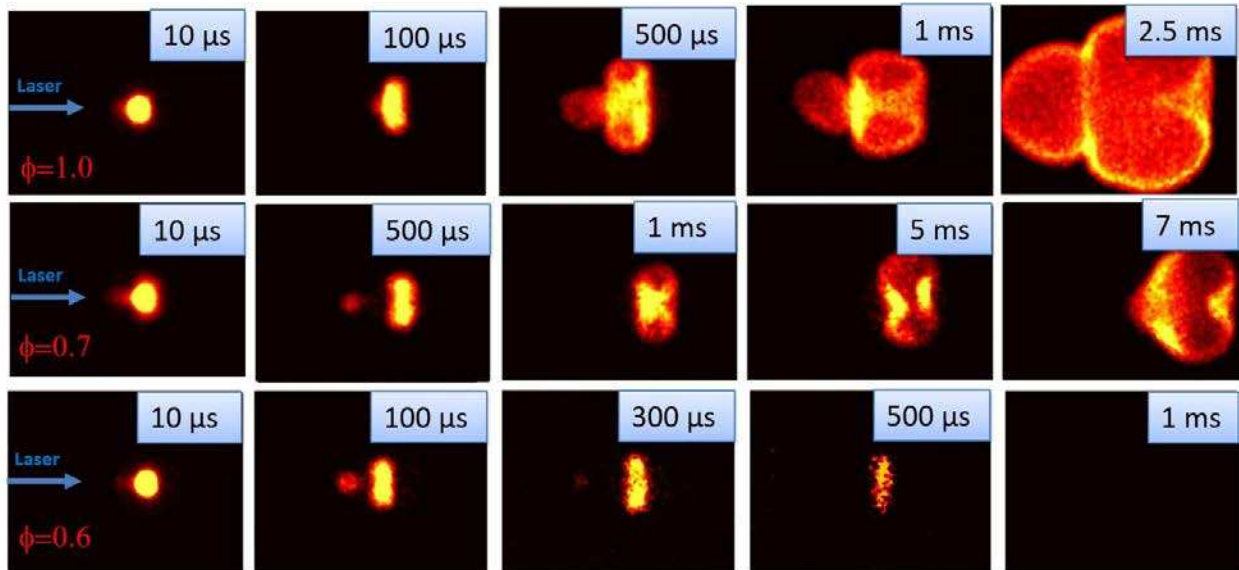


Figure 4.7: Flame kernel development during single-pulse ignition of propane air mixtures at  $\phi=1.0$  (top),  $\phi=0.7$  (middle), and  $\phi=0.6$  (bottom). The third lobe separates from the main kernel and is a precursor to flame quenching for the lean mixtures. Each image frame has field of view: 22 mm x 16 mm.

### 4.3.2 Dual-Pulse Laser Ignition

Here we conduct a similar study using the dual-pulse technique with a combination of UV pre-ionization and NIR energy addition pulses. Results of OH\* chemiluminescence imaging of the dual-pulse method are presented in Figure 4.8. The laser energy for the UV pre-ionization pulse was 20 mJ while the NIR energy addition pulse was set to 40 mJ corresponding to a total delivered energy of 60 mJ (compared to 75 mJ for the single-pulse NIR laser spark ignition). For the results presented in Figure 4.8, the UV and NIR focal spots were axially overlapped along the beam path (zero offset) and the delay between the two pulses was set to 15 ns. Clearly, the flame dynamics are very different for the dual-pulse case as compared to single-pulse. We find that the dual-pulse technique allows one to suppress the formation of the third lobe by adjustment of the axial offset,

which in turn has a significant impact on flame growth. For the stoichiometric case, i.e.  $\phi=1.0$  in the top row of Figure 4.8, the ignition conditions yield a quasi-spherical flame – quite different from its single-pulse counterpart (top row of Figure 4.7). Moreover, the dual-pulse method, even with lower total energy, provides an extension of the lean limit as successful flame growth is observed for the  $\phi=0.6$  (which extinguished with single-pulse). These findings have been repeatedly demonstrated over multiple experiments (10-15 tests of each case). The suppression of the third lobe avoids the problems associated with its detachment as further discussed below.

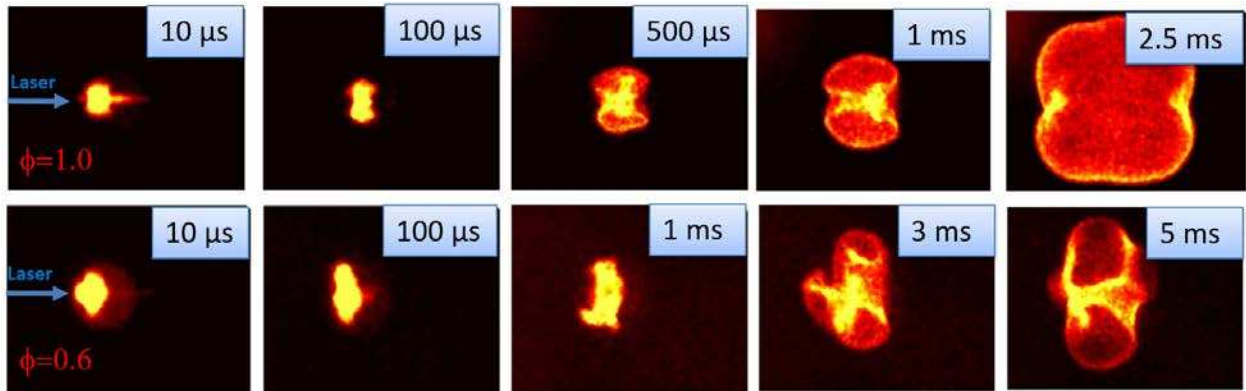


Figure 4.8: Early flame kernel development during dual-pulse ignition of propane-air mixtures at  $\phi=1.0$  (top) and  $\phi=0.6$  (bottom). Note that no third lobe is observed in this case. Each image frame has field of view: 22 mm x 16 mm.

### 4.3.3 Flame Speed Enhancement

To quantify the impact of the plasma induced vorticity on the flame propagation we examine the flame speeds in different directions,  $V_x$  and  $V_y$ , where  $x$  is defined to be along the laser beam and  $y$  perpendicular to it. The analysis is based on temporal image sequences from the OH\* chemiluminescence study. The flame speeds are determined from changes of the flame edge position relative to the center of the toroid. (The flame edge is indicated by the OH\* chemiluminescence edge which is found from its maximum gradient.) The  $x$ - speed component considers the change in (lateral) flame edge position as it moves towards the laser, while the  $y$ -

component is found from the furthest flame (transverse) edge away from the center line. The flame speed data presented in Figure 4.9 is normalized by the theoretical unstretched laminar flame speed,  $V_s$ , and plotted for both single- and dual-pulse ignition. For the stoichiometric case considered here, an unstretched laminar burning velocity of 0.3 m/s is used to compute the laminar flame speed<sup>124</sup>. For the single-pulse (NIR) case, shown in the left of Figure 4.9, one observes that excessive stretching is present at early times. In particular, the flame speed in the  $y$ -direction is  $\sim 13$  times higher than the unstretched laminar speed at early times. Conversely, as shown in the right of Figure 4.9, the stretching effects exhibited by the dual-pulse are much lower (only  $\sim 4$  times larger than the laminar speed). These findings support the idea that the flame breakdown for the NIR laser spark ignition under lean limit results from excessive stretching. Therefore, it is reasonable to conclude that the dual-pulse technique extends the combustion lean limit by reducing flame stretch through suitable alignment of the two beams to suppress the third lobe.

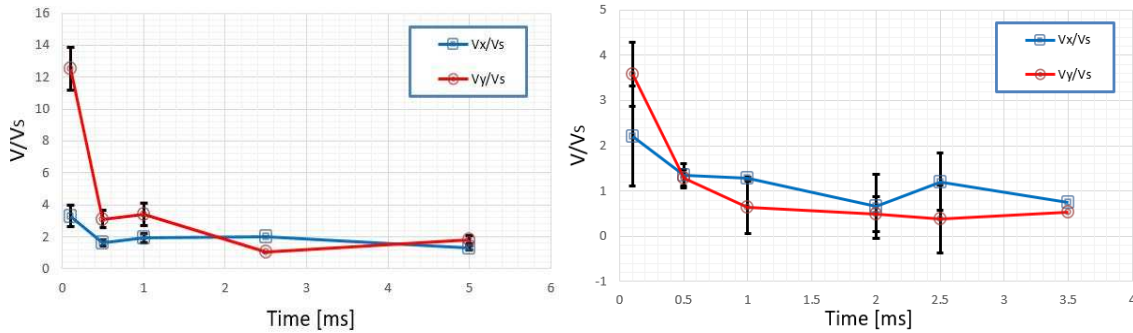


Figure 4.9: Normalized flame speed for a  $\phi=1.0$  propane-mixture for the laser breakdown ignited mixtures (left) and dual-pulse (right). Error bars represent  $\pm$  one standard deviation.

#### 4.4 Control of Flame Kernel Aerodynamics

In the dual-pulse case, the formation of toroidal structures (and the associated vorticity) has been found to depend strongly on the spatial overlap and offset of the focal spots. Figure 4.10 shows how the flame dynamics are influenced by changing the axial offset between the focal spot positions of the two pulses (experimentally achieved with a translation stage for the focusing lens

for the NIR beam). For the left image of Figure 4.10 the NIR focal spot is 2 mm upstream of the UV, for the middle image the offset is zero (corresponding to the case presented in Figure 4.8), while for the right image the NIR focal spot is 2 mm downstream of the UV. In the experimental cases with an offset, a lobe structure tends to appear on the NIR side (i.e. towards the laser in the left image, and away from the laser in the right image). The fluid dynamics that accompany the recombination and plasma kernel cooling stages dictate the propagation direction of the flame. More specifically, depending if the NIR pulse is focused in front or behind the waist of the UV pre-ionization pulse, the counter-rotating vortices formed on either side of the plasma kernel are going to exhibit different strengths. From a fluid dynamics perspective, the differing strength is due to the fact that the epicenter of the (single) shock wave is always biased towards the location of the NIR beam waist (due to the non-uniform energy deposition which is strongest at the avalanche location). The differential vorticity leads to the generation of a third lobe propagating towards the left or right as shown in Figure 4.10. If the beam waists of the NIR and UV pulses are overlapped along the laser propagation axis, the two counter-rotating vortices have equal strength and the development of the third lobe is suppressed. A more detailed discussion of the flow field that accompanies the plasma recombination is presented in the numerical modeling chapter of this dissertation.

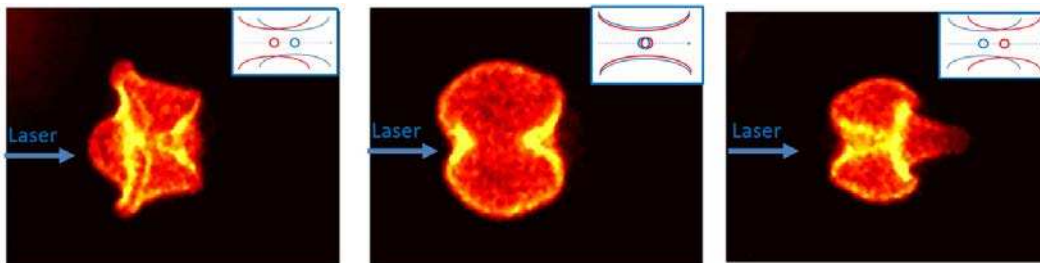


Figure 4.10: Dynamics of the flame kernel based on the spatial overlap between the two laser pulses. The images were all taken at delay of 1 ms with respect to the laser firing. Inserts at the top right corner shows the spatial overlap of the UV (blue) and NIR (red) beam waists. (The beams in the middle insert are laterally offset for visual clarity.)

A study examining the absorbed pulse energies for the different beam offsets was also conducted. A plot of the energy absorbed for the NIR as a function of spatial overlap between the two beam is presented in Figure 4.11. The results show that the total energy deposited in the dual-pulse case ( $\sim 2$  mJ absorbed due to UV plus  $\sim 13$  mJ absorbed from NIR) is similar to that absorbed when the NIR pulse is applied on its own ( $\sim 15$  mJ absorbed due to the NIR only). This is, of course, expected for the UV pulse, since its conditions are not changed by this offset, and the lack of change of the IR energy absorption is attributed to the fact that all offsets studied are still within the Rayleigh range of the UV beam ( $\sim 3$  cm). This is a very important finding because it suggests that the lean limit is governed by the flame dynamics induced by the plasma rather than the amount of energy absorbed into the ignition kernel. Moreover, this results further motivates the numerical study of the fluid flow field induced by the plasma kernels presented in the next chapter.

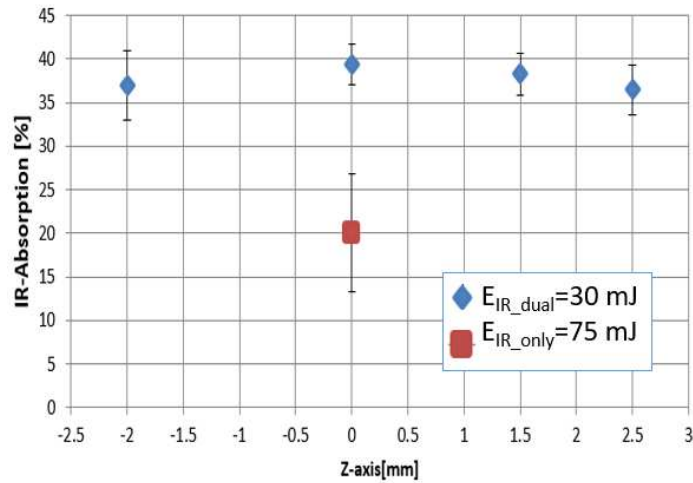


Figure 4.11: IR laser energy absorbed as a function of spatial overlap between the two pulses. Show in red is the IR pulse on its own.

## CHAPTER 5:

### Numerical Modeling of Laser Ignition

The motivation for developing a numerical code to investigate the laser plasma induced fluid mechanics stems from the need to understand how the energy deposition around the beam waist during the initial plasma formation stage influences the thermal/fluid dynamics processes that are dominant after plasma recombination. One of the main experimental findings from the previous chapter was that the flame kernel aerodynamics can be controlled using the dual-pulse laser ignition method. Therefore, it is important to look at how does the flow field generated in the hot gas kernel changes as a function of dual-pulse overlap. The ignition kernel is modelled here as a hot spot in which energy is added either uniformly along the optical axis or with a small offset between the two pulses.

Previous studies have demonstrated that the formation of the toroidal structure that is characteristic to laser ignition as well as pin-to-pin electrode discharge ignition does not depend on chemistry<sup>63,66,67</sup>. Therefore, plasma and combustion chemistry have been neglected for the purpose of this investigation. This is equivalent to generating a hot kernel in an inert gas (such as Ar, Xe, N<sub>2</sub> or He) and follow its evolution. In fact, the formation of the toroidal structure that follows laser breakdown has been demonstrated in various non-igniting mixtures<sup>26,64,125</sup>. The novelty of this modeling work is that we are investigating the kernel aerodynamics under dual-pulse conditions with varying degrees of overlap between the pre-ionization and NIR beams.

## 5.1 Mathematical Model

This section introduces the governing equations for the flow induced by the dual-pulse laser plasma. This consists of a system of partial differential equations (PDEs) describing the conservation of mass, conservation of momentum and conservation of energy. It is important to note that the geometry of the laser spark makes it possible to describe the entire 3-D flow field only by solving the 2-D axis-symmetric equations in a cylindrical coordinate system. This significantly reduces the computational time. The main challenge is represented by the fact that the temperature of the hot kernel reaches values on the order of 10,000 K. Under this conditions one would expect the gas mixture to be dissociated as well as becoming partially ionized. However, the model presented here ignores this effects by keeping the chemistry of the working fluid frozen. This represents the biggest approximation in the model developed here. On the other hand, assuming a calorically perfect gas would be a too crude approximation given the high temperatures of the gas kernel. In this study, the gas is assumed to consist of pure molecular nitrogen but it's thermodynamic properties are allowed to change with temperature thereby making the working fluid a thermally perfect gas. The relaxation of the calorically perfect gas assumption raises some challenges when integrating the system of conservation laws and these issues will be discussed in detail in the subsequent sections.

### 5.1.1 Governing Equations

The fluid flow induced by the laser breakdown process is modelled numerically by solving the Navier-Stokes conservation equations. The governing equations written in cylindrical coordinates with axial symmetry and zero azimuthal velocity are presented below in conservative form<sup>126</sup>:

$$U_t + F(U)^a_r + G(U)^a_z = F(U)^d_r + G(U)^d_z + S(U) \quad (5.1)$$

Where  $U$  is the vector of conserved variables:

$$U = \begin{bmatrix} \rho \\ \rho u \\ \rho v \\ E \end{bmatrix} \quad (5.2)$$

and  $F(U)^a$ ,  $G(U)^a$  represent the advective flux in the r-direction and z-direction respectively:

$$F(U)^a = \begin{bmatrix} \rho u \\ \rho u^2 + p \\ \rho uv \\ u(E + p) \end{bmatrix}; \quad G(U)^a = \begin{bmatrix} \rho v \\ \rho uv \\ \rho v^2 + p \\ v(E + p) \end{bmatrix} \quad (5.3)$$

For modeling the evolution of the hot gas kernel generated by the lasers, the diffusive flux  $F(U)^d$  and  $G(U)^d$  also needs to be considered:

$$F(U)^d = \begin{bmatrix} 0 \\ \tau_{rr} \\ \tau_{rz} \\ u\tau_{rr} + v\tau_{rz} - q_r \end{bmatrix}; \quad G(U)^d = \begin{bmatrix} 0 \\ \tau_{rz} \\ \tau_{zz} \\ u\tau_{rz} + v\tau_{zz} - q_z \end{bmatrix} \quad (5.4)$$

Finally, a source term appears in the system of equations (5.1) due to the change of coordinate systems from Cartesian to Cylindrical:

$$S(U) = -\frac{\delta}{r} \begin{bmatrix} \rho u \\ \rho u^2 - \tau_{rr} \\ \rho uv - \tau_{rz} \\ u(E + p) - u\tau_{rr} - v\tau_{rz} + q_r \end{bmatrix} \quad (5.5)$$

### 5.1.2 Thermodynamic Relations

The set of governing equations described by the relations (5.1)-(5.5) is not sufficient for describing the state of the system. In fact, a closer look shows that there are not sufficient relations

for the number of unknowns present to properly close the problem. The governing equations provide four relations: conservation of mass (the first row in vector form notation), conservation of momentum (second and third row) and conservation of energy (fourth row) but yield five unknowns: density, velocity (in both r-direction and z-direction), pressure and energy. The closure problem is resolved by considering the thermodynamic properties of the medium. This introduces new variables but also provides more relations between the variables. For example, the flow pressure can be related to the temperature of the fluid using the equation of state of an ideal gas:

$$p = \rho R_g T \quad (5.6)$$

where  $R_g$  represents the specific gas constant ( $R_g = 297 \text{ J/kg K}$ ). This provides another relation between the pressure and density of the fluid but also introduces temperature as a new unknown into the problem. An additional relation that describes the state of a thermally ideal gas is required. The energy of the system can be split into two components: internal energy and kinetic energy as follows:

$$E = \rho \left( e + \frac{u^2 + v^2}{2} \right) \quad (5.7)$$

The temperature dependence is introduced into equation (5.7) by writing the internal energy in terms of the fluid enthalpy:

$$E = \rho \left( h - \frac{p}{\rho} + \frac{u^2 + v^2}{2} \right) \quad (5.8)$$

The enthalpy is defined as:

$$h(T) = h_0^f + \int_{T_{ref}}^T c_p(T) dT \quad (5.9)$$

where the first term in (5.9) represents the heat of formation (zero in the case of nitrogen at standard conditions) and the second term represents the sensible enthalpy. In a calorically perfect gas, the

specific heat,  $c_p$ , is independent of temperature and a straightforward explicit relationship between energy, temperature, density and pressure can be obtained by substituting (5.6) and (5.9) into (5.8). For a thermally perfect gas the temperature is obtained by solving the following implicit equation in each domain cell at each time step<sup>127</sup>:

$$T = \frac{-E + \rho \left( \frac{u^2 + v^2}{2} \right) + \rho h(T)}{\rho R_g} \quad (5.10)$$

The enthalpy is solved in the numerical code using the Shomate interpolation polynomials for molecular nitrogen according to the NIST database. A solution procedure for Eq. (5.10) is described in Appendix A:. The problem is finally closed if the system of governing equations (5.1)-(5.5) is solved together with the thermodynamic relations: (5.6), (5.9) and (5.10).

### 5.1.3 Transport Properties

The transport properties need to be included to complete the description of the mathematical model. The physical effects of viscosity are captured in the molecular stress tensor that appears in relations (5.4) and (5.5). Denoting the viscous stress by  $\Pi_{i,j}$  and the deformation tensor by  $D_{i,j}$  we have:

$$\Pi_{i,j} = \begin{bmatrix} \tau_{rr} & \tau_{r\theta} & \tau_{rz} \\ \tau_{\theta r} & \tau_{\theta\theta} & \tau_{\theta z} \\ \tau_{zr} & \tau_{z\theta} & \tau_{zz} \end{bmatrix}; \quad D_{i,j} = \begin{bmatrix} u_r & \frac{1}{2}(v_r + u_\theta) & \frac{1}{2}(w_r + u_z) \\ \frac{1}{2}(u_\theta + v_r) & v_\theta & \frac{1}{2}(w_\theta + v_z) \\ \frac{1}{2}(u_z + w_r) & \frac{1}{2}(v_z + w_\theta) & w_z \end{bmatrix} \quad (5.11)$$

Under the Newtonian approximation the stress tensor is linearly proportional to the rate of strain of the fluid (i.e. the rate of deformation over time) and the following expression for the stress is obtained:

$$\Pi_{i,j} = 2\mu D_{i,j} + \left( \mu_B + \frac{2}{3}\mu \right) (\nabla \cdot \vec{V}) \quad (5.12)$$

For the 2-D axis-symmetric simulation all the azimuthal components to the stress tensor are ignored. Additionally, the bulk viscosity can be neglected ( $\mu_B = 0$ ) for pure nitrogen mixture<sup>128</sup>. The dynamic viscosity depends strongly on the temperature. For non-reacting gases at relatively low temperatures an accurate approximation is given by Sutherland:

$$\mu(T) = \mu_{ref} \left( \frac{T}{T_{ref}} \right)^{3/2} \frac{T_{ref} + T_S}{T + T_S} \quad (5.13)$$

Where:  $\mu_{ref}$  and  $T_{ref}$  are the dynamic viscosity and temperature at a reference state and  $T_S$  is the so-called Sutherland temperature coefficient. For molecular nitrogen we have:  $\mu_{ref} = 1.78 \times 10^{-5} \text{ kg}/(\text{m} \cdot \text{s})$ ,  $T_{ref} = 300.55 \text{ K}$  and  $T_S = 111 \text{ K}$ . Equation (5.13) represents the second important approximation made in this mathematical model. For gas mixtures in which ionization is present the viscosity is a highly non-linear function of temperature. In fact, at temperature above 10,000 K the viscosity decreases with temperature due long-range Coulomb interactions between charge particles<sup>129</sup>. Nonetheless, for temperatures below 6,000 K the viscosity can be approximated accurately using Sutherland's formula.

The heat conduction present in relations (5.4) and (5.5) is defined using Fourier's law:

$$\mathbf{q} = -k \nabla T \quad (5.14)$$

In the most general sense, there are three contributions to the thermal conductivity coming from the internal degrees of freedom of the molecules, translational motion and chemical reaction effects. However, a good approximation can be obtained if the thermal conductivity is directly related to the fluid's specific heat and the dynamic viscosity through the Prandtl number:

$$Pr = \frac{c_p \mu}{k} \quad (5.15)$$

In this investigation the Prandtl number was set to:  $Pr = 0.7$ .

## 5.2 Numerical Methods

The conservative formulation of the governing equations presents several advantages from a numerical point of view. When written in the form shown in Eq. (5.1) one can separate the effect of advection from those of diffusion and heat conduction. If the right-hand side of (5.1) is made equal to zero then the system of conservation laws is equivalent to the Euler's equations. In this case the problem is one of pure advection. Such a system of equation can be used successfully for compressible flow problems when the effects of viscosity and thermal conductivity can be neglected. Problems involving the propagation of shock waves inside nozzles and around objects usually fall in this category<sup>130</sup>. Alternatively, if the left-hand side is made equal to zero, the system of equations (5.1) can be used to describe flows driven by viscosity. Problems such as Couette flow can be solved using this system of equations. Finally, the source term (5.5), can be used to transfer the equations between a cartesian, cylindrical or spherical system of coordinates. More precisely, if  $\delta = 0$ , the source term is equal to zero. This is equivalent to solving the conservation laws in cartesian coordinates. If  $\delta = 1$ , the system of equations describes a problem of cylindrical geometry. Lastly,  $\delta = 2$ , casts the conservation laws on a spherical coordinate system.

### 5.2.1 Physical Properties of the Advection Problem

The most challenging part for developing a solution for the system of governing equations is solving the advection PDE problem (5.23). Therefore, advection represents the critical problem in developing numerical methods for solving the governing equations and a discussion of its physical properties is useful before introducing the numerical techniques.

In general, a homogeneous second-order PDE's in two independent variables (x,y) and one dependent variable  $u(x,y)$  can be written as follows<sup>131</sup>:

$$Au_{xx} + Bu_{xy} + Cu_{yy} + Du_x + Eu_y + Fu = 0 \quad (5.16)$$

The mathematical problems solved by differential equations of the type (5.16) can be classified into three categories depending on the sign of the discriminant  $B^2 - 4AC$  as show in Table 5.1.

Table 5.1: Classification of second order PDEs

<b>B<sup>2</sup>- 4AC</b>	<b>Characteristics</b>	<b>Type</b>
Negative	2 imaginary solutions	Elliptic
Zero	1 repeated real solution	Parabolic
Positive	2 real solutions	Hyperbolic

Physically, this classification is important because the solution of the discriminant equation tells one how the information is propagating through the domain which, in turn, influences what type of numerical method is used to solve the PDEs. Accordingly, if the discriminant is negative the equations are called elliptical. In this case, there are no characteristic directions over which information propagates and any disturbance created inside a domain affects all the points in the domain with infinite propagation speed (see Figure 5.1-(a)). In real-world applications this corresponds to equilibrium problems in which all discontinuities have been smoothed. One example is the Laplace equation which describes the steady state heat equation. On the other hand, parabolic and hyperbolic equations have real characteristic paths. This means that a disturbance in the domain has a range of influence. In the case of parabolic equations that have only one repeated real characteristic, information propagates over the domain but with a decreasing effect as the distance from location of the perturbation is increasing. Physical problems involving parabolic equations typically involve dissipative process (such as diffusion or heat conduction). This type of problems are usually solved using time marching techniques since the solution at a given time level only depends on previous information (see Figure 5.1-(b)). Hyperbolic equations have

distinct real roots. From a physical point of view, this means that information can only propagate over certain characteristic directions dictated by the eigenstructure of the system. A disturbance create in the domain will propagate at a finite speed over a finite region of the domain that is bounded by the characteristics of the system (see Figure 5.1-(c)). Wave propagation problems (or “advection-like” problems) are typical examples of physical problems that are solved by hyperbolic PDEs.

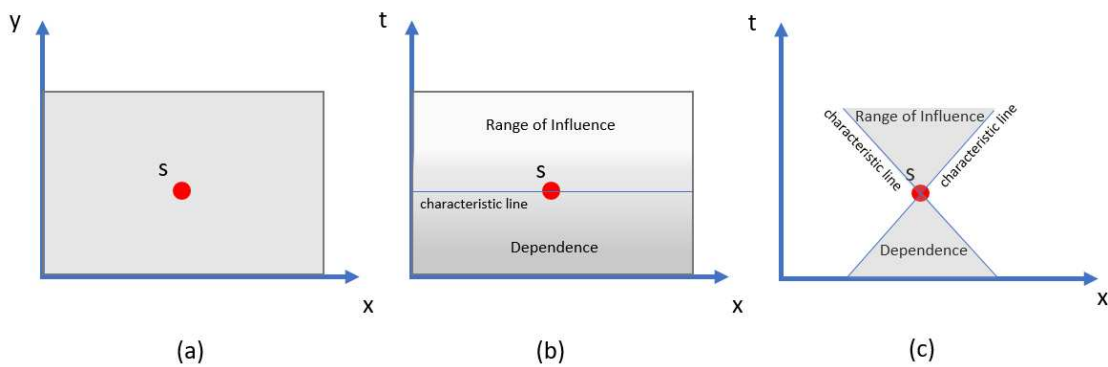


Figure 5.1: Schematic showing the domain of dependence and range of influence of a disturbance in the case of an elliptic (a), parabolic (b) and hyperbolic (c) PDE's. The color gradient in (b) is meant to show the decreasing effect of the disturbance as time progresses.

A close inspection of Eq. (5.23) shows that the system of PDE's governing the fluid flow is hyperbolic in nature. Moreover, this advection problem is nonlinear in nature which makes its mathematical treatment all the more challenging. To better understand how this affects the development of a solution it is useful to compare the second equation from the system in (5.23) with a linear advection problem:

$$\begin{cases} u_t + a u_x = 0 \\ u(x, 0) = u_0(x) \end{cases} \quad (5.17)$$

It can easily be seen that the equation above becomes an ordinary differential equation (ODE) if it is projected over the (x,t) plane since it's mathematical meaning is that the rate of change of quantity,  $u$ , is zero along  $x = x(t)$ :

$$\frac{du}{dt} = \frac{\partial u}{\partial t} + a \frac{\partial u}{\partial x} = 0 \quad (5.18)$$

This means that along a curve  $x = x(t)$  the following ODE has to hold:

$$a = \frac{dx}{dt} \quad (5.19)$$

Since the wave speed is constant the solution is simply a line whose intercept with the x-axis is dictated by the initial condition,  $x_0$ , and the slope is given by the wave speed,  $a$ :  $x(t) = x_0 + at$ . Physically these lines represent characteristics over which information propagates in time. As shown in Figure 5.2 the characteristic lines never intersect with each other because the slope is constant. Therefore, the solution of Eq. (5.17) corresponds to a translation of the initial conditions along the characteristic line to the right or to the left depending on whether the wave speed is positive or negative:

$$u(x, t) = u_0(x_0) = u_0(x - at) \quad (5.20)$$

This means that all points on the wave move at the same rate and the shape of the wave is conserved in time for a linear advection equation.

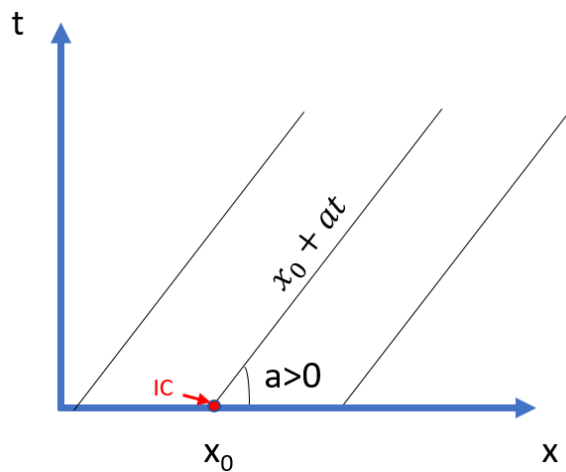


Figure 5.2: Characteristic lines for the 1-D linear advection equation

The momentum equations in (5.1) is the equivalent of a non-linear pure advection problem when all dissipative effects are neglected:

$$\begin{cases} u_t + a(u) u_x = 0 \\ u(x, 0) = u_0(x) \end{cases} \quad (5.21)$$

Following the same argumentation as for the linear advection problem the solution is given by:

$$u(x, t) = u_0[x - a(u(x))t] \quad (5.22)$$

The main observation from (5.22) is that the characteristics are not parallel anymore because the slope is not constant. Moving to a different spatial location gives a slightly different slope which implies that the characteristics are allowed to come together or distance from each other over time. Continuing the analogy with the propagation of waves, this means that the wave can get distorted as it propagates through time and space. Points can coalesce to a small region at the leading edge of the wave to form a shock or can “thin” out to form an expansion fan<sup>126</sup>. This process is described schematically in Figure 5.3 below.

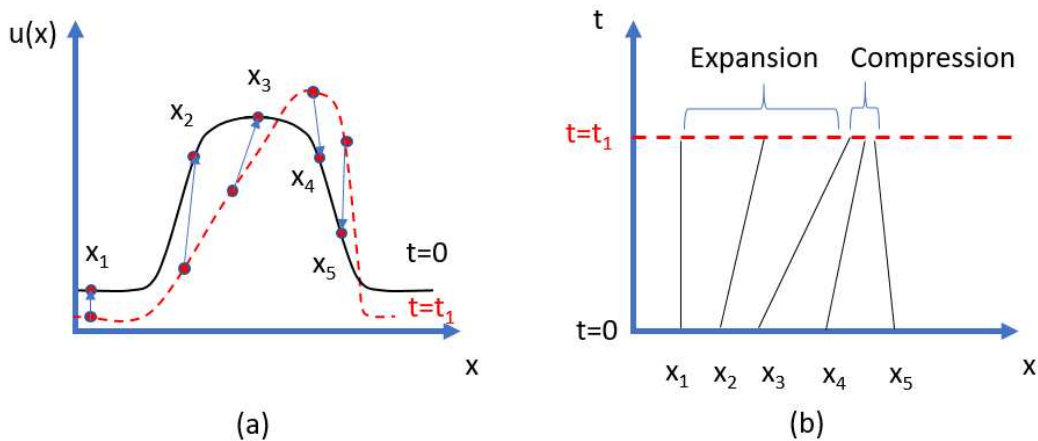


Figure 5.3: Diagram depicting a non-linear wave becoming distorted as time progresses (a) and the characteristic lines at several points on the wave (b).

The physical manifestation of this nonlinearity in the system of conservation laws (5.1) comes from the fact that the wave speed,  $\vec{V}(u, v)$ , is part of the solution (as opposed to being a

constant like in the case of a linear advection equation). This property of system (5.1) gives rise to a series of approximations and numerical methods. If the fluid domain is discretized using finite volumes, one particular class of solution methods is obtained by posing a Riemann problem at the interface of each cell. In this dissertation, the non-linear advection problem is solved using such a Riemann solver based on a linearization approach developed by Roe and Pikes that is introduced in the next section.

### 5.2.2 General Approach

In this dissertation, the Navier-Stokes system is solved by separating the advection problem from the diffusion and heat conduction effects. The advection problem is solved using a flux differencing scheme developed by Roe and Pikes<sup>132</sup> while the diffusion problem (including the source term) is discretized using a second order centered difference scheme<sup>133</sup>. After discretization, the resulting ordinary differential system is integrated using a Runge-Kutta IV time marching method. According to Toro<sup>126</sup>, the 2-D advection problem given the left-hand side of system (5.1) can be solved through the method of dimensional splitting as follows:

$$\text{r-split problem: } \begin{cases} PDE: & U_t + F(U)_r = 0 \\ ICs: & U^n \end{cases} \xrightarrow{\Delta t} U^{n+\frac{1}{2}} \quad (5.23)$$

$$\text{z-split problem: } \begin{cases} PDE: & U_t + G(U)_z = 0 \\ ICs: & U^{n+\frac{1}{2}} \end{cases} \xrightarrow{\Delta t} U^{n+1}$$

Based on Eq. (5.23) the solution at time step,  $n$ , is advanced to  $n+1$  by first solving the 1-D advection problem in the r-direction. This acts like half a step in the algorithm and the result of the r-split problem,  $U^{n+\frac{1}{2}}$  is then used as an initial condition for solving the z-split problem. If we denote the by  $\mathcal{R}^{(\Delta t)}$  and  $\mathcal{Z}^{(\Delta t)}$  the solution operators for the r-split and the z-split problems then it can be shown that the solution at the next time step,  $U^{n+1}$ , is obtained as follows<sup>126,134</sup>:

$$U^{n+1} = \mathcal{Z}^{(\Delta t)} \mathcal{R}^{(\Delta t)} U^n \quad (5.24)$$

The dimensional splitting method described by (5.23) and (5.24) simplifies the numerical procedure because it only requires the development of a single algorithm for the 1-D advection problem that is applied twice (once for each spatial direction).

A splitting scheme can also be applied for an inhomogeneous system as is the case of the conservation laws in (5.1) which includes the diffusive flux and the source term on the right-hand side:

$$\begin{aligned} \text{advection problem: } & \begin{cases} PDE: & U_t + F(U)_r + G(U)_z = 0 & \xrightarrow{\Delta t} \bar{U}^{n+1} \\ ICS: & U^n \end{cases} \\ & (5.25) \\ \text{source problem: } & \begin{cases} ODE: & U_t = D(U) & \xrightarrow{\Delta t} U^n \\ ICS: & \bar{U}^{n+1} \end{cases} \end{aligned}$$

The advection problem is solved first using dimensional splitting (Eq. (5.23)) and the result is used as an initial condition for solving the ODE of the source problem obtained after the finite volume discretization of the diffusive flux and source term,  $D(U)$ .

Overall, solving the system of conservation laws governed by Eq. (5.1) is equivalent to solving three separate problems: advection PDEs (in both direction) and source ODEs. If we denote by  $\mathcal{D}^{(\Delta t)}$  the solution operator for the source ODE, then the global solution at time  $n+1$  is obtained:

$$U^{n+1} = \mathcal{Z}^{(\Delta t)} \mathcal{R}^{(\Delta t)} \mathcal{D}^{(\Delta t)} U^n \quad (5.26)$$

In the subsequent section the solution procedure for each of the problems will be described in detail.

### 5.2.3 Roe-Pikes Method

The main concern is to find a numerical solution for the initial boundary value problem (IBVP) posed by on one of the dimensional splits of Eq (5.23). The discussion in this section is largely based on Toro who describes in great detail various Riemann solvers for systems of non-linear conservation laws<sup>126</sup>. The motivation is to provide only a general description of the particular numerical technique used in the CFD code developed in this dissertation. An IBVP based on the r-split 2-D problem can be written as follows:

$$\begin{cases} PDEs: & U_t + F(U)_r = 0 \\ ICs: & U(r, 0) = U_0(r) \\ BCs: & U(0, t) = U_L(t), \quad U(r, t) = U_R(t) \end{cases} \quad (5.27)$$

When the IBVP is discretized over the computational domain shown in Figure 5.4. The PDEs are converted to ODEs that can be integrated in time using any type of time marching technique.

If one assumes a piecewise constant solution on each cell Eq. (5.27) becomes:

$$\int_{r_{i-\frac{1}{2}}}^{r_{i+\frac{1}{2}}} [U_t + F(U)_r] dr = 0 \quad \rightarrow \quad \frac{d\bar{U}_i}{dt} = \frac{1}{\Delta r} [F_{i-\frac{1}{2}} - F_{i+\frac{1}{2}}] \quad (5.28)$$

Where:  $\bar{U}_i = \frac{1}{\Delta r} \int_{r_{i-\frac{1}{2}}}^{r_{i+\frac{1}{2}}} U(t, r) dr$  is the average value of the conservative variables over the cell

$\Delta r$  and  $[F_{i-\frac{1}{2}} - F_{i+\frac{1}{2}}] = \int_{r_{i-\frac{1}{2}}}^{r_{i+\frac{1}{2}}} F(U)_r dr$  represents the intercell flux difference.

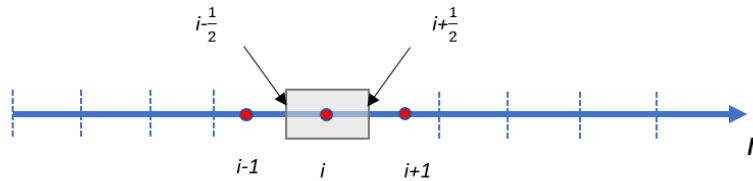


Figure 5.4: One-dimensional domain discretized using finite volumes

According to Godunov<sup>135</sup> the intercell flux can be determined if the IBVP (5.27) is converted into a Riemann problem that is solved at the interface of each cell in the computational domain:

$$\begin{cases} U_t + F(U)_r = 0 \\ U(r, 0) = \begin{cases} U_L & \text{if } r < 0 \\ U_R & \text{if } r > 0 \end{cases} \end{cases} \quad (5.29)$$

The flux is obtained as:

$$F_{i+\frac{1}{2}} = F(U_{i+\frac{1}{2}}(0)) \quad (5.30)$$

Where  $U_{i+\frac{1}{2}}(0)$  is the solution of (5.29). It is important to note at this stage that no numerical approximation have been made yet. In fact, Godunov finds an analytical solution for the intercell flux using this approach for a piece-wise distribution of initial data. However, his algorithm, albeit exact, it is not computationally efficient.

A different approach was introduced by Roe<sup>136</sup> which replaces the original Riemann problem (5.29) with a linearized approximate problem. Introducing the Jacobian matrix of the system of conservation laws,  $A(U) = \frac{\partial F}{\partial U}$ , the Riemann problem can be re-casted in the following more suitable form:

$$\begin{cases} U_t + AU_r = 0 \\ U(r, 0) = \begin{cases} U_L & \text{if } r < 0 \\ U_R & \text{if } r > 0 \end{cases} \end{cases} \quad (5.31)$$

Essentially what the Roe approach does is to replace the exact Jacobian of the system  $A(U)$  with a linearized version of itself,  $\tilde{A}(U)$ . In addition, if the system of equation describing the original IBVP is hyperbolic then the eigenvectors must be linearly independent which allows one to determine the intercell flux only by knowledge of the eigenstructure of the system's Jacobian:

$$\Delta U = U_R - U_L = U_{i+\frac{1}{2}}(0) = \sum_{i=1}^n \tilde{\alpha}_i \tilde{K}^{(i)} - \text{condition of linear independence} \quad (5.32)$$

Then, according to relation (5.30), the intercell flux is obtained as:

$$F_{i+\frac{1}{2}} = F_L + \sum_{i=1}^n \tilde{\alpha}_i \tilde{\lambda}_i \tilde{K}^{(i)} \quad (5.33)$$

Where  $\tilde{\alpha}_i, \tilde{\lambda}_i, \tilde{K}^{(i)}$  are the coefficients for linear independence, the eigenvalues and the eigenvectors of Jacobian matrix,  $\tilde{A}(U)$ . Physically they represent the wave strengths, the speed at which information is propagating and the characteristic directions over which information is propagating inside the computational domain.

One of the main challenges using Roe's original method is that it requires the knowledge of the linearized Jacobian matrix explicitly. For this reason, the code developed in this dissertation uses a variation of the original Roe's method due to Roe and Pikes<sup>132</sup> that avoids this issue by introducing an extra linearization into the problem. This approach assumes that, if the data  $U_L$  and  $U_R$  are close enough to a reference state  $\hat{U}$  then the Jacobian  $\tilde{A}(\tilde{U})$  can be replaced by  $\hat{A}(\hat{U})$  (note that this is the second approximation of the original Jacobian,  $A(U)$ ). Expressions for the wave strengths are found in this case by solving the Riemann problem (5.31) around the reference state:

$$\Delta U = U_R - U_L = \sum_{i=1}^n \hat{\alpha}_i \hat{K}^{(i)} \quad (5.34)$$

The sought solution vector,  $\tilde{W}$ , is found by evaluating the wave strengths at the average state and solving the resulting system of non-linear algebraic equations:

$$\tilde{\alpha}_i = \hat{\alpha}_i(\tilde{W}), \quad \tilde{\lambda}_i = \lambda_i(\tilde{W}), \quad \tilde{K}^{(i)} = K^{(i)}(\tilde{W}) \quad (5.35)$$

Where:

$$\tilde{W} = \begin{bmatrix} \tilde{\rho} \\ \tilde{u} \\ \tilde{v} \\ \tilde{\alpha} \end{bmatrix} \quad (5.36)$$

is the vector of primitive variables and can be obtained directly for the vector of conservative variables,  $U$ , described by (5.2). An example on how this technique can be applied for the 2-D advection problem is provided in Appendix B:.

### 5.2.4 Source Problem

If the conservation laws are solved in a coordinate system other than Cartesian then the system of PDE's describing the conservation in becomes inhomogeneous as a non-zero source term appears on the right-hand side of (5.1). Additionally, if the effects of viscosity and thermal conductivity are included then the source problem itself becomes a system of PDEs and has to be numerically discretized before the conservation laws can be integrate in time. In this work, the source problem is discretized using a finite volume centered scheme described by Edwards<sup>133</sup>:

$$D_{i,j} = \frac{1}{\Delta r} \left[ F_{i+\frac{1}{2},j}^d - F_{i-\frac{1}{2},j}^d \right] + \frac{1}{\Delta z} \left[ G_{i,j+\frac{1}{2}}^d - G_{i,j-\frac{1}{2}}^d \right] + S_{i,j} \quad (5.37)$$

In Eq (5.37) the geometrical source term and the diffusive flux were combined in a single operator:

$$D(U) = F(U)_r^d + G(U)_r^d + S(U) \quad (5.38)$$

One approach for computing the flux at the cell interface is to take the arithmetic average of the flux value in two neighboring cells. For example the flux in the r-direction at the interface of cells  $(i,j)$  and  $(i+1,j)$  is given by:

$$F_{i+\frac{1}{2},j}^d = \frac{1}{2} [F_{i,j}^d + F_{i+1,j}^d] \quad (5.39)$$

This makes the discretization of (5.38) a centered scheme. For consistency, all of the derivatives inside  $F(U)_r^d$ ,  $G(U)_r^d$  and  $S(U)$  are also discretized using a centered scheme.

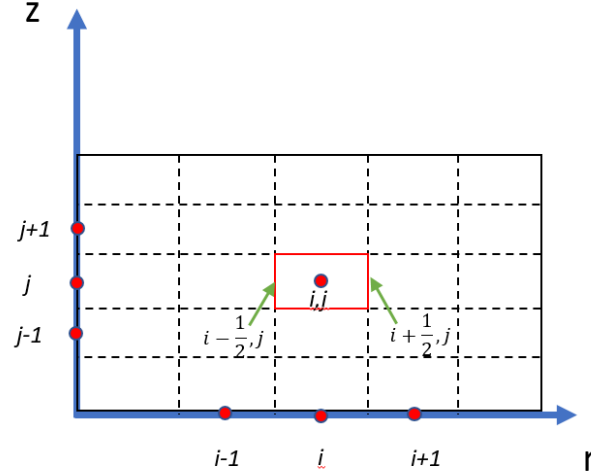


Figure 5.5: Finite volumes used for spatial discretization of the source problem.

### 5.2.5 Time Marching Technique

Once the advection flux is computed the system of governing PDEs is reduced to a system of ODEs in time of the form:

$$\begin{cases} U_t = F(t, U(t)) \\ U(t_0) = U_0 \end{cases} \quad (5.40)$$

The solution advancement from time step  $n$  to  $n+1$  is achieved in the numerical code using an explicit 4<sup>th</sup> order Runge-Kutta method<sup>137</sup>:

$$\begin{cases} U^{(1)} = U^{(n)} - \frac{\Delta t}{\Delta r} F(U^{(n)}) \\ U^{(2)} = U^{(n)} - \frac{1}{2} \frac{\Delta t}{\Delta r} F(U^{(1)}) \\ U^{(3)} = U^{(n)} - \frac{1}{2} \frac{\Delta t}{\Delta r} F(U^{(2)}) \\ U^{(4)} = U^{(n)} - \frac{1}{6} \frac{\Delta t}{\Delta r} [F(U^{(n)}) + 2F(U^{(1)}) + 2F(U^{(2)}) + F(U^{(3)})] \end{cases} \quad (5.41)$$

It is important to note that in reality the algorithm (5.41) is applied three times before a complete time step is made: after the r-split, z-split and source problem according to (5.23), (5.25) and (5.26).

For the other two problems,  $F(U)$  in Eq. (5.41) is replaced by  $G(U)$  and  $D(U)$  respectively.

The choice of time step is critical in order to ensure the numerical stability of the explicit ODE solver. In general, the time step depends on (1) the size of the mesh, (2) the speed at which information propagates through the domain (i.e. the wave speed) and (3) the method used for solving the intercell flux. This can be expressed mathematically for the 1-D system as<sup>126</sup>:

$$\Delta t \leq \frac{\Delta r}{S_{max}} \quad (5.42)$$

Where  $\Delta r$  represents the cell size in the r-direction and  $S_{max}$  is the fastest wave speed present in the computational domain. Hence, the latter parameter needs to be computed in each cell before the size of the next time step is determined. In practice, the time step is computed by introducing the Courant number (also referred in literature as the CFL number).

$$\Delta t = CFL \frac{\Delta r}{S_{max}} \quad (5.43)$$

For inequality (5.42) to be fulfilled the *CFL* number has to be below unity. In the case of the simulations presented in this work, the *CFL* number was chosen to be:  $CFL=0.7$ . In 2-D, Eq. (5.43) is substituted by<sup>126</sup>:

$$\Delta t = CFL \times \min \left( \frac{\Delta r}{S_{max}^r}, \frac{\Delta z}{S_{max}^z} \right) \quad (5.44)$$

And the wave speed is computed at the level of each cell using the following relations:

$$\begin{cases} S_{max}^r = |u| + a \\ S_{max}^z = |v| + a \end{cases} \quad (5.45)$$

Where  $a$  is the speed of sound and  $u$  and  $v$  are the velocities in the r-direction and z-direction respectively. Physically, condition (5.44) says that the size of the time step is computed by taking the minimum between the fastest wave speed propagating in the r-direction and z-direction.

## 5.2.6 Algorithm Steps

The algorithm involves the following steps:

1. Solve the r-split problem by finding the intercell numerical flux using the Roe-Pikes method. To find  $F_{i+\frac{1}{2}}$  the code performs the following tasks:
  - 1.1 Computes the Roe average values  $\tilde{\rho}, \tilde{u}, \tilde{v}, \tilde{a}$  that result from the solution of the linearized Riemann problem (5.34) evaluated at conditions (5.35)
  - 1.2 Computes the eigenvalues  $\tilde{\lambda}_l$  of the Jacobian matrix  $\tilde{A}$  (see Appendix B:)
  - 1.3 Computes the eigenvectors  $\tilde{K}^{(i)}$  of the Jacobian matrix  $\tilde{A}$  (see Appendix B:)
  - 1.4 Computes the wave strengths resulted from the linearized Riemann problem formulated around the average state,  $\tilde{U}$  (see Appendix B:)
  - 1.5 Finds the intercell flux,  $F_{i+\frac{1}{2}}$ , using Eq. (5.33).
2. Integrate in time using Eq. (5.41)
3. Repeat steps 1.1-1.5 to find the intercell flux in the z-direction,  $G_{i+\frac{1}{2}}$ .
4. Integrate the resulting system of ODEs using Eq. (5.41) where the initial condition  $U^{(n)}$  is now the solution of the r-split problem (obtained at step 2).
5. Compute the intercell diffusion flux using Eq. (5.39)
6. Solve the source problem using Eq. (5.37)
7. Advance the solution to the next time step using Eq. (5.41) where the initial condition  $U^{(n)}$  is now the solution of the z-split problem (obtained at step 4).

## 5.3 Test Problems

Before the numerical code is used to simulate the evolution of the laser spark kernel it is paramount that the code is validated against well-established tests problems for which solutions

are already known. The nature of the problem being investigated dictates that a high speed compressible flow problem involving the generation of shocks and rarefaction needs to be used for validating the code. The fluid dynamics of a laser sparks are similar to those generated by an explosion: an excessive amount of energy, concentrated in a very tight space, is being released in a very short time span (almost instantaneously). This transient development gives rise to the formation of a shock wave that carries part of the released energy away from the epicenter of the explosion. Therefore, it seems only reasonable to use a 2-D circular explosion problem that has an analytical solution for testing the ability of the numerical code to solve high speed compressible flows. At later times, the hot gas left at the epicenter of the laser spark develops into a toroidal structure entraining the cold surrounding gas as it cools down. In this cooling phase the thermal conductivity and viscous shear can also play an important. For the purpose of validating the code's ability to simulate these effects an additional unsteady Couette flow is also employed.

### 5.3.1 Spherical Explosion

The spherical explosion problem is an expansion of the Sod's 1-D shock tube problem in a spherical coordinate system<sup>126</sup>. This makes the choice of such a problem as a numerical test for the code very convenient because the results of the simulation can be easily compared against a well-established reference problem. The fluid flow in this conditions is governed by the 2-D Euler's equations written in cylindrical coordinates:

$$U_t + F(U)^a_r + G(U)^a_z = S(U) \quad (5.46)$$

Here  $U$  represents the vector of conservative variables given by (5.2) and  $F(U)^a_r$ ,  $G(U)^a_z$  are the advective fluxes in the r and z-direction (see Eq. (5.3)). The source term,  $S(U)$ , is:

$$S(U) = -\frac{1}{r} \begin{bmatrix} \rho u \\ \rho u^2 \\ \rho uv \\ u(E + p) \end{bmatrix} \quad (5.47)$$

The solution procedure follows the same steps as described in section 5.2.6 with the exception that there is no diffusive flux in this model problem.

The geometry and the initial data shown in Fig. 1 are chosen such that the cylindrical symmetry along the z-axis can be enforced. Moreover, the initial density and pressure profiles are the same as those of Sod's original shock tube problem<sup>138</sup>.

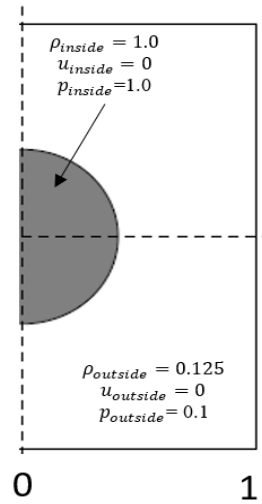


Figure 5.6: Initial conditions for a 2-D spherical explosion with axis-symmetric boundary conditions.

Note that by revolving the initial 2-D profile around the z-axis the problem becomes three-dimensional. For axis-symmetrical problems there is no need to simulate the full 3-D conservation equations. This is not only true for the test problem discussed here but also for the laser spark that is treated in the subsequent sections.

Simulation results are presented in terms of density contours in Figure 5.7 at various time delays. It is important to note that, if the density across the center of the domain is plotted as a

function of radius, one can directly compare the results with the analytical solution. This direct comparison is shown for at a time  $t=0.25$  seconds in the last panel of Figure 5.7.

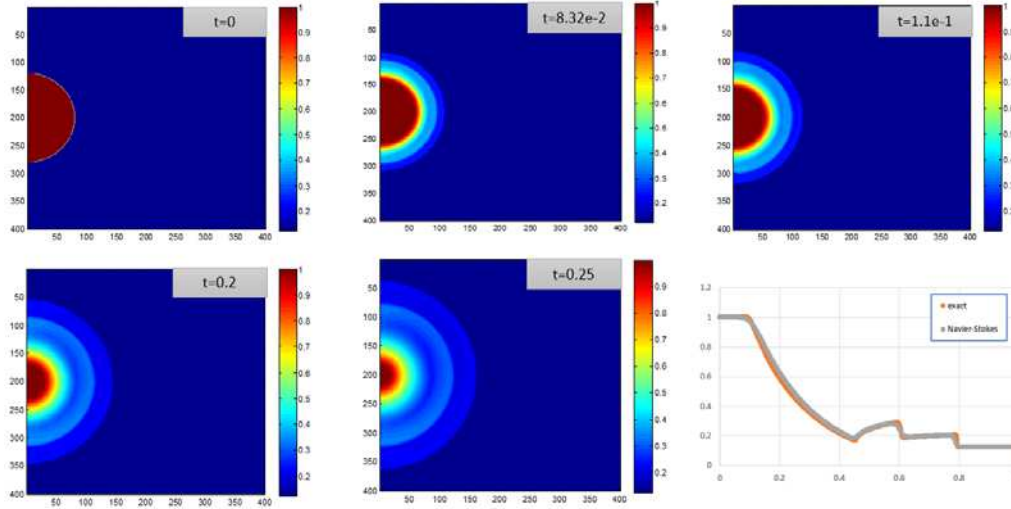


Figure 5.7: Density contours of a spherical explosion test problem. CFL=0.7, Grid resolution was set to  $400 \times 400$ .

A grid sensitivity analysis has also been performed by keeping the CFL number constant and varying the number of cells inside the domain. The plots in Figure 5.8 show how the numerical solution compares with the exact solution for various grid resolutions. A relative error averaged over the entire grid is computed also computed here as:  $\varepsilon_r = \text{abs}[(\rho_{exact} - \rho_{num})/\rho_{exact}]$ . The results, shown in Figure 5.9, indicate that the error follows a normal distribution which demonstrates that the numerical scheme is stable even for a relatively coarse grid size.

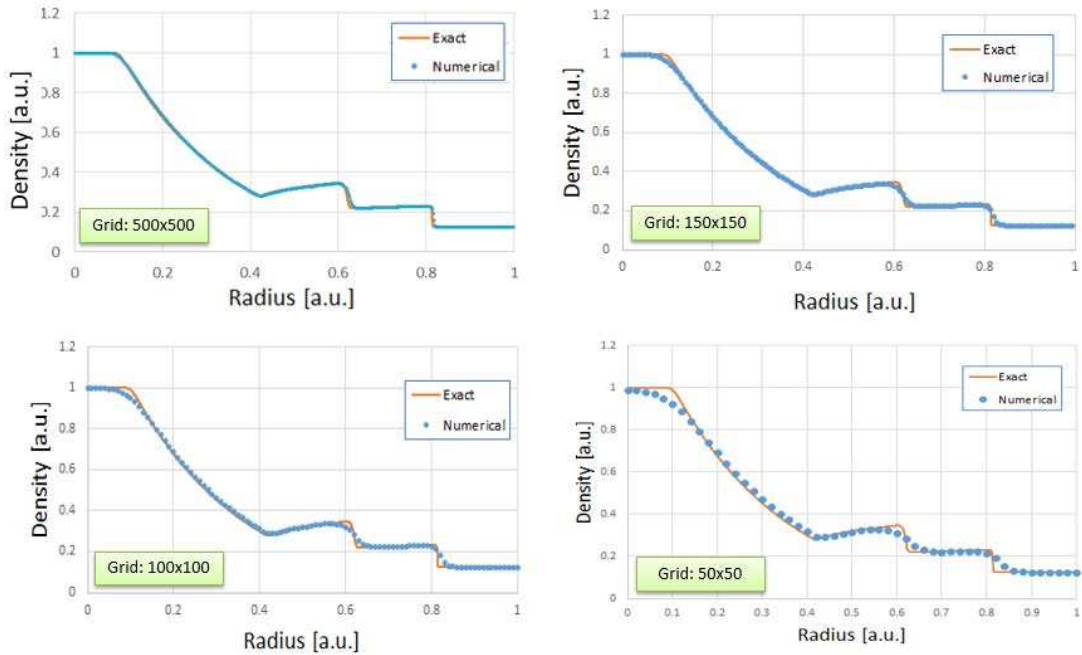


Figure 5.8: Density variation along the radius of a spherical explosion for various grid resolutions.

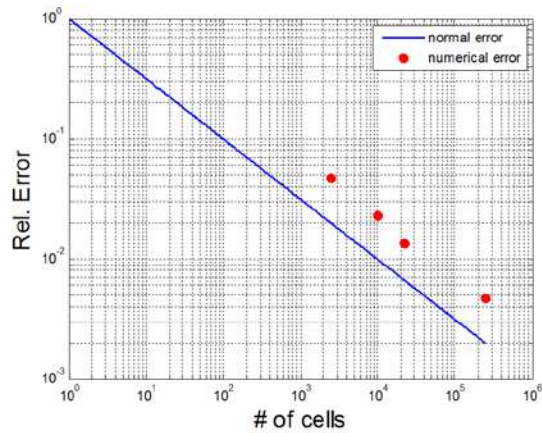


Figure 5.9: Grid sensitivity expressed here in terms of the average relative error.

### 5.3.2 Unsteady Couette Flow

For the explosion problem presented in the previous section, the effects of shear stress and thermal conductivity have been neglected. Another numerical test in which the fluid flow is governed by shear stress is given by the unsteady Couette flow. This problem simulates the flow induced between two infinite parallel plates due to one of the plates translating at a constant

velocity,  $U_{plate}$ . The governing equations (5.1) can be reduced by ignoring any pressure gradients and advective fluxes to the following simplified form:

$$U_t = F(U)^d_x + G(U)^d_y \quad (5.48)$$

with the diffusive flux given by:

$$F(U)^d = \begin{bmatrix} 0 \\ \tau_{xx} \\ \tau_{xy} \\ u\tau_{xx} + v\tau_{xy} \end{bmatrix}; G(U)^d = \begin{bmatrix} 0 \\ \tau_{xy} \\ \tau_{yy} \\ u\tau_{xy} + v\tau_{yy} \end{bmatrix} \quad (5.49)$$

The boundary conditions are no-slip at both walls which implies zero velocity at the lower stationary wall and  $u=U_{plate}$  at the upper moving plate. The domain inlet has zero velocity and there is a zero velocity gradient at the outlet. The velocity in the y-direction, v, is assumed zero everywhere in the domain. A schematic of the problem setup is shown in Figure 5.10.

The Couette problem can be thought as being 1-dimensional in nature. The flow is due to the no-slip condition that forces the fluid next to the translating plate to follow it at the same speed. This generates velocity gradients along the width of the channel formed between the two plates (see Figure 5.10). The unsteady analytical solution of this type of flow is given by Batchelor<sup>139</sup> as:

$$u(y, t) = U_{plate} \frac{y}{h} - \frac{2U_{plate}}{\pi} \sum_{n=1}^{\infty} \frac{1}{n} \exp(-n^2\pi^2vt/h^2) \sin \left[ 1 - \frac{y}{h} \right] \quad (5.50)$$

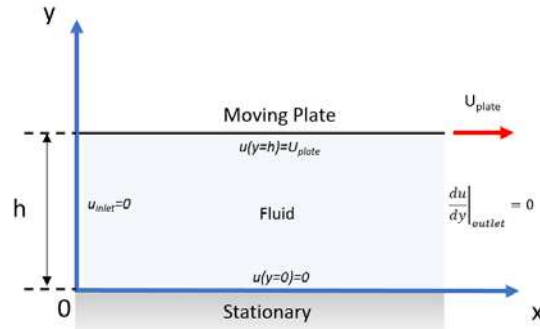


Figure 5.10: Schematic of a Couette Flow showing the Boundary Conditions used in the numerical code.

A comparison between the analytical solution (5.50) and the numerical solution is plotted in Figure 5.11. In reality, the Couette solution cannot be attained instantaneously. The time required to reach a steady state depends on the width of the channel created between the two plates and the kinematic viscosity of the fluid. Note, however, that it does not actually depend on the speed of the moving plate. As shown in Figure 5.11, the steady state solution is reached when

$$\frac{\nu t}{h^2} \sim 0.5.$$

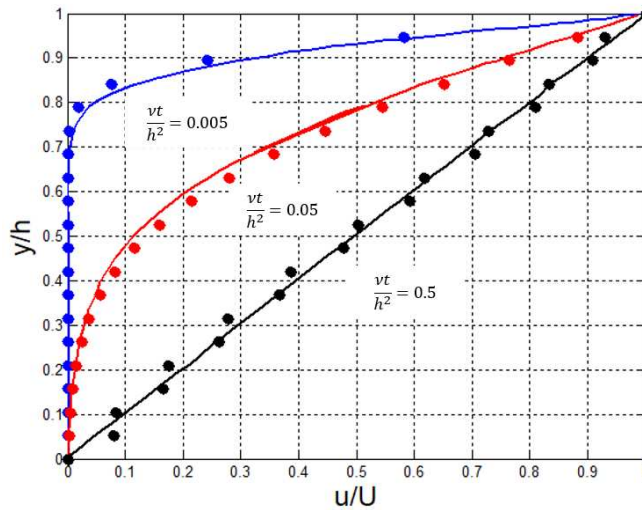


Figure 5.11: Unsteady Couette Solution at various time delays. The exact solution is shown with solid line and the numerical solution with discrete dots.

## 5.4 Study of Spark Induced Hydrodynamics

This section focuses on the CFD modeling of the dual-pulse laser energy deposition into a pure nitrogen gas. There are two scenarios under investigation: (1) the dual-pulse energy deposition is uniform along the laser beam. This case corresponds to the experimental observation presented in Figure 4.10-center where no third lobe is being observed. From here on we will call this the symmetric kernel case. (2) the energy deposition is not uniform with the NIR pulse being focused slightly in front or after the UV pulse (representative of the results shown in Figure 4.10-left or Figure 4.10-right). This will be referred as the asymmetric case. The investigation is conducted using the custom code developed at Colorado State University during the research conducted for this dissertation. The goal is to understand which configuration is more advantageous to stimulate the early flame kernel development. An ideal configuration would have a reduced vorticity and would limit the heat and radical advection from the kernel to the surroundings while at the same time keep the kernel temperature hotter for an extended time interval.

### 5.4.1 Problem Setup

The initial shape and dimensions of the hot kernel induced by the dual-pulse are determined by visual inspection of the Schlieren images obtained experimentally. An example image is shown in Figure 5.12 for the case in which the NIR pulse is focused slightly in front of the UV pulse. The image shows that the shape of the plasma kernel contains two features: an elongated channel formed by the UV pre-ionization beam and a spherical plasma growth overlapped on the channel that is due to the addition of the NIR pulse. Not shown here is the case when the two pulses are perfectly overlapped. Nonetheless, in that case, one would expect that the spherical plasma induced by the NIR to be centered on the UV pre-ionization channel.

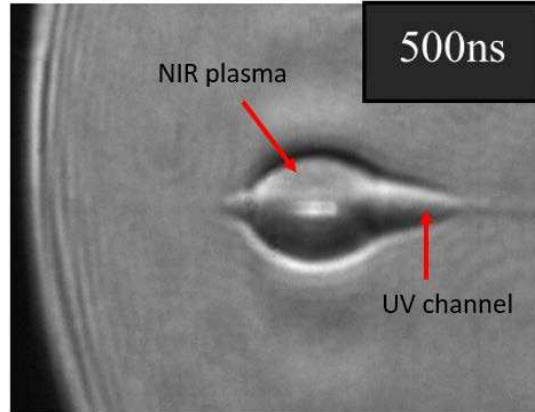


Figure 5.12: Schlieren image of a dual-pulse laser plasma in atmospheric air at 500 ns after the pulse. Image shows the channel generated by the UV plasma and the spherical plasma growth induced by the addition of the NIR.

Obtaining the initial temperature and pressure of the plasma experimentally is extremely challenging and satisfactory results have yet to be reported in literature. This makes the choice of the initial conditions for the simulation somewhat difficult. Several CFD studies of laser sparks report have used an initial temperature anywhere between 10,000 K and 50,000 K and an initial pressure on the order of a few hundred bar. They all show good agreement with experimental results in terms of the development of the third lobe<sup>63,140</sup>. Ghosh and Mahesh conducted a parametric study on the initial temperature and found that a higher initial plasma temperature leads to stronger gradients in the pressure field at the early time (and stronger shocks)<sup>65</sup>. However, they did not observe significant changes in the development of the third lobe as the initial temperature is varied. An alternative method for fixing the initial conditions is to use the Taylor-Sedov blast wave theory to fit the experimental data<sup>141,142</sup>. The theory establishes a relationship between the radius of the shock wave, the time of propagation and the instantaneous energy deposition inside the kernel. Once a relationship between the shock speed and the energy deposition is known, the pressure and temperature at the shock front can be determined using the Rankine-Hugoniot relationships. This method, however, does not give satisfactory results for predicting the pressure

and temperatures at the earliest times. Bradley et al. report a temperature on the order of 150,000 K and pressure in excess of 3,000 bar at 15 ns after the laser spark using the blast wave theory<sup>26</sup>. Even if this values were to be assumed correct, there are no transport data available at this conditions to perform a numerical simulation. In reality, an accurate prediction of initial conditions after the laser pulse requires the modeling of the plasma physics and this is beyond on the scope of the current investigation. For the simulations conducted here the initial peak temperature and peak pressure were estimated to:  $T_{\max_0} = 3.5 \times 10^4 K$  and  $P_{\max_0} = 2.2 \times 10^7 Pa$  based on previous research on laser sparks. Additionally, temperature of the surrounding gas is set to 300 K and the pressure to  $1.01 \times 10^5 Pa$ . The same initial conditions were used for both test cases because it was experimentally determined that the energy absorbed inside the gas was similar, irrespective of the overlap between the two pulses (see Figure 4.11). The initial temperature and pressure profiles are presented in Figure 5.13 for the case in which the two pulses have the same waist and in Figure 5.14 for the case in which the NIR pulse is focused in front of the UV pulse. The initial shape was obtained by superimposing an ellipse over a rectangular shape and the gradients were generated using a Gaussian filter. The spark length is 2 mm and the minor radius of the elliptical part is 0.5 mm giving an aspect ratio  $AR=2$  for the initial kernel, similar to what was observed experimentally through Schlieren images.

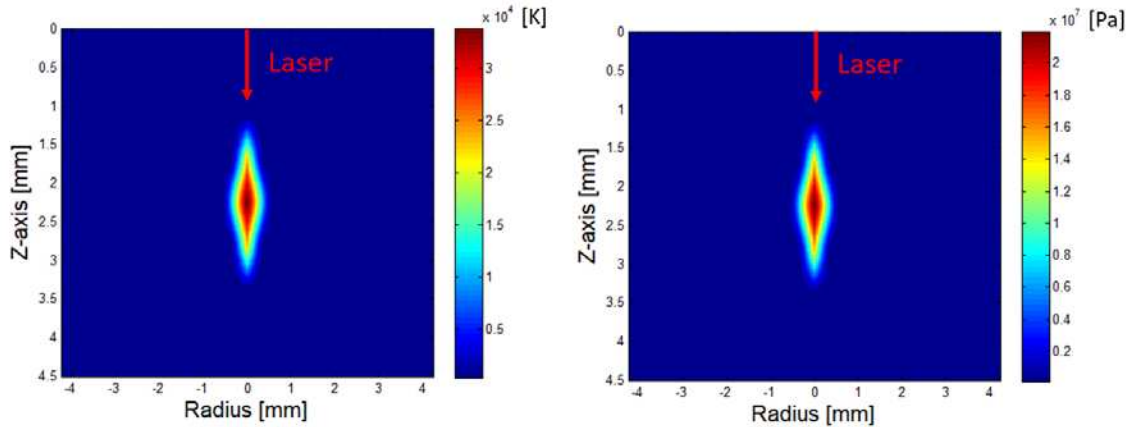


Figure 5.13: Initial temperature (left) and pressure (right) profiles for the symmetric hot kernel generated by the dual-pulse.

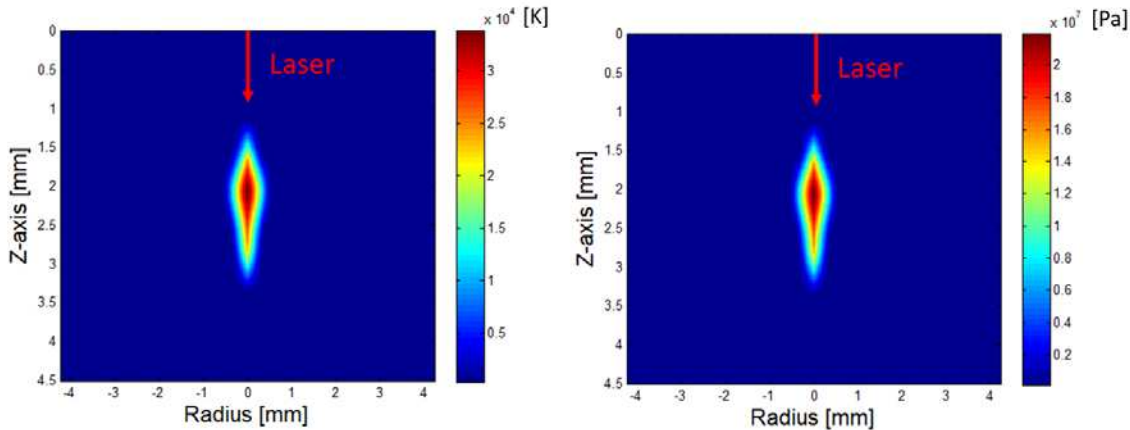


Figure 5.14: Initial temperature (left) and pressure (right) profiles for the asymmetric hot kernel generated by the dual-pulse.

The governing equations are solved on a structured Cartesian grid using the control volume discretization approach described previously. A piece-wise distribution of initial data over the computational cells is employed where the value at the center of a cell represents the average of each variable over the cell (see Section 5.2 for more details). An optimum cell resolution is required in order to resolve the phenomenon of interest while minimizing the computational requirements. The experimental results indicate that kernel evolution takes place over two timescales suggesting that two different cell sizes can be used in the simulation. In the first 20  $\mu$ s

the kernel grows significantly, the temperature drops by more than half of its initial value and vorticity is generated by the interaction of the rarefaction waves with the hot gas. Over this time interval, an optimum cell size of 15 microns was determined through a grid sensitivity analysis. At times greater than  $t > 20 \mu s$ , it was established reasonable to double the cell size to 30 microns in order to save computational time since the gradients of pressure and temperature are much weaker and the toroidal structure observed experimentally has already formed.

The grid size is reduced by taking advantage of the axial symmetry of the two kernels under investigation as mentioned in section 5.2. Additionally, when waists of the UV and NIR pulses are overlapped, the kernel is also symmetric over the radial axis. This means that only a quarter of the kernel needs to be considered in the simulation for this problem. On the other hand, when the NIR pulse is focused in front of the UV pulse, half of the kernel is simulated. The mesh size at the start of the simulation along with the boundary conditions are shown in Figure 5.15. The z-axis in both cases denotes the optical axis of symmetry (A). In reality, axisymmetry is not a boundary condition because there is no boundary in the azimuthal direction. The axisymmetry condition is simply used to simplify the conservation laws in Eq. (4.1). Therefore, axisymmetry it is already contained in the model equations. To determine the appropriate physical value for a particular variable at a point on the boundary (A), the code uses the values from the adjacent cells. (B') is prescribed as a symmetry boundary condition by making all of the gradients normal to the r-axis equal to zero. Physically this corresponds to a mirroring of the profile around (B'). Note that symmetry and axisymmetric conditions are not the same thing. They model different physical phenomena. The remaining boundaries (B), (C) and (D) in Figure 5.15 are held constant to the ambient conditions ( $T_0 = 300 K, p_0 = 1.01 \times 10^5 Pa$ ).

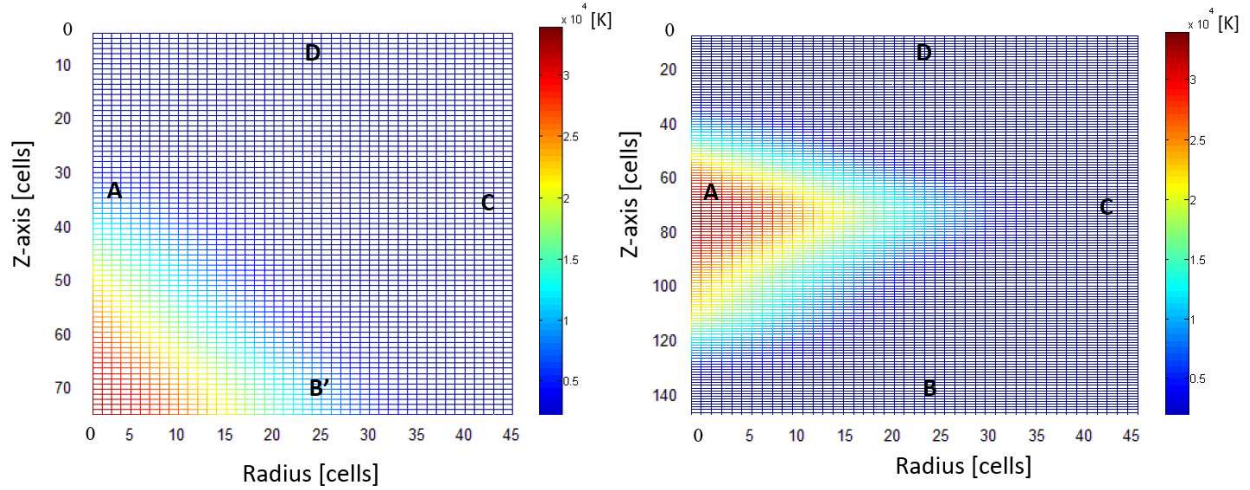


Figure 5.15: Initial mesh size for the symmetric (left) and asymmetric (right) kernels. Boundary A is the axis of symmetry for both kernels, B' is boundary of symmetry and C, D are prescribed the ambient condition.

The code developed in this dissertation uses a dynamic domain size which further reduces the computational cost. Initially, the domain is only slightly larger than the kernel itself as seen in Figure 5.15. However, as the kernel grows in time and the shock wave starts to develop, the domain size is increased by adding computational cells at the edges of the boundary. Once the pressure behind the shock returns to ambient conditions, the domain is shrunk back to dismiss the presence of the shock and the focus is solely on the evolution of the hot gas kernel that is left behind at the epicenter.

### 5.4.2 Shock Wave Propagation

The simulation starts after the laser energy deposition has ended. At early times, the kernel pressure decay dominates the initial fluid dynamics. Since the laser energy is deposited inside the gas on a much smaller timescale (nanoseconds) compared to the hydrodynamics scale of the gas mixture, pressure waves created during the energy addition process tend to coalesce into a shock wave at the surface of the kernel. Around ~500 nanoseconds after the end of the dual-pulse, the shockwave detaches itself from the kernel and starts propagating outward dissipating the excess

energy of blast. As shown in Figure 5.16, initially the shock wave takes the shape of the kernel. However, as time progresses, the shock wave becomes more spherical reaching an almost spherical front  $\sim 20 \mu s$ . This is valid for both kernels under investigation and it shows that, independent of the initial shape of the plasma, the non-uniform acceleration generated by the pressure gradients ultimately leads to the development of a spherical shock. The phenomena is visible when taking a closer look at the pressure contours in Figure 5.16. The aspect ratio of the plasma is such that the kernel twice as long over the optical axis than radially. However, at early times ( $t \sim 0.5-2 \mu s$ ) the pressure gradient is stronger over the radial direction. This leads to more acceleration in this direction and, as time progresses, the shock “catches up” becoming spherical. An intuitive explanation of the phenomenon is provided with the aid of Figure 5.17 below. If one imagines a cylindrical kernel oriented such that its height corresponds to the z-axis, the ensuing shock wave can be thought of as a superposition of a spherical front at the leading and trailing edge and a planar shock wave on the lateral sides of the cylinder. Initially, the pressure field is uniform across the shock. However, as the cylindrical shock propagates, the spherical shock losses energy quicker than the planar counterpart because it is stretched over a larger area (increasing its radius) as time progresses. This makes the pressure gradients (and the acceleration) smaller over the z-axis than radially. Ultimately, this will make the shock spherical in shape as it observed in the two tests cases investigated here.

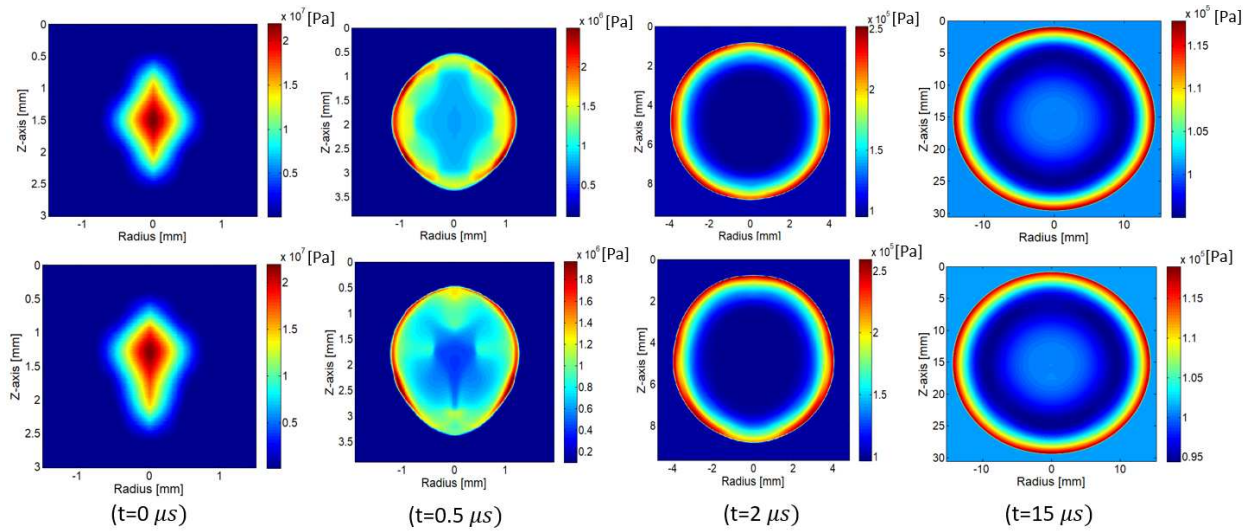


Figure 5.16: Pressure contours shown the evolution of the shock wave for the symmetric (top) and asymmetric (bottom) kernel. Note that the r-axis is stretched compared to the z-axis in all the plots.

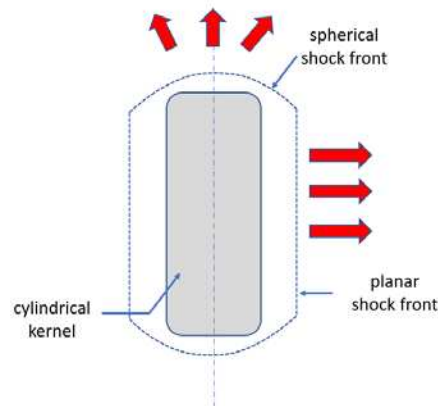


Figure 5.17: Schematic explaining the dynamics of shock wave development for non-spherical bodies

As the shock waves propagate outward the pressure in the center of the domain starts to decrease towards ambient conditions. Interestingly, the pressure goes below atmospheric at  $\sim 2 \mu\text{s}$  after the pulse with a minimum pressure value of  $\sim 7.92 \times 10^4 \text{ Pa}$  at a time delay of  $\sim 4 \mu\text{s}$  (see Figure 5.18). This represents the moment of kernel collapse and it is at this stage that the development of the toroidal shape starts to take place. At  $\sim 15 \mu\text{s}$  the pressure at the center returns back to normal. After this point the pressure itself does no longer play an important role in the

dynamics of the hot gas left at the center of domain. A close inspection of Figure 5.18 reveals that there is an inflection point in the pressure decay rate  $\sim 500$  ns after the pulse. This change in pressure decay trend is consistent with the moment of shock wave detachment from the kernel. Moreover, the trend is almost identical for both types of kernel.

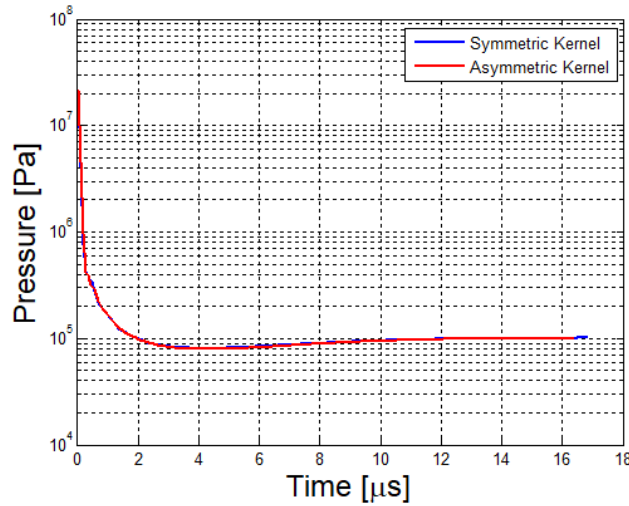


Figure 5.18: Time history of the pressure evolution at the center of the domain

### 5.4.3 Kernel Dynamics

Displayed in Figure 5.19 are temperature profiles showing the time evolution of the simulated dual-pulse kernel in the two cases investigated: symmetric kernel – energy of the NIR pulse is placed at the center of the UV channel and asymmetric kernel – energy of the NIR pulse is deposited with an offset with respect to the UV plasma (in this case, NIR focus is displaced towards the laser). It is interesting to note that, while the shock wave development was nearly identical in both cases, the kernel dynamics are distinctly different for each case. During the first  $5 \mu s$  the kernel expands very quickly while both temperature and pressure decay. The kernels are observed to double their initial size during this time period. In both cases the plasma collapse takes place  $\sim 3-5 \mu s$ . The subsequent evolution of the two kernels take different paths after this point.

The symmetric kernel starts to grow significantly over the radial direction as it collapses over the optical axis. At  $\sim 50 \mu\text{s}$  the kernel has the shape of a perfectly symmetrical toroid. As time evolves, fluid from the center region is being advected outwards and the toroid increases its dimensions and gradually cools down. On the other hand, in the case of the asymmetric kernel, the collapse induces a fluid flow along the optical axis propagating towards the laser (or towards the point where the temperature is the highest). As time progresses, the kernel evolves into an asymmetric torus in which the fluid from the outside is entrained and pushed along the optical axis towards the laser source. This leads to the rapid cooling of the kernel epicenter and the formation of a third lobe. The results presented in Figure 5.19 also confirm the idea advanced in Chapter 4, section 4.4, that the formation of the third lobe depends strongly on how the energy is deposited along the axis of the kernel. If the NIR pulse is focused in front of the UV pulse, then the third lobe propagates towards the laser beam. Alternatively, if the two focal points are perfectly overlapped, the formation of a third lobe is suppressed. Due to symmetry, we have also indirectly shown that if the NIR pulse is focused behind the UV pulse then the third lobe will reverse direction and propagate away from the laser source. Another important aspect, with possible consequences for ignition, is that the temperature of the kernel decays much faster if there is an offset between the two pulses. For example, at  $t = 50 \mu\text{s}$ , the maximum temperature is  $\sim 6,500 \text{ K}$  for the symmetric kernel and only  $\sim 3,600 \text{ K}$  for the asymmetric kernel.

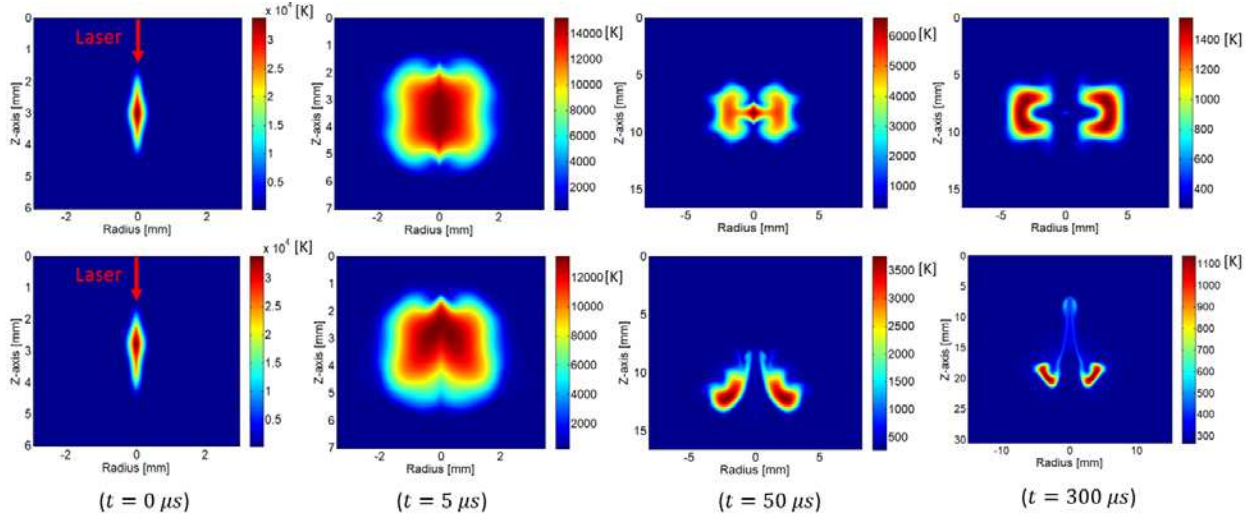


Figure 5.19: Temperature contours showing the kernel evolution for the symmetric (top) and asymmetric (bottom) kernels

In order to better understand the kernel dynamics it is important to look at the velocity field for both test cases. Initial vorticity is generated very early during the kernel development. For example, the velocity field of the symmetric kernel at  $t = 1.5 \mu s$  is already distorted due to the presence of vorticity at the leading and trailing edge (see Figure 5.20-left). The presence of eddies at this moment in time is surprising as one would have intuitively expected that vorticity is induced in the flow during the kernel collapse phase which takes place several microseconds later. The source of flow rotation is revealed by inspecting the vorticity equation. Taking the curl of the momentum equation<sup>143</sup>:

$$\frac{D\vec{\omega}}{Dt} = (\vec{\omega} \cdot \vec{\nabla})\vec{u} - \vec{\omega}(\vec{\nabla} \cdot \vec{u}) + \frac{1}{\rho^2} [\vec{\nabla}p \times \vec{\nabla}\rho] + v\vec{\nabla}^2\vec{\omega} \quad (5.51)$$

The first term on the right-hand side describes enhancement of vorticity by stretching and is the mechanism through which turbulent eddies transfer energy to smaller scales. The flow considered here is not turbulent and this term is not very important for the problem under investigation. The physical interpretation of the divergence of velocity in the second term is that of a volumetric expansion. In this context, the second term shows that vorticity decreases as the

fluid expands (due to the negative sign). This mechanism of vorticity generation is important during the kernel collapse at later times. However, at this early stage, the kernel is expanding so this term does not contribute to vorticity generation. The last term in Eq. (5.51) describes the effects of viscous diffusion on vorticity generation. However, the contribution of diffusive fluxes at this time delay is minimal the flow being primarily dominated by the advective fluxes (compressible inviscid). This leaves us with the third term which describes vorticity generated by a baroclinic instability in the flow. Physically this is manifested through a misalignment between the density and pressure gradients that induces baroclinic torque. Indeed, if the pressure and density gradients are plotted in the region where flow vorticity is observed it becomes apparent that the pressure and density gradients are misaligned (see Figure 5.20-right). If the same gradients are plotted in a region where there is no flow rotation, one notices that they overlap perfectly as expected. It is interesting to contemplate the reason why baroclinicity is present in the flow induced by the dual-pulse laser plasma. One speculative idea is that it is in fact induced due to the aspherical nature of the initial kernel. Following the same arguments as presented previously in Figure 5.17 the pressure field will be stronger in the radial direction than along the optical axis (due to the cylindrical geometry of the kernel). This will slightly tilt the pressure gradient with respect to the density gradient. At the same time, the density gradient is heavily influenced by the kernel temperature which is homogeneously distributed along the kernel. The two effects combined lead to the generation of vorticity through the mechanism of baroclinic torque.

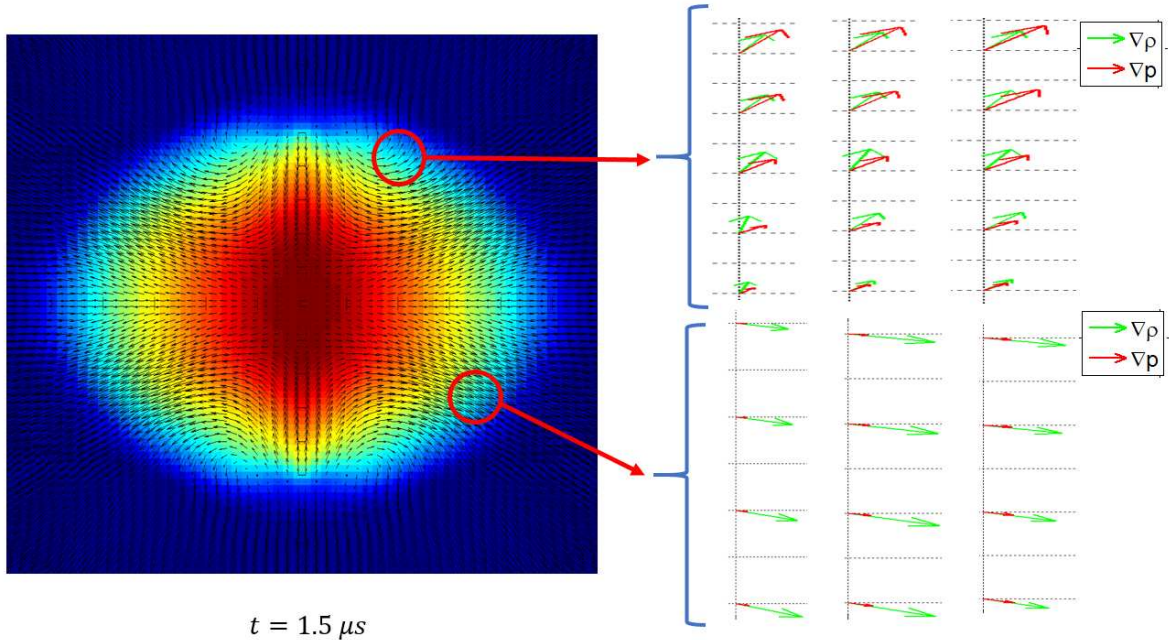
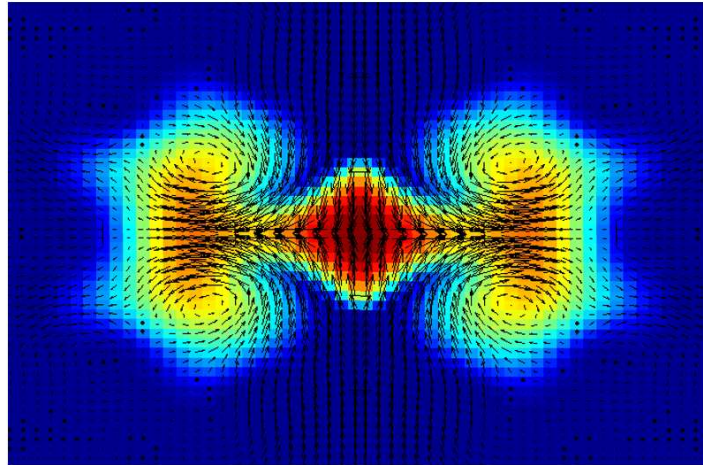


Figure 5.20: (Left) Velocity field overlaid on top of temperature contours for the symmetric kernel at a delay of  $1.5 \mu s$  after the two pulses. (Right) Zoomed-in inserts showing the misalignment of the density and pressure gradients which leads to the formation of a barotropic instability.

After plasma collapse ( $t < 5 \mu s$ ), the second term in Eq. (5.51) is expected to enhance the flow vorticity due to the kernel compression under the action of a negative pressure gradient directed towards the center. Physically, the negative pressure gradient is caused by the passage of a rarefaction wave that accompanies the shock propagation. This leads to a mean flow directed towards the epicenter of the hot gas kernel. The lower density fluid will be accelerated more by this pressure gradient than the fluid at high density leading to further generation of vorticity inside the kernel. It is posited that this mechanism is the primary responsible for the formation of the toroidal shape observed in Figure 5.21 at a time delay of  $50 \mu s$ . Note that the symmetric structure of the kernel in the case when the UV and NIR pulses are perfectly overlapped lead to the formation of a stagnation plane at the center of the gas kernel. This explains why the temperature in this configuration decays slower than when there is an offset between the two laser pulses (the asymmetric case).



$t = 50 \mu s$

Figure 5.21: Velocity field overlaid on temperature contours for the symmetric kernel at  $50 \mu s$  delay. This shows the development of two counter-rotating vortices inside the toroid.

The mechanism of vorticity generation for the asymmetric kernel is very similar to the one described above for the symmetric case: baroclinic torque at early stage followed by additional vorticity at later times due to the interaction between the rarefaction wave and the hot gas. A related mechanism was reported by Ghosh et al while studying single-pulse laser generated sparks<sup>65</sup>. The velocity contours are shown in Figure 5.23 for the two distinct moments in the evolution of the kernel. Initially, vorticity is being generated both at the leading and trailing edge of the kernel (much like in the case of the symmetric kernel). However, the offset between the center of the channel and the epicenter of the shock seen in Figure 5.22 makes the vorticity more persistent at the trailing edge of the kernel.

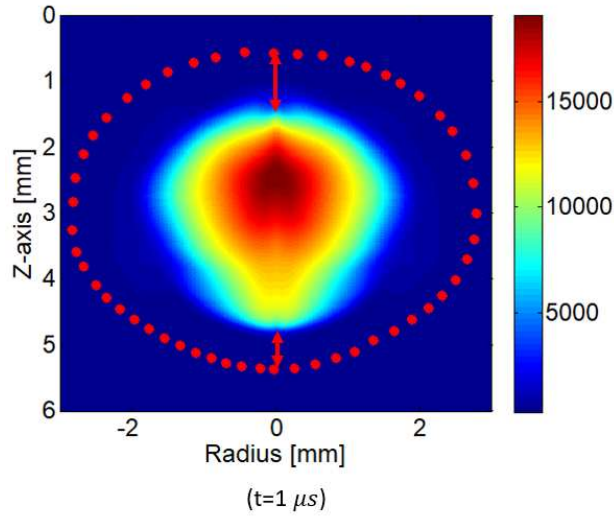


Figure 5.22: Temperature contours of the symmetric kernel at 1 microsecond after the dual-pulse. Also shown in this figure is the position of the shock wave. Note that the trailing edge of the shock wave is much closer to the kernel than the leading edge.

This imbalance preferentially entrains the outer fluid from the trailing edge and pushes it through the center of the toroid giving rise to the formation of a third lobe propagating towards the laser source as seen in Figure 5.23. It is important to note that, since the energy is not deposited uniformly along the optical axis there is no stagnation plane at the center of the kernel anymore.

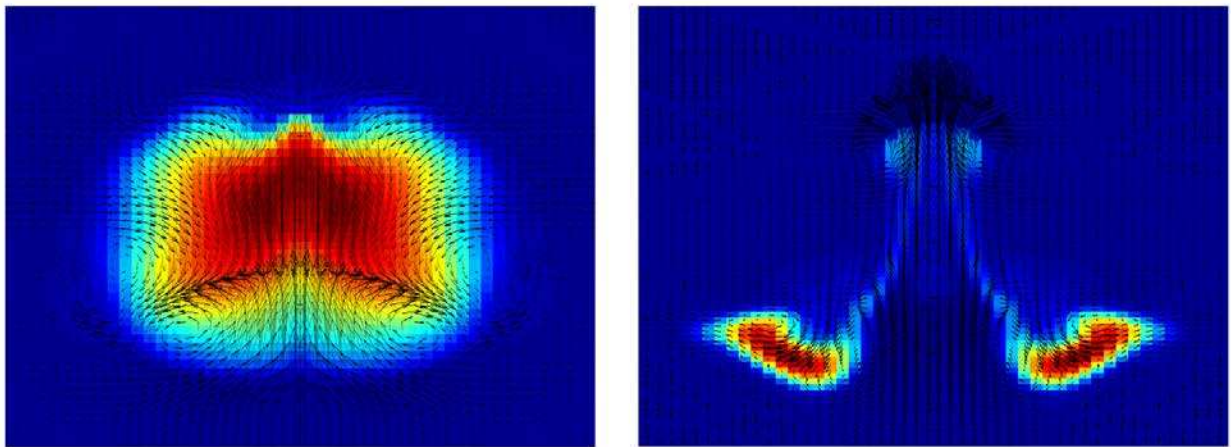


Figure 5.23: (a) Velocity field of asymmetric dual-pulse kernel at  $5 \mu s$  and (b) at  $300 \mu s$ .

#### 5.4.4 Comparison with experiments

For the case of the dual-pulse kernel in which energy is deposited homogeneously along the optical axis an experimental comparison can be made with the gas breakdown between two pin electrodes. The images from Figure 5.24 provide a qualitative comparison between the synthetic Schlieren images obtained in the current study and experimentally generated Schlieren of a spark generated between the gap of two pin electrodes (taken from Kono et al.<sup>67</sup>). The time scales are very different with the experimental kernel developing much quicker. This is probably due to the presence of the electrodes which act as a heat sink for the hot kernel and confine the geometry of the flow (therefore forcing the earl. Additionally, the electrodes confine the geometry of the flow which would lead to a much earlier kernel collapse and plasma core roll up. However, certain features are very similar despite the different configuration (and physics) involved in the breakdown process thus confirming that the thermal/fluid dynamics processes governing the late kernel development depend primarily on the way energy is deposited into the gas. The symmetrical plasma collapse and the radial growth of the kernel is shown in both cases at  $\sim 20\text{-}30 \mu\text{s}$  with the simulation kernel taking somewhat longer to develop. It is interesting to note in both cases the formation of a groove inside the toroidal ring at later times. Kono et al. note in their study that the presence of the groove is highly dependent on the aspect ratio of the initial plasma channel. In the experimental case the aspect ratio is  $AR \sim 2.5$ , being dictated by the diameter of the electrodes and the distance between them. The aspect ratio of the simulated spark is similar ( $AR \sim 2$ ).

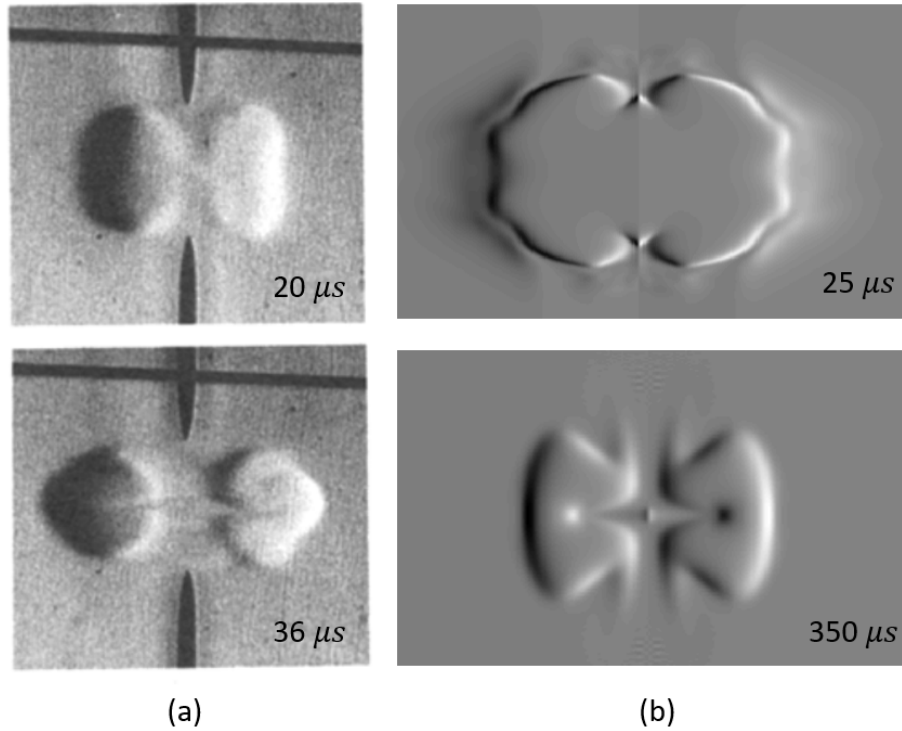


Figure 5.24: (a) Schlieren images depicting the evolution of a plasma kernel between two electrodes and (b) synthetic Schlieren images showing similar dynamics for the hot kernel generated by the dual-pulse symmetric case. Experimental Schlieren is from Kono et al.<sup>67</sup>

Schlieren images of the asymmetric plasma kernels generated using the dual-pulse have been obtained in our lab. A comparison between the experimentally obtained kernels and the model is presented in Figure 5.25. In both cases the laser beam propagates from left to right with the NIR beam being focused slightly in front of the UV pulse. The kernel dynamics predicted by the model is seen to agree very well with experimental observation. At 30 μs after the two pulses, there is a noticeable larger indentation into the plasma core at the trailing edge than at the leading edge due to preferential vorticity along the optical axis. This represents the beginning of third lobe development. At later times, the asymmetric toroidal shape with the third lobe propagating towards the laser source is observed. The Schlieren images also make it visible that the hottest part of the kernel has moved away from the center of the initial plasma.

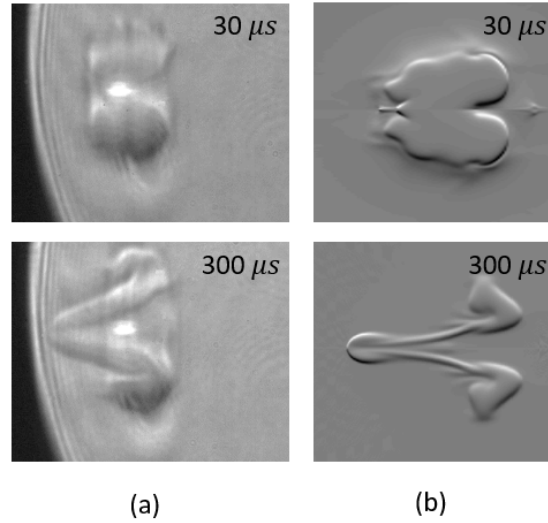


Figure 5.25: (a) Experimentally obtained Schlieren images showing the collapse of the plasma kernel and the formation of the third lobe. (b) Synthetic Schlieren images showing very similar dynamics.

#### 5.4.5 Implications for Laser Ignition

The numerical results presented in the previous section gives an idea on how the two different kernels will influence the early flame development. As observed experimentally in Chapter 4, the impact of the different kernel geometry on ignition can be significant near the lean limit. Based on the numerical analysis conducted here one would expect that the perfect overlap of the two beams would be more beneficial to ignition applications. The temperature of this type of kernel stays high for a longer period of time due to the presence of the stagnation plane at the center of the kernel. Additionally, the recirculation induced by the symmetric toroidal shape could reduce the diffusion of radicals through the third lobe which will greatly benefit ignition. Near the lean limit, the lower flame stretching induced by this kernel geometry could also be beneficial. The asymmetric kernel dynamics developed in a similar manner as a typical single-pulse laser ignition kernel with the formation of third lobe propagating towards the laser source. As shown in Chapter 4, this type of kernel geometry can lead to high rates of flame stretch and extinction near the lean flammability limit.

## CHAPTER 6:

### Conclusions

The objective of this dissertation was to present a new laser ignition technique based on a dual-pulse pre-ionization scheme that addresses some of the common issues associated with laser ignition (high energy requirements, increased flame stretching, no control over the plasma parameters). The topic was treated from the point of view of the physics of plasma involved at various laser wavelengths (Chapter 3) as well as the combustion perspective (Chapter 4). In Chapter 6 a numerical code was developed in order to understand the impact of the plasma induced flow on the flame dynamics. The conclusions drawn from Chapters 3,4 and 5 are summarized in the next section. This chapter concludes with the presentation of future research directions and new potential applications of the technique developed in this dissertation are proposed.

#### 6.1 Summary

Chapter 3 provides an analysis of the threshold characteristics of the ultraviolet and near-infrared laser induced plasma. The present contribution compares the energy absorption, optical emission, temperature and fluid dynamics of ultraviolet (UV)  $\lambda=266$  nm and near infrared (NIR)  $\lambda=1064$  nm nanosecond laser induced plasmas in ambient air. For UV pulses at the conditions studied, energy absorption by the plasmas increases relatively gradually with laser pulse energy starting at delivered energy of  $E \sim 8$  mJ. Corresponding measurements of plasma luminosity show that the absorption of UV radiation does not necessarily result in visible plasma emission. For the NIR induced plasmas, the energy absorption profile is far more abrupt and begins at  $\sim 55$  mJ. In contrast with UV, the absorption of NIR radiation is always accompanied by intense optical

emission. The temperatures of both types of plasma have been measured with Rayleigh scattering thermometry (at times after the Thomson signal sufficiently diminishes). The UV plasmas can attain a wider range of temperatures, including lower temperatures, depending on the pulse energy (e.g.  $T \sim 400-2000$  K for  $E \sim 7-35$  mJ at  $\Delta t = 10$   $\mu$ s after the pulse) while the NIR plasmas show only hotter temperatures (e.g.  $T \sim 12,000$  K for  $E = 75$  mJ at  $\Delta t = 10$   $\mu$ s after the pulse) as is consistent with the literature. Differences in the fluid dynamics for UV versus NIR pulses are shown with Schlieren imaging. The contrast in the UV and NIR plasma threshold behavior are attributed to differing roles of avalanche ionization and multiphoton ionization as is also illustrated by a simple numerical model. The present study addresses the mechanisms governing laser plasma formation with UV and NIR nanosecond pulses. Laser energy absorption for 266 nm pulses takes place at much lower energies than for 1064 nm due to the higher influence of MPI and possible N<sub>2</sub> REMPI contributions. The influence of pressure on the NIR energy absorption is higher in agreement with a larger role of electron avalanche ionization (under cascade ionization theory). The new finding is that the UV absorbed energy (and ionization and luminosity) varies continuously with laser energy, while for the NIR pulses the absorbed energy tends to “jump” between zero and elevated values. The continuous increase in UV ionization with pulse energy points to an inconsistency in the traditional use of the term “breakdown threshold” in this spectral region, while the more step-like behavior at NIR is more amenable to a threshold description. Both UV and NIR plasma show a stochastic behavior. The development of a simple numeric model of the plasma growth at various wavelengths provides consistent results in terms of the increased role of MPI for UV and the dominant role of EAI for NIR. The ability to generate UV plasmas with varying energy content, temperature, and ionization can open the door for tailored laser induced plasmas with desired. For

example, in combustion applications, this would enable the generation of a somewhat cold plasma ( $T \sim 2,000\text{--}3,000\text{ K}$ ) with low degree of ionization.

In chapter 4 the dual-pulse pre-ionization technique using UV and NIR pulses is demonstrated for ignition of propane-air mixtures at various equivalence ratios. A comparative study between the well-established laser spark ignition and dual-pulse is presented. The results indicate that using the dual-pulse technique leads to a reduction of the lean limit for propane-air mixture and an increase in combustion efficiency. Additionally, the energy required for ignition for the dual-pulse method is lower ( $E=60\text{ mJ}$ ) compared to the NIR laser spark ignition ( $E=75\text{ mJ}$ ). A detailed study of the differing flame dynamics was also conducted using  $\text{OH}^*$  chemiluminescence imaging. It is shown that the flame kernel develops as a toroidal structure that is governed by the fluid mechanics induced during the plasma recombination process. For lean mixtures the third lobe (that points towards the laser beam) breaks from the main toroidal flame structure with negative effects on flame development. For the dual-pulse method, it is shown that the flame dynamics can be controlled by adjusting the axial offset of the UV and NIR beams resulting in reversal or elimination of the third lobe. Finally, it is suggested that the third lobe has important consequences on the early flame growth and extinction.

A computational fluid dynamics (CFD) study describing the evolution of the laser spark kernel is presented in Chapter 5. The model simulates the energy deposited by the laser in the gas mixture neglecting plasma kinetics and changes to the gas composition. Nonetheless, a comparison with experimental results shows that the CFD simulation provides a realistic image of the flow field induced by the laser spark. Two different cases are simulated for laser plasma induced using the dual-pulse pre-ionization scheme. When the two beams are perfectly overlapped the energy deposition is homogeneously distributed around the beam waist. This leads to the generation of a

symmetrical toroidal structure with a stagnation plane present at the center of the hot kernel. It is posited that this configuration has a positive impact on ignition because the temperature at the center of the kernel stays high for a longer period than for typical single-pulse laser sparks. Additionally, the vorticity generated inside the kernel is smaller for this configuration which leads to a reduction in early kernel stretching. This has the effect of reducing the possibility of flame kernel separation (a scenario that was observed experimentally in Chapter 4 under certain conditions). A different test case investigated here corresponds to an asymmetric kernel formed when the focal points of the two pulses are matched along the optical axis. As the kernel cools down this asymmetric (in the r-direction) energy deposition leads to the formation of a 3-lobe structure that is similar to the one reported in literature for single pulse laser spark ignition. When compared to the fluid dynamics induced by the symmetric kernel there are certain disadvantages to this configuration. The presence of the third lobe means that important radicals formed inside the toroid can be advected away from the hot region of the kernel through the third lobe. Additionally, the temperature decays much faster in the 3-lobe configuration and the vorticity is higher. This could negatively impact the early development of the flame kernel.

## **6.2 Future Work**

### **6.2.1 Dual-Pulse Pre-ionization for Laser Ignition**

The dual-pulse pre-ionization scheme in its current implementation has shown promising potential for laser ignition applications as presented in Chapters 3-6. However, this method is not optimized yet and more work is needed for the technique to reach its full potential. The dual-pulse technique presented here still requires a high degree of ionization ( $n_e \sim 10^{16} - 10^{17} \text{ cm}^{-3}$ ). As presented in Chapter 3, the UV pulse can generate a very low degree of ionization in the gas that is only visible using the intensified camera. Ideally, the NIR pulse will only add energy into the pre-

ionized gas without increasing the plasma density. This could not be achieved in the current configuration and should be investigated further. One idea is to increase the waist size of the NIR pulse to be greater than that of the UV pulse. This way, the peak intensity of the energy addition beam will be lower and the chances of breakdown inside of the pre-ionization channel will decrease. Moreover, an investigation of the optimum focusing conditions for the two pulses will also allow us to better understand the effects of beam defocusing for the NIR pulse. The UV generated plasma changes the index of refraction of the medium at the location of the beam waist. This would, in principle, change the focus of the NIR pulse that follows the pre-ionization. Changing the focusing conditions of the two pulses can also affect the volume of the ignition source. In combustion devices with poor fuel-air mixing having a larger plasma volume can be beneficial in improving the cycle-to-cycle performance and decreasing the coefficient of variance (COV) of the device.

Another parameter that has not been fully optimized yet is the minimum absorption energy. While the UV/NIR pulse combination has shown promising results and is a good candidate for practical implementation due to the widespread availability of Nd:YAG sources on the market, other combination of pulses could lead to further decrease in total energy required for ignition. One idea is to use a quantum resonant multi-photon ionization scheme (or REMPI) for the pre-ionization pulse. The resonant process will significantly increase the photoionization rate which will lower the laser energy required to ionized the gas. Several REMPI schemes for N<sub>2</sub> and O<sub>2</sub> ionization that can be attempted are available in literature<sup>144-146</sup>. Additionally, the energy addition pulse could be replaced with microwaves. As shown in Chapter 2, the electron avalanche ionization rate increases with wavelength. This means that it will be easier to breakdown the pre-ionized gas using microwaves than using an NIR pulse. Moreover, the UV generated plasma could

act as a waveguide and help focus the microwaves at the point of ignition<sup>46,147</sup>. Alternatively, if gas breakdown is to be avoided shorter wavelengths could be used for energy addition. A 266 nm/532 nm dual-pulse scheme would be an interesting approach from this point of view.

The REMPI contribution to the ability of the UV pulse to pre-ionize the gas should also be studied in more detail. The possibility for nitrogen REMPI at 266 nm was discussed in Chapter 3 with several authors citing this as a possible explanation for the lower absorption energies observed at 266 nm compared to 1064 nm. This can be investigated experimentally by conducting experiments in various gas mixtures. For example, if N<sub>2</sub> REMPI is indeed present at 266 nm one would expect to see a lower energy requirement for ionization in pure nitrogen mixtures than in pure oxygen. This would be an interesting finding because the ionization potential for oxygen is lower than that of nitrogen. In a non-resonant MPI process the opposite result would be expected. Optical emission experiments could also be used to demonstrate the presence of N<sub>2</sub> REMPI. The spectral measurements presented in this work in Chapter 3 only give a qualitative image of the plasma composition due to the limitations of the equipment used. Primarily, the long integration time of the spectrograph used for those measurements did not provide temporally resolved spectra at the early time (~20-100 ns after the pulse). Emission spectra obtained using a gated ICCD camera with short exposure mounted at the exit of the spectrograph will greatly improve the ability to observe small differences in the chemical composition of the UV and NIR laser plasma. By comparing emission spectra, one would expect to see strong emission from the second positive system of N<sub>2</sub> (C–B) and the first negative system of N<sub>2</sub><sup>+</sup> (B–X) around 350-450 nm if N<sub>2</sub> REMPI is involved in the ionization process for the 266 nm. Fitting of the molecular bands will also allow one to determine the plasma temperature at earlier times than was possible using Rayleigh scattering.

### 6.2.2 Other Applications for Dual-Pulse Pre-ionization

Laser generated plasma find several other applications besides source of ignition in engines. Past research has shown that ozone generated during optical breakdown can provide assistance in flame stabilization. This is mainly because ozone acts as a low temperature carrier oxygen atoms that are critical in chain branching reactions that take place in flames. For example, ozone decomposition and reaction with hydrogen atoms can increase the production of O and OH radicals in the pre-heat zone of the flame<sup>148</sup>. This kinetic enhancement leads to a hydrodynamic enhancement that can aid in stabilizing the flame under turbulent conditions. Therefore, a REMPI pre-ionization scheme targeting oxygen can enhance the production of ozone. Moreover an energy addition pulse can significantly increase the temperature of the discharge thus stimulating the production of ozone.

Laser plasma has also been used for flame holding in scramjet propulsion devices. Past research in this field has focused on the ability of the laser plasma to reduce the chemical reaction timescale by stimulating the local production of radicals. However, the dual-pulse technique presented here can enhance the flame holding ability by also controlling the fluid dynamics induced by the plasma. As shown in Chapter 6, the overlap of the dual-pulse can generate a stagnation plane which can increase the flow residence time inside the combustor. Combined with the increase in reaction rates associated with the formation of a plasma this will lead to a decrease of the reaction length inside the combustor.

Plasma assisted flow control for supersonic and hypersonic flight conditions has been demonstrated in the past<sup>68,149,150</sup>. Plasma injected into the boundary layer acts as a volumetric source of heat and momentum addition into the flow. Under certain conditions, changes in the flow structure caused by the injection of plasma can lead to a reduction of drag and decreased in shock

waves strength. The dual-pulse pre-ionization scheme developed in this work can provide a controlled source of energy addition into the flow. This can be achieved due to the ability of the dual-pulse technique to control the inverse bremsstrahlung absorption of the NIR laser pulse into the pre-ionized gas. In addition, the dual-pulse scheme can be used to control boundary layer separation. The vorticity induced by the laser plasma can add momentum into the flow near the airfoil surface and delay separation.

A dual-pulse scheme can be used for plasma-wave generation in high power laser plasma accelerators<sup>151</sup>. One of the key components in plasma accelerators is the generation of an ionized channel inside of which a high-power laser pulse is coupled. The interaction of the two laser pulses generates high amplitude longitudinal space-charge plasma waves that are capable of accelerating particles. Typically, femtosecond lasers have been used for the generation of plasma channels but, as demonstrated in Chapter 3, an UV pulse can also generate a weakly ionized channel plasma.

### **6.3 Final Thoughts**

This dissertation work comes at a moment in time when laser ignition is on the verge of becoming a reality in a number of industrial applications. I feel not only grateful but also privileged for the opportunity to conduct research in this exciting field. As I write this last words to conclude my doctoral work I leave with the hope that our community will find this contribution useful and that it will help inspire new doctoral students in their research activity.

## BIBLIOGRAPHY

1. Joshi, S., Olsen, D. B., Dumitrescu, C., Puzinauskas, P. V & Yalin, A. P. Laser-induced breakdown spectroscopy for in-cylinder equivalence ratio measurements in laser-ignited natural gas engines. *Appl. Spectrosc.* **63**, 549–54 (2009).
2. Yamaguchi, S. *et al.* Dual-Point Laser Ignition and its Location Effects on Combustion in Lean-Burn Gas Engine. *SAE Int. J. Engines* 2015-01–9041 (2015). doi:10.4271/2015-01-9041
3. Bihari, B., Gupta, S. B., Sekar, R., Gingrich, J. & Smith, J. Development of Advanced Laser Ignition System for Stationary Natural Gas Reciprocating Engines. in *ASME 2005 Internal Combustion Engine Division Fall Technical Conference (ICEF2005)* 601–608 (2005). doi:10.1115/ICEF2005-1325
4. McIntyre, D. L., Woodruff, S. D., McMillian, M. H., Richardson, S. W. & Gautam, M. Lean-Burn Stationary Natural Gas Reciprocating Engine Operation With a Prototype Miniature Diode Side Pumped Passively Q-Switched Laser Spark Plug. in *ASME 2009 Internal Combustion Engine Division Spring Technical Conference* 405–413 (2008). doi:10.1115/ICES2009-76013
5. Herdin, G. & Klausner, J. Laser Ignition: A New Concept to Use and Increase the Potentials of Gas Engines. in *ICEF-ASME 2005* 1–9 (2005). doi:10.1115/ICEF2005-1352
6. El-Rabii, H. *et al.* Laser spark ignition of two-phase monodisperse mixtures. *Opt. Commun.* **256**, 495–506 (2005).
7. Strozzi, C., Gillard, P. & Minard, J.-P. Laser-Induced Spark Ignition of Gaseous and Quiescent N-Decane–Air Mixtures. *Combust. Sci. Technol.* **186**, 1562–1581 (2014).

8. Lacaze, G., Cuenot, B., Poinso, T. & Oswald, M. Large eddy simulation of laser ignition and compressible reacting flow in a rocket-like configuration. *Combust. Flame* **156**, 1166–1180 (2009).
9. Manfletti, C. & Kroupa, G. Laser ignition of a cryogenic thruster using a miniaturised Nd:YAG laser. *Opt. Express* **21**, A1126-39 (2013).
10. Börner, M., Manfletti, C. & Oswald, M. Experimental Study of a Laser-Ignited Liquid Cryogenic Rocket Engine Conventional ignition methods of cryogenic rocket engines. in *Laser Ignition Conference* 1–19 (2015). doi:10.1364/LIC.2015.Th2A.5
11. Brieschenk, S., O’Byrne, S. & Kleine, H. Laser-induced plasma ignition studies in a model scramjet engine. *Combust. Flame* **160**, 145–148 (2013).
12. Brieschenk, S., Kleine, H. & O’Byrne, S. Laser ignition of hypersonic air–hydrogen flow. *Shock Waves* **23**, 439–452 (2013).
13. Negishi, J., Horisawa, H. & Kimura, I. Mixing and reaction enhancement characteristics of laser-induced plasmas and detonations in laser-augmented scramjets. *AIP Conf. Proc.* **830**, 151–162 (2006).
14. Gupta, S. B., Bihari, B., Sekar, R., Klett, G. M. & Ghaffarpour, M. Ignition Characteristics of Methane-air Mixtures at Elevated Temperatures and Pressures. in *ICES2005-1064* 1–7 (2005). doi:10.4271/2005-01-2189
15. Phuoc, T. & White, F. Laser-induced spark ignition of CH<sub>4</sub>/air mixtures. *Combust. Flame* **2180**, 203–216 (1999).
16. Barbosa, S., Scoufflaire, P., Ducruix, S. & Gaborel, G. Comparisons Between Spark Plug and Laser Ignition in a Gas Turbine Combustor. in *Proceedings of the European*

*Combustion Meeting 2–7* (2007).

17. Dumitrache, C., Rath, J., Yalin, A. P. & Gupta, S. Development of a Photonic Crystal Fiber Delivery System for Laser Ignition in Engines. in *45TH AIAA PLASMADYNAMICS AND LASERS CONFERENCE* 1–8 (AIAA, 2014).
18. Kopecek, H., Maier, H., Reider, G., Winter, F. & Wintner, E. Laser ignition of methane–air mixtures at high pressures. *Exp. Therm. Fluid Sci.* **27**, 499–503 (2003).
19. Herdin, G., Klausner, J., Weinrotter, M., Graf, J. & Wimmer, A. GE Jenbacher’s Update On Laser Ignited Engines. *ICEF-ASME 2006* 1–7 (2006). doi:10.1115/ICEF2006-1547
20. Ronney, P. D. Laser versus conventional ignition of flames. *Opt. Eng.* **33**, 510 (1994).
21. Phuoc, T. X. Laser-induced spark ignition fundamental and applications. *Opt. Lasers Eng.* **44**, 351–397 (2006).
22. Schwarz, E. *et al.* Laser-induced optical breakdown applied for laser spark ignition. *Laser Part. Beams* **28**, 109 (2010).
23. Dumitrache, C., Wilvert, N., Yalin, A. & Shneider, M. Laser Plasma Formation Using Dual Pulse Pre-Ionization. *44th AIAA Plasmadynamics Lasers Conf. Sand Diego, CA* (2013).
24. Wermer, L., Hansson, J. & Im, S. Dual-pulse laser-induced spark ignition and flame propagation of a methane diffusion jet flame. *Proc. Combust. Inst.* **36**, 4427–4434 (2017).
25. Phuoc, T. X. & White, F. P. An optical and spectroscopic study of laser-induced sparks to determine available ignition energy. *Proc. Combust. Inst.* **29**, 1621–1628 (2002).
26. Bradley, D., Sheppard, C. G. W., Suardjaja, I. M. & Woolley, R. Fundamentals of high-energy spark ignition with lasers. *Combust. Flame* **138**, 55–77 (2004).

27. Maker, P. D., Terhune, R. W. & Savage, C. W. Optical Third Harmonic Generation. in *3rd International Congress on Quantum Electronics* 1559–1576 (1964).
28. B., Z. Y. & Raizer, P. Cascade Ionization Of a Gas By a Light Pulse. *Sov. Phys. JETP* **20**, 772–780 (1965).
29. Raizer, Y. *Laser-Induced Discharge Phenomena*. (Consultants Bureau, 1977).
30. Demichelis, C. Laser Induced Gas Breakdown: A Bibliographical Review. *IEEE J. Quantum Electron.* **5**, 188–202 (1969).
31. Morgan, C. G. Laser-induced breakdown of gases. *Reports Prog. Phys.* **38**, 621–665 (1975).
32. Radziemski, L. J. & Cremers, D. *Lasers-Induced Plasmas and Applications*. (Marcel Dekker, INC., 1989).
33. Dale, J. D., Smy, P. R., Way-Nee, D. & Clements, R. M. Laser-ignited internal combustion engine. *Combust. Flame* **30**, 319–320 (1977).
34. Krasnyuk, I. K. & Pashinin, P. P. Breakdown in Argon and Nitrogen Under the Influence of a 0.35- $\mu$  Picosecond Laser Pulse. *Journal of Experimental and Theoretical Physics Letters* **15**, 471–473 (1972).
35. Phuoc, T. X. Laser spark ignition: Experimental determination of laser-induced breakdown thresholds of combustion gases. *Opt. Commun.* **175**, 419–423 (2000).
36. Buscher, H. T., Tomlinson, R. G. & Damon, E. K. Frequency dependence of optically induced gas breakdown. *Phys. Rev. Lett.* **15**, 847–849 (1965).
37. Raizer, Y. *Gas Discharge Physics*. (Springer: New York, 1991).
38. Davis, J. P., Smith, a L., Giranda, C. & Squicciarini, M. Laser-induced plasma formation

- in Xe, Ar, N<sub>2</sub>, and O<sub>2</sub> at the first four Nd:YAG harmonics. *Appl. Opt.* **30**, 4358–64 (1991).
39. Tambay, R. & Thareja, R. K. Laser-induced breakdown studies of laboratory air at 0.266, 0.355, 0.532, and 1.06  $\mu\text{m}$ . *J. Appl. Phys.* **70**, 2890–2892 (1991).
  40. Sircar, A., Dwivedi, R. K. & Thareja, R. K. Laser induced breakdown of Ar, N<sub>2</sub> and O<sub>2</sub> gases using 1.064, 0.532, 0.355 and 0.266  $\mu\text{m}$  radiation. *Appl. Phys. B Laser Opt.* **627**, 623–627 (1996).
  41. Zvorykin, V. Control of extended high-voltage electric discharges in atmospheric air by UV KrF-laser radiation. *Quantum Electron.* **41**, 227–233 (2011).
  42. Way, J., Hummelt, J. & Scharer, J. Experimental measurements of multiphoton enhanced air breakdown by a subthreshold intensity excimer laser. *J. Appl. Phys.* **106**, 83303 (2009).
  43. Shneider, M. N., Zheltikov, a. M. & Miles, R. B. Tailoring the air plasma with a double laser pulse. *Phys. Plasmas* **18**, 63509 (2011).
  44. Zhou, B. *et al.* Revival of femtosecond laser plasma filaments in air by a nanosecond laser. *Opt. Express* **17**, 11450–11456 (2009).
  45. Starikovskiy, A. Y., Semenov, I. E. & Shneider, M. N. Supression of laser breakdown by pulsed nonequilibrium ns discharge. *Plasma Sources Sci. Technol.* **25**, 54008 (2016).
  46. Michael, J. B., Dogariu, a., Shneider, M. N. & Miles, R. B. Subcritical microwave coupling to femtosecond and picosecond laser ionization for localized, multipoint ignition of methane/air mixtures. *J. Appl. Phys.* **108**, 93308 (2010).
  47. Sattmann, R. *et al.* Laser-induced breakdown spectroscopy of steel samples using multiple Q-switch Nd:YAG laser pulses. *J. Phys. D. Appl. Phys.* **28**, 2181–2187 (1995).

48. Joshi, S., Yalin, A. P. & Galvanauskas, A. Use of hollow core fibers, fiber lasers, and photonic crystal fibers for spark delivery and laser ignition in gases. *Appl. Opt.* **46**, 4057–64 (2007).
49. Dumitrache, C., Rath, J. & Yalin, A. High Power Spark Delivery System Using Hollow Core Kagome Lattice Fibers. *Materials (Basel)*. **7**, 5700–5710 (2014).
50. Stakhiv, A., Kopecek, R., Zheltikov, A. & Wintner, E. Laser ignition of engines via optical fibers? *Laser Phys.* **14**, 738–747 (2004).
51. Mullett, J. D. *et al.* A comparative study of optical fibre types for application in a laser-induced ignition system. *J. Opt. A Pure Appl. Opt.* **11**, 54007 (2009).
52. Yalin, A. High power fiber delivery for laser ignition applications. *Opt. Express* **21**, 515–517 (2013).
53. Leeuwen, R. Van *et al.* VCSEL-pumped passively Q-switched monolithic solid-state lasers. in *Proc. SPIE 9726, Solid State Lasers XXV: Technology and Devices* 1–6 (2016). doi:10.1117/12.2213322
54. Taira, T. Microchip Laser , Ceramic Laser toward Giant Micro-photonics. in *17th Opto-Electronics and Communications Conference (OECC 2012)* **3**, 578–579 (2012).
55. Tsunekane, M. & Taira, T. High Peak Power, Passively Q-switched Yb: YAG/Cr: YAG Micro-Lasers. *IEEE J. Quantum Electron.* **49**, 454–461 (2013).
56. Weinrotter, M. *et al.* Laser ignition of ultra-lean methane/hydrogen/air mixtures at high temperature and pressure. *Exp. Therm. Fluid Sci.* **29**, 569–577 (2005).
57. Lee, T. W., Jain, V. & Kozola, S. Measurements of minimum ignition energy by using laser

- sparks for hydrocarbon fuels in air: Propane, dodecane, and jet-A fuel. *Combust. Flame* **125**, 1320–1328 (2001).
58. Lewis, B. & Von Elbe, G. *Combustion, Flames and Explosions of Gases*. (Academic Press, New York, 1987).
  59. Beduneau, J., Bonggyu, K., Zimmer, L. & Ikeda, Y. Measurements of minimum ignition energy in premixed laminar methane/air flow by using laser induced spark. *Combust. Flame* **132**, 653–665 (2003).
  60. E.H. Lim, A. McIlroy, P.D. Ronney, J. A. S. *Detailed Characterization of Minimum Ignition Energies of Combustible Gases Using Laser Ignition Sources. Transport phenomena in combustion* **1**, (1996).
  61. Dumitrache, C. *et al.* Laser Ignition of Methane-Air Mixtures with a Rapid Compression Machine. in *53rd AIAA Aerospace Sciences Meeting* 1–12 (2015).
  62. Dumitrache, C. *et al.* A study of laser induced ignition of methane – air mixtures inside a Rapid Compression Machine. *Proc. Combust. Inst.* **36**, 3431–3439 (2017).
  63. Morsy, M. H. & Chung, S. H. Numerical simulation of front lobe formation in laser-induced spark ignition of  $\text{CH}_4$ /air mixtures. *Proc. Combust. Inst.* **29**, 1613–1619 (2002).
  64. Endo, T. *et al.* An experimental study on the ignition ability of a laser-induced gaseous breakdown. *Combust. Flame* **178**, 1–6 (2017).
  65. Ghosh, S. & Mahesh, K. Numerical simulation of laser – induced breakdown in air. in *46th AIAA Aerospace Sciences Meeting* 1–22 (2008). doi:10.2514/6.2008-1069
  66. Castela, M. *et al.* A 3-D DNS and experimental study of the effect of the recirculating flow pattern inside a reactive kernel produced by nanosecond plasma discharges in a methane-

- air mixture. *Proc. Combust. Inst.* **36**, 4095–4103 (2017).
67. Kono, M., Niu, K., Tsukamoto, T. & Ujiie, Y. Mechanism of flame kernel formation produced by short duration sparks. *Symp. Combust.* **22**, 1643–1649 (1988).
  68. Unfer, T. & Boeuf, J. P. Modelling of a nanosecond surface discharge actuator. *J. Phys. D. Appl. Phys.* **42**, 194017 (2009).
  69. Pancheshnyi, S. V., Lacoste, D. A., Bourdon, A. & Laux, C. O. Ignition of propane-air mixtures by a repetitively pulsed nanosecond discharge. *IEEE Trans. Plasma Sci.* **34**, 2478–2487 (2006).
  70. Bekefi, G. *Principles of Laser Plasmas*. (John Wiley, 1976).
  71. Ostrovskaya, G. V & Zaidel', A. N. Laser spark in gases. *Sov. Phys. Uspekhi* **16**, 834–855 (1974).
  72. RAMSDEN, S. A. & SAVIC, P. A Radiative Detonation Model for the Development of a Laser-Induced Spark in Air. *Nature* **203**, 1217–1219 (1964).
  73. Ramsden, S. A. & Davies, W. E. R. Radiation Scattered From the Plasma Produced by a Focused Ruby Laser Beam. *Phys. Rev. Lett.* **13**, 227–230 (1964).
  74. Adलगren, R. & Elliott, G. S. Energy Deposition in Supersonic Flows. in *AIAA Proceedings* (2001).
  75. Kartashov, D. *et al.* Free-space nitrogen gas laser driven by a femtosecond filament. *Phys. Rev. A* **86**, 33831 (2012).
  76. Tzortzakіs, S. *et al.* Femtosecond laser-guided electric discharge in air. *Phys. Rev. E. Stat. Nonlin. Soft Matter Phys.* **64**, 57401 (2001).

77. Couairon, A. & Mysyrowicz, A. Femtosecond filamentation in transparent media. *Phys. Rep.* **441**, 47–189 (2007).
78. Gordon, D. F. *et al.* Streamerless guided electric discharges triggered by femtosecond laser filaments. *Phys. Plasmas* **10**, 4530–4538 (2003).
79. Wu, C. *et al.* Laser-induced dissociation and explosion of methane and methanol. *J. Phys. B At. Mol. Opt. Phys.* **35**, 2575–2582 (2002).
80. Keefer, D. R., Henriksen, B. B. & Braerman, W. F. Experimental study of a stationary laser-sustained air plasma. *J. Appl. Phys.* **46**, 1080–1083 (1975).
81. Morgan, C. G. Laser-induced breakdown of gases. *Reports Prog. Phys.* **38**, 621–665 (2001).
82. Guthrie, J. A., Wang, X. X. & Radziemski, L. J. Resonance-enhanced multiphoton ionization of N<sub>2</sub> at 193 and 248 nm detected by N<sub>2</sub><sup>+</sup> fluorescence. *Chem. Phys. Lett.* **170**, 117–120 (1990).
83. Hankin, S. M., Villeneuve, D. M., Corkum, P. B. & Rayner, D. M. Nonlinear Ionization of Organic Molecules in High Intensity Laser Fields. *Phys. Rev. Lett.* **84**, 5082–5085 (2000).
84. Mishima, K., Nagaya, K., Hayashi, M. & Lin, S. H. Effect of quantum interference on tunneling photoionization rates of N<sub>2</sub> and O<sub>2</sub> molecules. *J. Chem. Phys.* **122**, (2005).
85. Keldysh, L. V. Ionization in the field of a strong electromagnetic wave. *J. Exp. Theor. Phys.* **20**, 1307–1314 (1965).
86. Dumitrache, C., Limbach, C. M. & Yalin, A. P. Threshold characteristics of ultraviolet and near infrared nanosecond laser induced plasmas. *Phys. Plasmas* **23**, 93515 (2016).
87. Tozer, E. Theory of the Ionization of Gases. *Phys. Rev.* **137**, A1665 (1965).

88. Geltman, S. Free-free radiation in electron-neutral atom collisions. *J. Quant. Spectrosc. Radiat. Transf.* **13**, 601–613 (1973).
89. Dalgarno, A. & Lane, N. Free-free transitions of electrons in gases. *Astrophys. J.* **145**, 623–633 (1966).
90. Taylor, R. L. & Caledonia, G. Experimental determination of the cross-sections for neutral bremsstrahlung I. Ne, Ar and Xe. *J. Quant. Spectrosc. Radiat. Transf.* **9**, 657–679 (1969).
91. Karzas, Q. J. & Latter, R. ELECTRON RADIATIVE TRANSITIONS IN A COULOMB FIELD. *Astrophys. J.* **167**, 167–212 (1961).
92. Yalin, A. P., Wilvert, N., Dumitrache, C., Joshi, S. & Shneider, M. N. Laser plasma formation assisted by ultraviolet pre-ionization. *Phys. Plasmas* **21**, 103511 (2014).
93. Kohmoto, M. & Watanabe, T. Penning ionization of optically allowed excited atoms: the He(2 1 P) and Ar system. *J. Phys. B At. Mol. Phys.* **10**, 1875–1887 (1977).
94. Kossyi, I. a, Kostinsky, a Y., Matveyev, a a & Silakov, V. P. Kinetic scheme of the non-equilibrium discharge in nitrogen-oxygen mixtures. *Plasma Sources Sci. Technol.* **1**, 207–220 (1992).
95. Dibble, R. W. & Hollenbach, R. E. Laser rayleigh thermometry in turbulent flames. *Symp. Combust.* **18**, 1489–1499 (1981).
96. Miles, R. B., Lempert, W. R. & Forkey, J. N. Laser Rayleigh scattering. *Meas. Sci. Technol.* **12**, R33–R51 (2001).
97. Limbach, C. M., Dumitrache, C. & Yalin, A. P. Laser Light Scattering from Equilibrium , High Temperature. in *47th AIAA Plasmadynamics and Lasers* 1–13 (2016).

98. Froula, D., Sheffield, J., Glenzer, S. & Luhmann, N. *Plasma Scattering of Electromagnetic Radiation: Theory and Measurements*. (Elsevier Ltd, 2011).
99. Alcock, A. J. & Ramsden, S. A. Two wavelength interferometry of a laser-induced spark in air. *Appl. Phys. Lett.* **8**, 187–188 (1966).
100. Miles, R. B. *et al.* New diagnostic methods for laser plasma- and microwave-enhanced combustion. *Philos. Trans. R. Soc. A Math. Phys. Eng. Sci.* **373**, 20140338 (2015).
101. Settles, G. S. *Schlieren and Shadowgraph Techniques: Visualizing Phenomena in Transparent Media*. (Springer-Verlag, 2001).
102. Wilvert, N., Joshi, S. & Yalin, A. Ultraviolet Laser Plasma Preionization and Novel Thomson. 1–15
103. Akhmanov, S., Kovrigin, A., Strukov, M. & Khokhlov, R. Frequency Dependence of the Threshold of Optical Breakdown in Air. *JETP Lett.* **1**, 25–29 (1965).
104. Chylek, P., Jarzembski, M. a, Srivastava, V. & Pinnick, R. G. Pressure dependence of the laser-induced breakdown thresholds of gases and droplets. *Appl. Opt.* **29**, 2303–6 (1990).
105. Lewis, W. B. & Wadt, W. R. Laser-induced fluorescence in N<sub>2</sub> and N<sub>2</sub><sup>+</sup> by multiple-photon excitation at 266 nm. *Chem. Phys. Lett.* **78**, 266–269 (1981).
106. Choi, Y., Zhou, C., Stolz, P., Joshi, S. & Yalin, A. Simulation and Measurement of the Laser Induced Breakdown in Air and Argon for Nanosecond Order Pulses. in *PROCEEDINGS OF THE ASME INTERNAL COMBUSTION ENGINE DIVISION FALL TECHNICAL CONFERENCE* 1–9 (ASME, 2012).
107. Parigger, C., Plemmons, D. H., Hornkohl, J. O. & Lewis, J. W. L. Temperature measurements from first-negative N<sub>2</sub><sup>+</sup> spectra produced by laser-induced multiphoton

- ionization and optical breakdown of nitrogen. *Appl. Opt.* **34**, 3331–3335 (1995).
108. Bebb, H. B. & Gold, A. Multiphoton ionization of hydrogen and rare-gas atoms. *Phys. Rev.* **143**, 1–24 (1966).
  109. Lecompte, C., Mainfray, G., Manus, C. & Sanchez, F. Experimental demonstration of laser temporal coherence effects on multiphoton ionization processes. *Phys. Rev. Lett.* **32**, 265–268 (1974).
  110. Lambropoulos, P. Effect of light polarization on multiphoton ionization of atoms. *Phys. Rev. Lett.* **28**, 585–587 (1972).
  111. Kramida, A., Ralchenko, Yu., Reader, J. NIST Atomic Spectra Database. *National Institute of Standards and Technology* Available at: <http://physics.nist.gov/asd>.
  112. El-Rabii, H., Victorov, S. B. & Yalin, A. P. Properties of an air plasma generated by ultraviolet nanosecond laser pulses. *J. Phys. D. Appl. Phys.* **42**, 75203 (2009).
  113. Glumac, N., Elliott, G. & Boguszko, M. Temporal and Spatial Evolution of the Thermal Structure of a Laser Spark in Air. in *43rd AIAA Aerospace Sciences Meeting and Exhibit* 1–16 (2005). doi:10.2514/6.2005-204
  114. Joshi, S., El-Rabii, H., Dumitrescu, C., Puzinauskas, P. & Yalin, a. P. Temperature and Electron Density Measurements of Laser-Induced Plasmas in Air at Elevated Pressures. *Spectrosc. Lett.* **44**, 103–112 (2011).
  115. Yalin, A. P. *et al.* Laser plasma formation assisted by ultraviolet pre-ionization. *Plasmas* **21**, 103511–6 (2014).
  116. Shneider, M. N. & Miles, R. B. Laser induced avalanche ionization in gases or gas mixtures with resonantly enhanced multiphoton ionization or femtosecond laser pulse pre-ionization.

- Phys. Plasmas* **19**, 83508 (2012).
117. Siegman, A. Defining, measuring, and optimizing laser beam quality. *Proc. SPIE* **V**, 2–12 (1993).
  118. Bozkurt, M., Fikri, M. & Schulz, C. Investigation of the kinetics of OH\* and CH\* chemiluminescence in hydrocarbon oxidation behind reflected shock waves. *Appl. Phys. B Lasers Opt.* **107**, 515–527 (2012).
  119. Heywood, J. *Internal Combustion Engines Fundamentals*. (McGraw Hill, 1988).
  120. Tinaut, F. V., Reyes, M., Giménez, B. & Pastor, J. V. Measurements of OH\* and CH\* chemiluminescence in premixed flames in a constant volume combustion bomb under autoignition conditions. *Energy and Fuels* **25**, 119–129 (2011).
  121. Prince, J. C. & Williams, F. A. Short chemical-kinetic mechanisms for low-temperature ignition of propane and ethane. *Combust. Flame* **159**, 2336–2344 (2012).
  122. Dumitrache, C., Limbach, C. M. & Yalin, A. P. Laser Thermal Ignition Using a Dual-Pulse Approach. *54 AIAA Aerosp. Sci. Meet.* 1–9 (2016). doi:10.2514/6.2016-0460
  123. Kojima, H., Takahashi, E. & Furutani, H. Breakdown plasma and vortex flow control for laser ignition using a combination of nano- and femto-second lasers. *Opt. Express* **22**, A90 (2014).
  124. Metghalchi, M. & Keck, J. C. Burning Velocities of Mixtures of Air with Methanol , Isooctane , and Indolene at High Pressure and Temperature. *Combust. Flame* **48**, 191–210 (1982).
  125. Boguszko, M. & Elliott, G. S. On the use of filtered Rayleigh scattering for measurements in compressible flows and thermal fields. *Exp. Fluids* **38**, 33–49 (2004).

126. Toro, E. *Riemann solvers and numerical methods for fluid dynamics*. (Springer-Verlag, 1999).
127. Fedkiw, R. P., Merriman, B. & Osher, S. High Accuracy Numerical Methods for Thermally Perfect Gas Flows with Chemistry. *J. Comput. Phys.* **132**, 175–190 (1997).
128. Bird, R. B., Stewart, W. E. & Lightfoot, E. N. *Transport Phenomena*. (Wiley, 2001).
129. Wilke, R. C. A Viscosity Equation for Gas Mixtures. *J. Phys. Chem.* **18**, 518 (1950).
130. Anderson, J. D. *Computational Fluid Dynamics: The Basics With Applications*. (McGraw Hill, 1995).
131. Hoffman, J. D. *Numerical Method for Engineers and Scientist*. (Marcel Dekker, INC., 2001).
132. Roe, P. L. & Pike, J. Efficient construction and utilisation of approximate Riemann solutions. *Comput. methods Appl. Sci. Eng.* VI 499–518 (1984).
133. Edwards, J. R. A low-diffusion flux-splitting scheme for Navier-Stokes calculations. *Comput. Fluids* **26**, 635–659 (1997).
134. LeVeque, R. J. *Numerical Methods for Conservation Laws. Mathematics of Computation* **57**, (1992).
135. Godunov, S. K. Finite Difference Method for Numerical Computation of Discontinuous Solutions of the Equations of Fluid Dynamics. *Mat. Sb.* **47**, 271 (1959).
136. Roe, P. Approximate Riemann solvers, parameter vectors, and difference schemes. *J. Comput. Phys.* **372**, 357–372 (1981).
137. Lomax, H., Pulliam, T. H. & Zingg, D. W. *Fundamentals of computational fluid dynamics*. (Springer-Verlag, 2003).

138. Sod, G. ~A. A survey of several finite difference methods for systems of nonlinear hyperbolic conservation laws. *Journal of Computational Physics* **27**, 1–31 (1978).
139. Batchelor, G. K. *An Introduction to Fluid Dynamics*. Cambridge University Press (1967).  
doi:10.1063/1.3060769
140. Dors, I. G. & Parigger, C. G. Computational fluid-dynamic model of laser-induced breakdown in air. *Appl. Opt.* **42**, 5978–85 (2003).
141. Taylor, G. The Formation of a Blast Wave by a Very Intense Explosion. I. Theoretical Discussion. *Proc. R. Soc. A Math. Phys. Eng. Sci.* **201**, 175–186 (1950).
142. Taylor, G. The Formation of a Blast Wave by a Very Intense Explosion. II. The Atomic Explosion of 1945. *Proc. R. Soc. A Math. Phys. Eng. Sci.* **201**, 175–186 (1950).
143. Kundu, P. K. & Cohen, I. M. *Fluid Mechanics*. Book (Academic Press, 2008).
144. McGuire, S., Chng, T. & Miles, R. Nanosecond time-resolved 2+ 2 Radar REMPI measurements performed in molecular nitrogen. *AIAA 44th Lasers Plasmadynamics Proc.* 2–7 (2013).
145. Salumbides, E. J., Khramov, a & Ubachs, W. High-resolution 2 + 1 REMPI study of the a''1Sigma(g)+ state in N2. *J. Phys. Chem. A* **113**, 2383–6 (2009).
146. Mori, H., Ishida, T., Aoki, Y. & Niimi, T. A Study on REMPI as a Measurement Technique for Highly Rarefied Gas Flows. Analyses of Experimental REMPI Spectra in Supersonic Free Molecular Flows. *JSME Int. J. Ser. B* (2001).
147. Shneider, M. N., Zheltikov, a. M. & Miles, R. B. Long-lived laser-induced microwave plasma guides in the atmosphere: Self-consistent plasma-dynamic analysis and numerical simulations. *J. Appl. Phys.* **108**, 33113 (2010).

148. Ombrello, T., Won, S. H., Ju, Y. & Williams, S. Flame propagation enhancement by plasma excitation of oxygen. Part I: Effects of O<sub>3</sub>. *Combust. Flame* **157**, 1906–1915 (2010).
149. Corke, T. C., Enloe, C. L. & Wilkinson, S. P. Dielectric Barrier Discharge Plasma Actuators for Flow Control. *Annu. Rev. Fluid Mech.* **42**, 505–529 (2010).
150. Little, J., Nishihara, M. & Adamovich, I. High-lift airfoil trailing edge separation control using a single dielectric barrier discharge plasma actuator. *Exp. Fluids* **48**, 521–537 (2010).
151. Sodha, M. S. *et al.* Generation of plasma waves by Gaussian laser beam and stimulated Raman scattering. *Plasma Phys.* **18**, 879–888 (1976).

## Appendix A:

### Solution Procedure for Thermally Perfect Gas

As discussed in section 5.1.2, the main difference between a caloric perfect gas and a thermally perfect gas is given by the implicit dependence of the internal energy on temperature. In general, for a thermally perfect gas the internal energy is given by:

$$E = \rho \left( e + \frac{u^2 + v^2}{2} \right) \quad (\text{A.1})$$

In other words the total energy can be split in two contributions: the total internal energy and the kinetic energy. Furthermore, Eq. (A.1) can be written in terms of the fluid enthalpy since:

$$e = h - \frac{p}{\rho} \quad (\text{A.2})$$

The state of the thermodynamic system is described by the caloric equation of state (obtained after substituting Eq. (A.2) into (A.1)) together with the ideal gas law as follows:

$$\begin{cases} E = -p + \rho \frac{(u^2+v^2)}{2} + \rho h(T) \\ p = \rho R_g T \end{cases} \quad (\text{A.3})$$

The Navier-Stokes system written in the form given by Eqs. (5.1)-(5.5) gives relations for pressure,  $p$ , velocity,  $u$ ,  $v$ , and energy,  $E$ . In order to close the problem a relationship for the gas temperature is still needed. This is obtained from (A.3) by plugging the equations of state into the caloric state equation and solve for temperature:

$$T = \frac{-E + \rho \frac{u^2 + v^2}{2} + \rho h(T)}{\rho R_g} \quad (\text{A.4})$$

It is important to note that Eq. (A.4) is implicit in temperature and needs to be solved numerically together with Eqs. (5.1)-(5.5) before advancing the solution to the next step. An equivalent statement to Eq. (A.4) is:

$$T = C_1 + C_2 h(T) \quad (\text{A.5})$$

where:

$$\begin{cases} C_1 = -E + \rho \frac{u^2 + v^2}{2} / (\rho R_g) \\ C_2 = 1/R_g \end{cases} \quad (\text{A.6})$$

Equation (A.5) is solved numerically using a Newton-Raphson iterative technique. The method involved finding successively better approximations to the roots of the nonlinear equation based on information from previous iteration (or “guess”) and the derivative (evolution) of the function:

$$T_{n+1} = T_n - \frac{f(T_n)}{f'(T_n)} \quad (\text{A.7})$$

The function is given by:

$$f(T) = T - C_1 - C_2 h(T) \quad (\text{A.8})$$

A schematic describing the Newton method is shown Figure A.1 below.

The slope of the function is computed using a centered finite difference scheme such that Eq. (A.7) becomes:

$$T_{n+1} = T_n - \frac{f(T_n) \Delta T^2}{f(T_n + \Delta T) - 2f(T_n) + f(T_n - \Delta T)} \quad (\text{A.9})$$

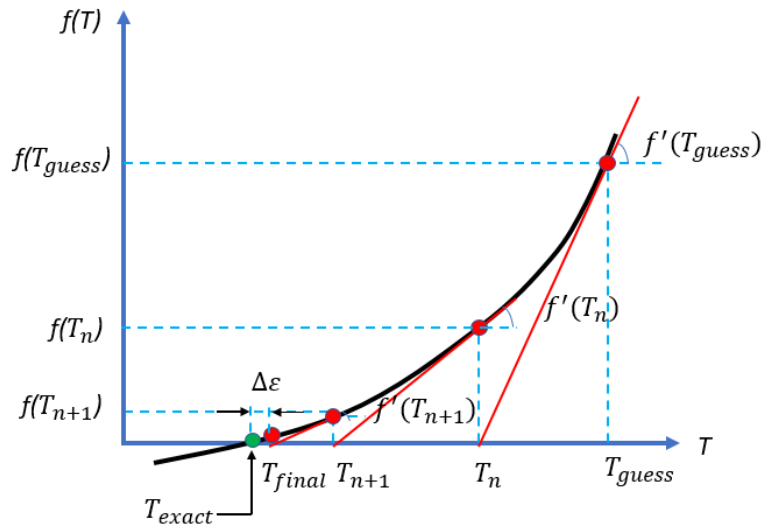


Figure A.1: Diagram depicting the solution finding algorithm for temperature using Newton-Raphson method

## Appendix B:

### Roe-Pikes Algorithm for the Advection Problem

#### B.1 Euler Equations

The advection problem is governed by the compressible Euler equations. The equations are obtained from the general conservation laws simply by making the diffusion terms and the geometrical source term equal to zero.

$$U_t + F(U)_r + G(U)_z = 0 \quad (\text{B.1})$$

Where the vector of conservative variables,  $U$ , and the advection fluxes,  $F(U)$  and  $G(U)$ , are described by Eqs. (5.2)-(5.3) just like in section 5.1.1.

For the Roe-Pikes method the conservation equations are re-written in terms of the Jacobian matrices of the advection flux as follows:

$$U_t + A(U)U_r + B(U)U_z = 0 \quad (\text{B.2})$$

The Jacobian is obtained by taking the derivatives of the flux with respect to the conservative variables. In the r-direction this is:

$$A(U) = \frac{\partial F(U)}{\partial U} = \begin{bmatrix} 0 & 1 & 0 & 0 \\ -u^2 + 0.5(\gamma - 1)V^2 & (3 - \gamma)u & -(\gamma - 1)v & \gamma - 1 \\ -uv & v & u & 0 \\ u \left[ 0.5(\gamma - 1)V^2 - H \right] & H - (\gamma - 1)u^2 & -(\gamma - 1)uv & \gamma u \end{bmatrix} \quad (\text{B.3})$$

Similarly, for the z-direction:

$$B(U) = \frac{\partial G(U)}{\partial U} = \begin{bmatrix} 0 & 1 & 0 & 0 \\ -v^2 + 0.5(\gamma-1)\bar{V}^{-2} & (3-\gamma)v & -(\gamma-1)u & \gamma-1 \\ -uv & u & v & 0 \\ v \left[ 0.5(\gamma-1)\bar{V}^{-2} - H \right] & H - (\gamma-1)v^2 & -(\gamma-1)uv & \gamma \end{bmatrix} \quad (\text{B.4})$$

With the corresponding eigenvalues:

$$\begin{cases} \lambda^r_1 = u - a; \lambda^r_2 = \lambda^r_3 = u; \lambda^r_4 = u + a; \rightarrow r\text{-split} \\ \lambda^z_1 = v - a; \lambda^z_2 = \lambda^z_3 = v; \lambda^z_4 = v + a; \rightarrow z\text{-split} \end{cases} \quad (\text{B.5})$$

The eigenvectors can also be obtained from the Jacobian matrices  $A(U)$  and  $B(U)$  are:

$$k_r^{(1)} = \begin{bmatrix} 1 \\ u - a \\ v \\ H - au \end{bmatrix}; k_r^{(2)} = \begin{bmatrix} 1 \\ u \\ v \\ \frac{1}{2}\bar{V}^2 \end{bmatrix}; k_r^{(3)} = \begin{bmatrix} 0 \\ 0 \\ 1 \\ v \end{bmatrix}; k_r^{(4)} = \begin{bmatrix} 1 \\ u + a \\ v \\ H + au \end{bmatrix} \quad (\text{B.6})$$

$$k_z^{(1)} = \begin{bmatrix} 1 \\ v - a \\ u \\ H - av \end{bmatrix}; k_z^{(2)} = \begin{bmatrix} 1 \\ v \\ u \\ \frac{1}{2}\bar{V}^2 \end{bmatrix}; k_z^{(3)} = \begin{bmatrix} 0 \\ 0 \\ 1 \\ u \end{bmatrix}; k_z^{(4)} = \begin{bmatrix} 1 \\ v + a \\ u \\ H + av \end{bmatrix} \quad (\text{B.7})$$

To find the wave strengths one needs to solve the linearized Riemann problem around a reference state,  $\hat{U}$ , as described in section 5.2.3 for both the r-split and the z-split problems. The result of the linearized problem is given in terms of the data jump across the discontinuity:

$$\begin{cases} \Delta U_r = \sum_{i=1}^4 \hat{\alpha}_r k_r^{(i)} \\ \Delta U_z = \sum_{i=1}^4 \hat{\alpha}_z k_z^{(i)} \end{cases} \quad (\text{B.8})$$

The expressions for the wave strengths will be provided by solving the two 4x4 linear systems of equations. Accordingly, the wave strengths for the r-split problem are given by:

$$\begin{cases} \hat{\alpha}_1^r = \frac{1}{2a} [\Delta p - \hat{\rho} \hat{a} \Delta u] \\ \hat{\alpha}_2^r = \Delta \rho - \Delta p / \hat{a}^2 \\ \hat{\alpha}_3^r = \rho \Delta v \\ \hat{\alpha}_4^r = \frac{1}{2a} [\Delta p + \hat{\rho} \hat{a} \Delta u] \end{cases} \quad (\text{B.9})$$

The z-split problem:

$$\begin{cases} \hat{\alpha}_1^z = \frac{1}{2a} [\Delta p - \hat{\rho} \hat{a} \Delta v] \\ \hat{\alpha}_2^z = \Delta \rho - \Delta p / \hat{a}^2 \\ \hat{\alpha}_3^z = \rho \Delta u \\ \hat{\alpha}_4^z = \frac{1}{2a} [\Delta p + \hat{\rho} \hat{a} \Delta v] \end{cases} \quad (\text{B.10})$$

Finally, the sought average vector is found by solving the set equations given by:

$$\begin{cases} \Delta U = \sum_{i=1}^4 \tilde{\alpha}_r k_r^{(i)} \\ \Delta F = \sum_{i=1}^4 \tilde{\alpha}_r \tilde{\lambda}_r k_r^{(i)} \end{cases} \quad (\text{B.11})$$

Where the wave strengths, Eqs. (B.9)-(B.10), the eigenvectors, Eqs. (B.6)-(B.7) and the eigenvalues, Eq. (B.5) are all evaluated at the unknown average state:

$$\tilde{W} = \begin{bmatrix} \tilde{\rho} \\ \tilde{u} \\ \tilde{v} \\ \tilde{a} \end{bmatrix} \quad (\text{B.12})$$

The average primitive variables found by solving Eq. (B.11) are the same irrespective of the dimensional split and are given by:

$$\left\{ \begin{array}{l} \tilde{\rho} = \sqrt{\rho_L \rho_R} \\ \tilde{u} = \frac{\sqrt{\rho_L} u_L + \sqrt{\rho_R} u_R}{\sqrt{\rho_L} + \sqrt{\rho_R}} \\ \tilde{v} = \frac{\sqrt{\rho_L} v_L + \sqrt{\rho_R} v_R}{\sqrt{\rho_L} + \sqrt{\rho_R}} \\ \tilde{H} = \frac{\sqrt{\rho_L} H_L + \sqrt{\rho_R} H_R}{\sqrt{\rho_L} + \sqrt{\rho_R}} \end{array} \right. \quad (\text{B.13})$$

It is important to note that in order to find the vector of the average primitive variables one needs the speed of sound,  $\tilde{a}$ , not the enthalpy,  $\tilde{H}$ , as given by in Eq. (B.13) above. One possibility is to determine the average temperature,  $\tilde{T}$ , by table lookup once the average enthalpy is computed from Eq. (B.13). Then the speed of sound at the average state is simply given by:

$$\tilde{a} = \sqrt{\tilde{\rho} \tilde{R}_g \tilde{T}} \quad (\text{B.14})$$

## B.2 Algorithm

To find the intercell flux for one of the dimensional split problem using the Roe-Pikes method, the following procedure should be followed:

- Find the primitive variable at the average state using Eqs. (B.13)-(B.14).
- Solve for the eigenvalues at the average state using Eq. (B.5) so that  $\tilde{\lambda}_i = \lambda_i(\tilde{W})$
- Compute the eigenvectors from Eq. (B.6) also at the average state:  $\tilde{k}^{(i)} = \tilde{k}^{(i)}(\tilde{W})$
- Similarly, compute the wave strengths using Eq. (B.9) at the average state:  $\tilde{\alpha}_i = \alpha_i(\tilde{W})$
- Find the intercell flux using the following equation:

$$F_{i+\frac{1}{2}} = F_L + \sum_{i=1}^n \tilde{\alpha}_i \tilde{\lambda}_i \tilde{k}^{(i)} \quad (\text{B.15})$$

- Repeat the same procedure for the other dimensional split.